

Effect of Reactive Ion Etching on Laser-Annealed Low- κ SiCOH Materials

Kris Beykirch

Physics, Corning Community College

NNIN REU Site: Cornell NanoScale Science and Technology Facility, Cornell University, Ithaca, NY

NNIN REU Principal Investigator: Dr. Michael Thompson, Associate Professor, Materials Science and Engineering, Cornell University

NNIN REU Mentor: Robert Bell, Materials Science and Engineering, Cornell University

Contact: kmb364@cornell.edu, mot1@cornell.edu, rtb83@cornell.edu

Introduction:

The speed of current microelectronic devices is limited due to parasitic capacitance between wires in the back end. The dielectric constant, or κ value, of the insulator between wires can be reduced to shorten this delay. To reduce the dielectric constant of standard SiO_2 , carbon can be added to form bonds that are not as polar, and the material can be made porous, introducing air with its low κ value. These are generally referred to as SiCOH materials. Porosity, however, is achieved at the expense of modulus, meaning that the lower the κ value of a given SiCOH material, the weaker and less useful it is in industry.

Our group hoped to use millisecond laser spike annealing (LSA) to produce a stronger but still low- κ material. Annealing was performed at higher temperatures than conventional thermal anneals, with the short duration limiting many of the damaging material changes.

LSA involves focusing a high-power laser, and then tracing a line across the sample. By varying the dwell (the amount of time any particular region is heated) and laser power, different maximum anneal temperatures can be achieved. The beam intensity (and therefore, anneal temperature) follows a Gaussian profile. Consequently, temperature varies with position, with the highest temperature in the center of the line, as shown in Figure 1. This project involved characterizing the etch behavior of SiCOH films after laser heating.

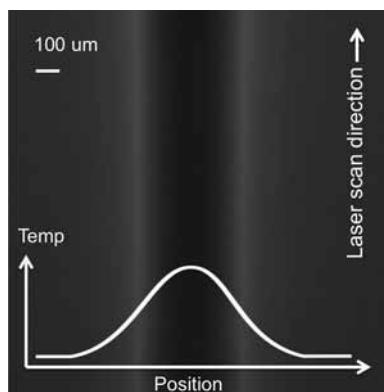


Figure 1: A representative diagram of a laser anneal stripe.

Experimental Procedure:

A 2×2 cm sample was annealed using a CO_2 laser at dwells ranging from 0.2 to 2 ms, all with a maximum temperature of 1200°C . As the 1 ms and shorter dwell anneals exhibited signs of material failure, only the 2 ms dwell (power 50.2 W) and the 1.5 ms dwell (power 52.6 W) anneals were considered in subsequent steps. (The failure was likely due to heat transfer from previous anneals; had the 0.2 ms anneal been performed first and the 2 ms anneal performed last, the material may not have failed.)

Photoresist was patterned so that only a small area of the sample was exposed to any given etch process. Two reactive ion etches

were performed using an Oxford 82 etcher, both typical SiO_2 etches: CF_4 etch (30 sccm CF_4 , 40 mTorr, 150 W power) and CHF_3/O_2 etch (50 sccm CHF_3 , 2 sccm O_2 , 40 mTorr, 240 W). Both 30 and 60 second etches were performed, each on a new region of the sample. Profilometry measurements were taken laterally across the anneal line, before and after etching, using a P10 profilometer. (During data analysis, the average of every ten values was plotted to reduce noise.)

A film appeared on the sample post resist removal. Following all CF_4 and CHF_3/O_2 etches, the part of the sample containing all of the etched regions was exposed to oxygen plasma (50 sccm O_2 , 60 mTorr, 150 W) for two 4-second intervals in the Oxford 82 in an attempt to remove this film. The remainder of the sample was covered in thick (S1827) resist. While the film removal was largely unsuccessful, enough was removed to allow for basic profilometry measurements.

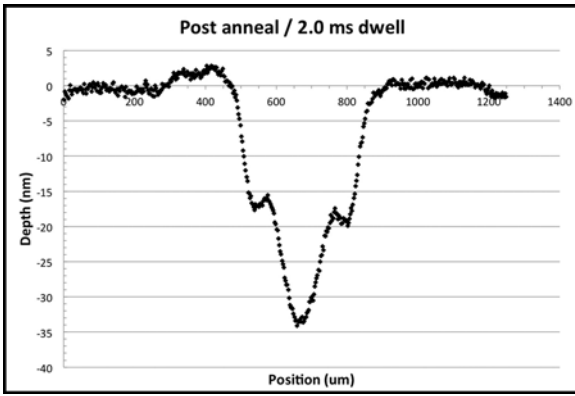


Figure 2: Depth vs. lateral position across the laser line (position as indicated in Figure 1).

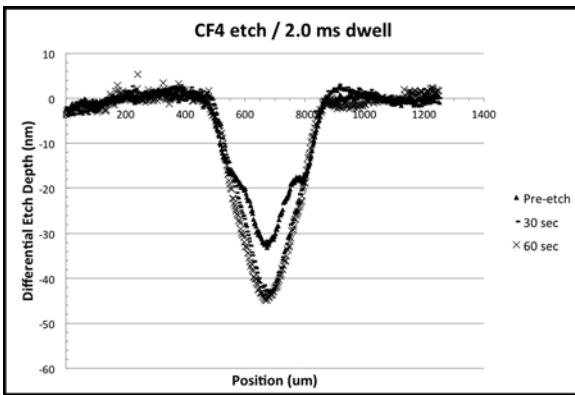


Figure 3: Differential etch depth vs. position for 2.0 ms dwell and CF_4 etch.

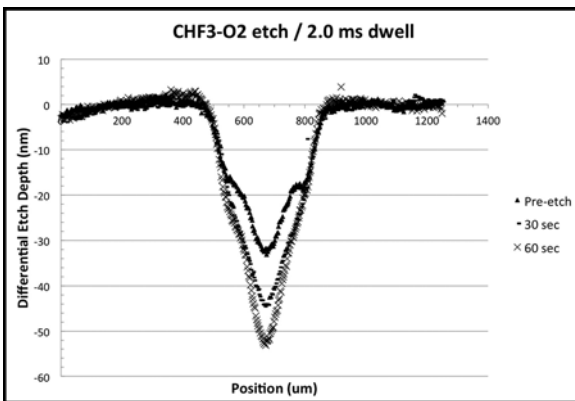


Figure 4: Differential etch depth vs. position for 2.0 ms dwell and CHF_3 / O_2 etch.

Results and Conclusions:

Figure 2 shows the change in depth with respect to position (and therefore temperature) across the laser line after anneal and before etch or oxygen clean. The material densified as it was heated, and the thickness of the film (originally about 200 nm) decreased. Of particular note are the two “shoulder” threshold regions, located at about 525-575 and 750-800 nm, where for a brief interval densification did not continue with increasing temperature.

After 30 and 60 second CF_4 etches, the surface profiles were virtually identical (as seen in Figure 3), indicating that at or some time before or at 30 seconds, the etch rate became uniform for all previous annealing temperatures. The shoulder regions also disappeared, hinting at the presence of a residue in the high temperature region (roughly between and including the shoulders) that etched away very quickly during initial etching, leaving behind only material that etched at a constant rate. The CF_4 etch profiles for 2.0 and 1.5 ms of dwell (not pictured here) were extremely similar, to the point that the etch behavior appeared to be independent of dwell.

The CHF_3/O_2 etch displayed slightly different behavior, with the shoulder regions remaining to an extent and a significant difference in the high temperature annealed region between the 30 and 60 second etch profiles, as seen in Figure 4. The residue appeared to take more than 30 seconds in order to etch, with a continued higher etch rate in the high temperature region after 30 seconds. In addition, the 60 second etch profile for 1.5 ms dwell (not pictured here) had a maximum depth of approximately -48 nm as opposed to approximately -53 nm.

Our hypothesis is that laser annealing leaves behind a residue in the high-temperature regions, possibly decomposed organic material, which is rapidly etched away so that only a material that etches at a uniform rate is left behind.

Acknowledgments:

I would like to thank Professor Thompson and my mentor Robert Bell, as well as the staff of the Cornell NanoScale Facility for their help. I would also like to acknowledge the National Science Foundation and the National Nanotechnology Infrastructure Network Research Experience for Undergraduates (NNIN REU) Program for funding this research.

Characterization of Single Component Molecular Glass Resists

Maike Blakely

Chemistry, Chatham University, Pittsburgh, PA

NNIN REU Site: Cornell NanoScale Science and Technology Facility, Cornell University, Ithaca, NY

NNIN REU Principal Investigator: Prof. Christopher K. Ober, Materials Science and Engineering, Cornell University

NNIN REU Mentor: Katherine Camera, Chemistry, Cornell University

Contact: mblakely@chatham.edu, cko3@cornell.edu, kc737@cornell.edu

Abstract:

Molecular glasses (MGs) are materials that exist in an amorphous state below their glass transition temperature, which allows us to study their glassy properties and behavior as photoresists. This research explored single component MG photoresists designed for future use in physical vapor deposition studies. This study investigated the critical doses, etch resistance rates, and electron beam lithography performance of three MGs. The CM-CR6 MG photoresist was identified as the most suitable candidate due to its relatively high etch resistance and high resolution patterning of 80 nm line and space patterns.

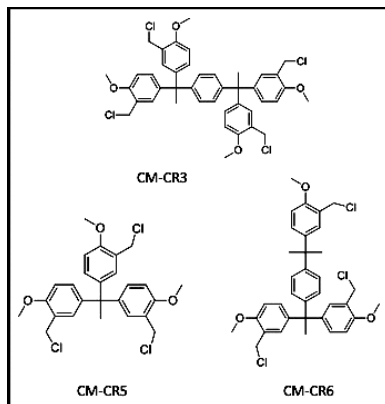


Figure 1: Structures of MG resists.

Introduction:

MG photoresists have specific characteristics like small molecular size, ability to form films, and high glass transition temperatures (T_g), which make them strong candidates for next generation lithography [1]. As polymeric photoresists are reaching their limits in feature size and roughness, attention has turned to small molecule photoresists like MGs [2]. To help optimize MGs in the lithography process, fundamental studies of their glass-forming properties can be explored using physical vapor deposition. For this, new single component molecular glasses must be designed and characterized before deposition studies are conducted. Figure 1 displays the chemical structures of the chloromethylated Cornell resists (CM-CR) that were studied. Using this model resist system, we can characterize their lithographic performance using contrast curves, etch resistance rates, and patterning through electron beam lithography.

Experimental Procedure:

The MG resist was dissolved in 2-butanone, making a 5 weight percent (wt%) solution. If necessary, 5 wt% with respect to resist of photoradical initiator, 2,2-dimethoxy-2-phenyl-

acetophenone (DPAP) was added to the solution. The resist was filtered through a 0.2 μm membrane filter onto a HDMS primed silicon wafer and spun at 2000 rpm for one minute. The wafer then underwent a post apply bake for one minute at 100°C.

For the contrast curves, the resist was first flood-exposed using the ABM contact aligner with 254 nm broadband light, and developed for one minute in 1-butanol. The film thickness was then measured as a function of dose using the Woollam spectroscopic ellipsometer. For the etch resistance studies, the resists were flood exposed as mentioned previously, and then plasma etched on the Oxford 80+ plasma etcher for varying amounts of time. Film thickness was measured as a function of

etch time, and the rate determined in nanometers per minute. To study the patterning capabilities of the photoresists, they were exposed using the JEOL 9500 electron beam (e-beam) lithography system. Their performance was evaluated using scanning electron microscope images, and SuMMIT software was used to calculate the line edge roughness (LER) and line width roughness (LWR).

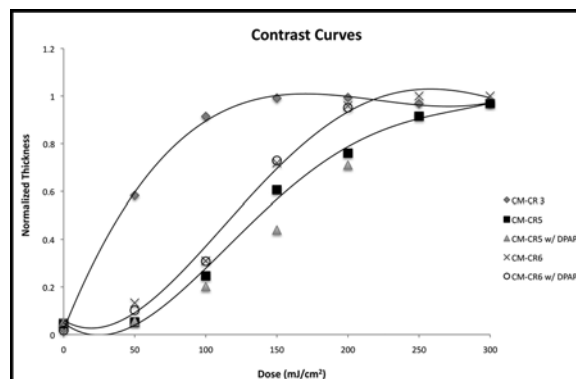


Figure 2: Contrast curves.

Results and Conclusions:

The contrast curves for the three MGs are shown in Figure 2. They did not display a desired steep slope, however the critical doses were identified for CM-CR3, CM-CR5, and CM-CR6 as 150 mJ/cm², 300 mJ/cm², and 250 mJ/cm² respectively. The addition of DPAP did not affect the critical dose of CM-CR5 or CM-CR6, and therefore, the experiment was not carried out with CM-CR3. This deep ultra-violet light behavior is not ideal however; this information is essential for quick testing of other properties.

The etch resistance of each resist were measured and compared to poly(hydroxystyrene) (PHOST), an industry standard (Figure 3). With CHF₃/O₂ etch gas, the etch resistance rates of the three MGs were the slowest and are comparable to PHOST, making CHF₃/O₂ the most favorable etch gas for this system.

The e-beam patterning performance is one of the most important aspects of these MGs. CM-CR6 showed patterns down to 80 nm 1:1 line:space with a low LER of 3.8 nm and LWR of 5.9 nm. The addition of DPAP allowed for comparable results using less than half of the original required dose, as seen in Figure 4. CM-CR3 was also able to pattern down to 80 nm 1:1 line:space, but had higher LER (5.0 nm) and LWR (9.3 nm) compared to CM-CR6. CM-CR5's performance was poor compared to CM-CR3 and CM-CR6, as it was only able to pattern down to 150 nm 1:1 line:space.

From these results, CM-CR6 was recognized as the most suitable resist for future use, due to its e-beam patterning performance and its proficient etch resistance. Future Work In general MG photoresists have shown promise but have not been optimized. Therefore future characterization and further optimization is needed to make MG photoresists a viable option for next generation lithography.

Acknowledgements:

I would like to thank the National Science Foundation, National Nanotechnology Infrastructure Network REU Program and the Cornell NanoScale Science and Technology Facility. A special thanks to Rob Iliac, Daron Westly, Melanie-Claire Mallison, and the Ober group especially my mentor, Katherine.

References:

- [1] Shirota, Y. J. Mater. Chem. 2005. 15, 75-93.
- [2] Dai, J., Chang, W., Hamad, A., Yang, D., Felix, N., Ober, C.K. Chem. Mater. 2006. 18, 3404-3411.

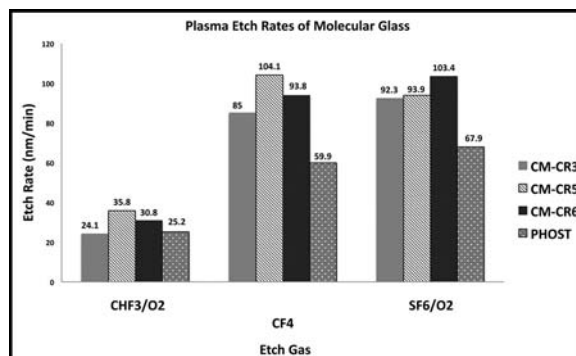


Figure 3: Etch resistance study.

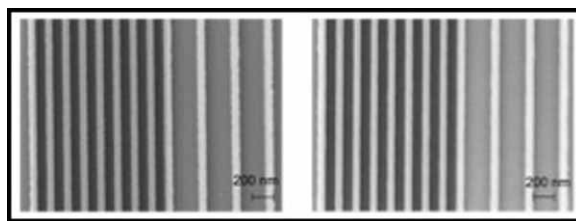


Figure 4: SEMs. Left: CM-CR6 without DPAP with a dose of 1250 mJ/cm². Right: CM-CR6 with DPAP with a dose of 500 mJ/cm².

Silver Nanoplates; Structural Stability and Optical Properties

Tyler Burkett

Chemical Engineering, University of Florida

NNIN REU Site: Nanotechnology Research Center, Georgia Institute of Technology, Atlanta, GA

NNIN REU Principal Investigator: Dr. Dong Qin, Materials Science and Engineering Department, Georgia Institute of Technology

NNIN REU Mentor: Graham Parkinson, Materials Science and Engineering Department, Georgia Institute of Technology

Contact: tburkett55@ufl.edu, dong.qin@mse.gatech.edu, grahamdbp@gatech.edu

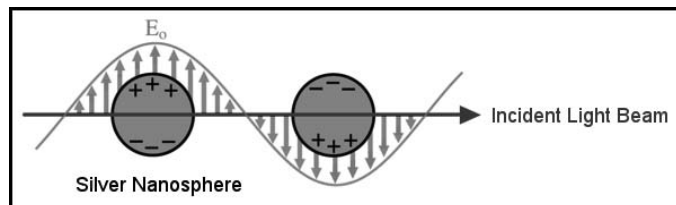


Figure 1: A figure explaining the optical properties of a generic nanoparticle. The example is using a silver nanosphere, with the incident light beam shown as a arrow and the electrical component of the light labeled E_0 .

Abstract and Introduction:

Silver nanoplates have attracted significant attention in the nanomaterials community for their numerous possible future uses. These nanoparticles are classified as ‘plates’ because they have high aspect ratios. Their edge lengths can be made to be between 30 and 500 nm, and they are typically triangular in shape. These plates exhibit interesting optical properties, because they are smaller than the wavelengths of incident light. Because of this, the conduction electrons of the nanoparticles interact and oscillate with the electrical component of light. The oscillation is what allows for these distinct optical properties and it also allows for distinct colors to be shown for different structures. This explanation can be seen clearly in Figure 1.

The material of silver was chosen for several reasons. One is that it is cheaper than other materials, specifically platinum and gold. A sizeable portion of the research of nanoparticles has been done using gold, which is more expensive. Another is that silver is highly electrically conductive. Also the silver nanoplates that are produced in the Qin Lab [1] are ideal for these studies. With the absence of a strong capping agent such as citrate, we can manipulate the shape, size, and local environment of these nanoplates and test optical effects.

It has been seen that any change in structure of these nanoplates creates changes in optical properties. These changes can be seen visually through a color change and can be quantified through UV-vis spectra. Also morphology is verified with scanning electron microscopy (SEM) and transmission electron microscopy (TEM). Understanding this ‘building block’ of nanoscience is a key step towards utilizing metallic nanomaterials in more intricate applications.

Experimental Procedure:

The first objective involved the synthesis of silver nanoparticles with ~ 50 nm edge-lengths. Chemically, this synthesis involved the reduction of ionic silver to atomic silver. As the process occurred, silver nucleation sites were created, which then grew into plates. The process involved has been honed to have anion-to-solid conversion greater than 99% [1]. The starting materials were silver nitrate (AgNO_3), which is the source of silver, and polyvinyl pyrrolidone (PVP), both dissolved in ethanol. PVP is the chemical that acts as the reducer and also is called a capping agent, because it binds to the surface of the nanoplate and allows it to remain relatively stable. The mixture of these ingredients was then placed into a Teflon® liner, which was sealed into a stainless steel vessel. This vessel was then placed into an oven for 4-5 hours.

Results and Conclusions:

Experiments with these as-prepared silver nanoplates included vertical and lateral growth experiments. Vertical growth was created with a very fast injection rate of more ionic silver with the presence of mild reducers, including PVP. This process successfully created bipyramidal nanoparticles. This showed a color change from blue to yellow. Slowing the injection rate

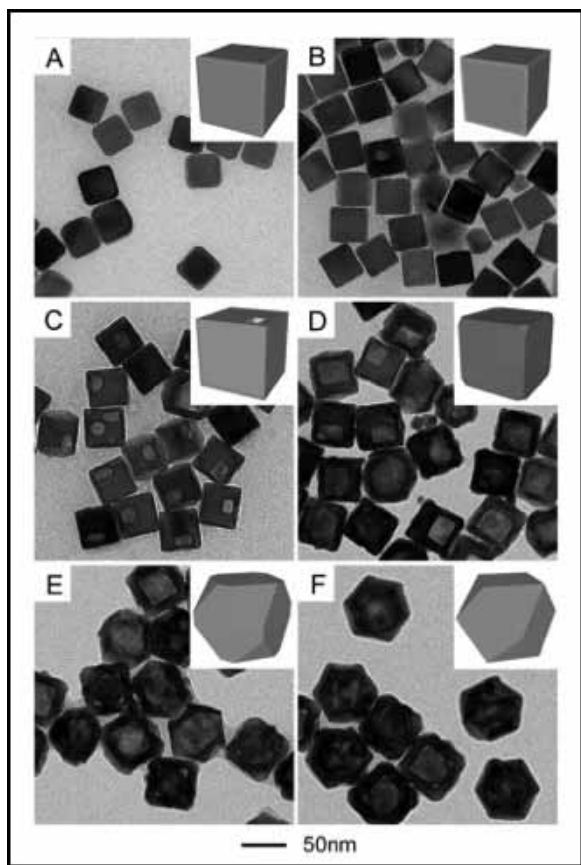


Figure 2: A collection of TEM images and illustrations showing silver nanocubes (A) coated with increasing amounts of gold (B through F). Deposition occurs first around the edges (B) before alloy structures are formed (C and D), eventually resulting in a gold shell (E and F).

allowed for a switch from vertical growth to lateral growth. This process successfully created larger plates with edge-lengths of 300 nm and visually showed a shift of color from blue to green.

Smaller nanoplates were produced in an ethanol system and were relatively stable. However, in water, they were typically unstable and selectively etch at the corners. This etching created truncated corners and hexagonal shapes. Etching occurred at corners because sharp corners have the highest chemical energy. These plates were tested with tap water and salt water. It has been shown that even a very small addition of chlorine ions can create this truncation and a large color change.

Stability is key for other future application. Stabilizing these nanoparticles may be achieved with a thin gold coating; a technique previously achieved with nanocubes, seen in Figure 2. This synthesis involves using nanocubes created by the lab group, ionic gold, and ascorbic acid as the reducing agent.



Figure 3: Silver nanoplates deposited onto the surface of PDMS. This is the first step towards flexible electrodes that utilize these plates.

When this knowledge was beginning to be transferred to nanoplates, the goal was to create the thinnest full coating of the plate.

Future Work:

The instability of plates in the water provides promising future applications in sensing and bio-sensing because of the drastic changes in color produced by small additions of ions. Once all knowledge of platecoating is transferred to silver nanoplates, these stable nanoplates can then be applied to several different applications. One notable application that is promising is metallic ink; because of their electric conductivity and the variety of colors that can be produced. Another application that was explored was flexible electronics.

The first steps towards this goal were taken with the deposition of these plates onto PDMS, a flexible substrate, seen in Figure 3. Popular possible types of flexible electronics include, flexible computers, electronics within fabric, and medical implants such as a pacemaker that can mold to the shape of the patient's body.

Acknowledgments:

Thanks to the NNIN REU Program, the NSF and the Institute for Electronics and Nanotechnology (IEN) for their support. Specifically I would like to thank the NNIN REU site coordinator at Georgia Tech, Leslie O'Neill, as well as Dr. Nancy Healy. It has been a privilege to work this summer with Dr. Dong Qin under the mentorship of Graham Parkinson.

References:

- [1] Zhang, Q.; Yang, Y.; Li, J.; Iurilli, R.; Xie, S.; Qin, D. ACS Appl. Mater. Interfaces, 2013, 6333-6345.

Low-Temperature Cu Segregation and Oxidation in Microwaved Ag-Cu Alloys

Brandi T. Burton

Physics, Norfolk State University

NNIN REU Site: ASU NanoFab, Arizona State University, Tempe, AZ

*NNIN REU Principal Investigator: Dr. T. L. Alford, Department of Chemistry and Biochemistry,
and School for Engineering of Matter, Transport and Energy, Arizona State University*

*NNIN REU Mentors: Mr. Sayantan Das, Department of Chemistry and Biochemistry, Arizona State University;
Mr. Benjamin Roos, School of Engineering of Matter, Transport and Energy, Arizona State University;
Dr. A. Lanz, Department of Mathematics, Norfolk State University*

Contact: b.t.burton@spartans.nsu.edu, ta@asu.edu, sdas30@asu.edu, bravokiloromeo@gmail.com, dr.l.lanz@gmail.com

Abstract:

Samples of a silver-copper (Ag-Cu) alloy of 13% Cu were annealed in a microwave cavity for up to 200 seconds, with a maximum temperature of 80°C. Rutherford backscattering spectrometry (RBS) indicated copper segregation to the surface. Oxygen resonance analysis and x-ray diffraction (XRD) showed that a thin copper oxide layer began forming on the surface at 40 seconds and completed at 80 seconds. Four-point probe measurements showed a decrease in the sheet resistance and XRD suggested that subsequent annealing resulted only in additional Ag grain growth.

Introduction:

Microwave processing has gained, and is gaining, much attention regarding materials processing due to its ability to process materials at low temperatures, and its efficiency in respect to time and energy savings, which lead to monetary savings [1]. Silver is a great conductor and has a high electromigration resistance [2], however, silver particles tend to cluster at high temperatures and oxidize in certain environments. To control these downsides, it is vital that an encapsulation layer be formed, in a sense, to protect the silver.

In this paper, it is noted that the copper will diffuse out of the alloy and react with ambient oxygen to form a copper oxide layer, which will act as an encapsulation layer protecting the silver from agglomeration and oxidation [3].

Experimental Procedure:

An Ag(Cu) alloy was fabricated by co-sputtering pure, 99.99%, Ag and Cu targets onto a silicon (Si) substrate with a previously deposited 100 nm thick silicon nitride (SiN_x) layer. The SiN_x layer ensured that the silver did not diffuse into, or agglomerate on, the Si substrate. The alloy structures were heated in a

2.45 GHz microwave cavity for up to 200 seconds. The temperatures of the samples were recorded using a Raytek low-temperature pyrometer. The resistivity of the samples, taken before and after the heating, was measured using a four point probe. RBS measurements using the RUMP simulation program determined the thickness and composition of the alloy. Glancing angle x-ray diffraction (XRD) measurements confirmed the phases of the alloy.

Results and Conclusions:

Glancing angle x-ray diffraction, using Cu $K\alpha$ particle radiation, at a wavelength of 1.54Å, rendered the preferential orientation for the alloy. An asymmetrical omega-two-theta scan was performed on the as-deposited and the 200 second annealed samples. JCPDS x-ray card number 04-0783 confirmed the defined Ag $\langle 111 \rangle$ and $\langle 220 \rangle$ peaks for both samples. Figure 1 shows that the Ag $\langle 111 \rangle$ and $\langle 220 \rangle$ peaks became narrow after annealing, suggesting that the alloy gained a better crystalline structure. We contributed the narrowing of the peak to be evident of the grain growth of the underlying silver layer.

RBS spectra, portrayed in Figure 2, showed an oxygen peak for the annealed sample only. RBS measurements showed that as the heating continued, the oxygen peak increased, indicating the formation of a thicker oxide layer. Figure 3 shows that as the heating time increased, the copper segregated to the surface of the alloy; also the front edge of the silver layer moved back, providing evidence that copper oxide formed on the surface of the alloy. By simulating the data using the RUMP program, we were able to determine how much copper remained in the alloy after annealing. Initially at 13% in the as-deposited sample, the copper decreased to 3% after 200 seconds of annealing. A more detailed analysis of the percent of residual copper per anneal time is detailed in Table 1.

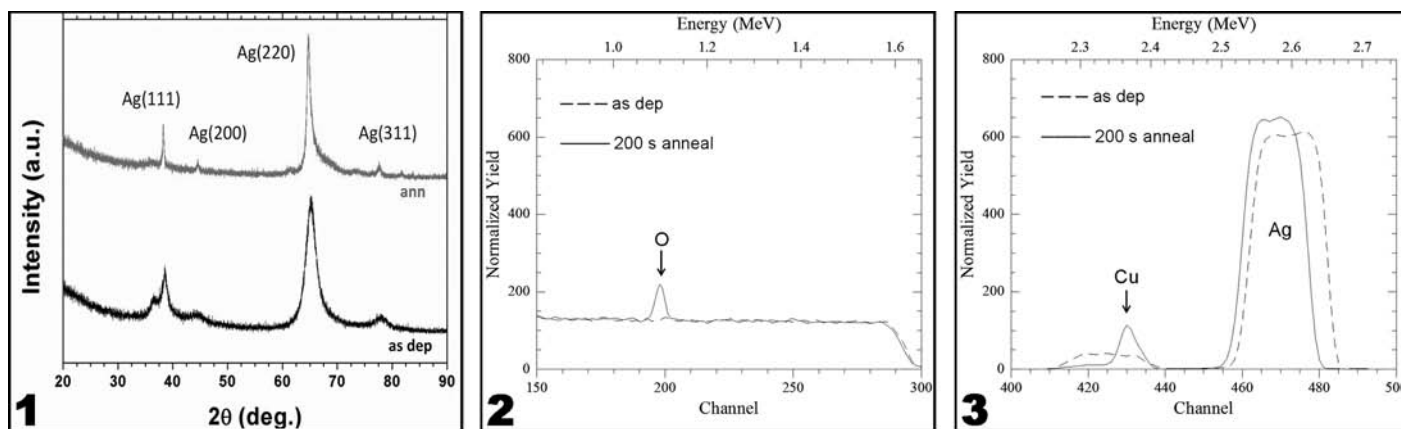


Figure 1, left: Glancing angle XRD measurements suggests the alloy's preferential orientation.

Figure 2, center: The RBS spectra for the as deposited and 200 second annealed samples highlighting the oxygen peak.

Figure 3, right: The RBS spectra for the as deposited and 200 second annealed samples highlighting the copper and silver peaks.

A four-point-probe was employed to measure the sheet resistance of the samples before and after heating. The sheet resistance decreased as the annealing time increased. Combined with the thickness measurements from RBS and RUMP simulations, the resistivity of each sample was approximated. The resistivity measurements, with respect to various anneal times is also described in Table 1. Since the newly formed copper oxide layer was considered to be an insulator, this decrease in resistivity can be attributed to the grain growth of the underlying silver layer. The grain size of both the as-deposited sample and the heated sample for 200 seconds were approximated using the Debye Scherrer Equation. It approximated that the grain size of the silver layer did increase from 39 nm to 111 nm.

Microwave annealing proved to be a sufficient method for annealing thin metal films. It promotes a processing technique that provides short processing times and efficiency. Ag(Cu) alloy structures at 13% percent copper, annealed at temperatures below 80°C for times ranging between zero to two minutes did prove to have enhanced electrical properties.

Future Work:

X-ray photoelectron spectroscopy measurements will determine whether a copper (I) oxide or copper (II) oxide formed on the surface of the alloy.

Acknowledgments:

I would like to thank my PI, Dr. T. L. Alford, and my mentors Mr. Sayantan Das, Mr. Benjamin Roos, and

Dr. A. Lanz for their assistance and guidance. I would also like to thank Dr. Trevor Thornton, and the National Nanotechnology Infrastructure Network Research Experience for Undergraduates (NNIN REU) Program, the National Science Foundation, and the Center for Solid State Electronics Research at Arizona State University for research support and funding.

References:

- [1] Das, S., Alford, T. L; Materials Letters, 89, 163-165 (2012).
- [2] Zeng, Y., Chen, L., Zou, Y., Nguyen, P., Hansen, J., Alford T. L; Materials Chemistry and Physics, 66, 77-82 (2000).
- [3] Akepati, S., Cho, H., Lee, K; "Growth of ultrathin Ag films of TaN_x layer and their optical properties." (to be published).

Microwave Processing Time	Resistivity	% of Residual Cu
0 s	5.63 μΩ cm	13%
40 s	3.60 μΩ cm	9%
80 s	3.32 μΩ cm	6%
120 s	3.37 μΩ cm	3%
200 s	3.21 μΩ cm	3%

Table 1: As the heating time increases, the resistivity and the percent of residual copper decreases.

Development of Platinum Embedded in Reduced Graphene Oxide (Pt@rGO) for Fuel Cell Applications

Michelle Chen

Chemical Engineering, Cornell University

NNIN REU Site: UCSB Nanofabrication Facility, University of California, Santa Barbara, CA

NNIN REU Principal Investigator: Prof. Daniel E. Morse, Institute for Collaborative Biotechnologies,

Department of Molecular, Cellular, and Developmental Biology, University of California, Santa Barbara

NNIN REU Mentor: Dr. Chang Sun Kong, Center for Energy Efficient Materials, University of California, Santa Barbara

Contact: mc2258@cornell.edu / michelle.chen888@yahoo.com, d_morse@lifesci.ucsb.edu, cskong@icb.ucsb.edu

Introduction:

For the past century, researchers have been searching for an environmentally friendly alternative energy conversion device to replace the antiquated 18th-century internal combustion system. One of the most promising and emerging alternative energy conversion devices is the polymer electrolyte membrane fuel cell (PEMFC). The hydrogen fuel cell essentially converts hydrogen gas and oxygen gas into water while producing electrical energy, rendering this system significantly more environmentally attractive [1]. Some of the reasons that this system is not implemented today include its high cost and relatively low efficiencies from its catalyst layer, compared to its combustion system counterpart. Conventionally, the catalyst layer is composed of a supporting matrix of porous carbon black and platinum (Pt). Platinum serves the pivotal role as the catalyst, converting the incoming hydrogen gas into its hydronium ions and electrons. Once the platinum is embedded within the carbon black, some of carbon black's pores close during synthesis, rendering the platinum nanoparticles inside the pores useless.

Instead of using a porous carbon material, we will be employing reduced graphene oxide (rGO), a planar carbon structure, to maximize the efficiencies of Pt in fuel cell's catalyst layer. The aggregation of Pt particles on the carbon composite is still one of the imminent obstacles for hydrogen fuel cell integration; this

conglomeration decreases the catalyst efficiencies in the catalyst layer [2]. Different concentrations of stabilizers, such as Nafion ionomer and polyvinylpyrrolidone (PVP) were employed to prevent aggregation of Pt nanoparticles. Nafion ionomer is a sulfonated tetrafluoroethylene based fluoropolymer with a hydrophobic backbone and with hydrophilic side chains. In solution, Nafion ionomer forms micelles due to its amphiphilic property. PVP is a water soluble polymer with the ability to quickly form thin films. Because of this property, PVP can coat other molecules. These two dispersing agents lower the tendency for Pt nanoparticles to conglomerate. An increase Pt nanoparticle conglomeration would in turn lower the effective surface area of Pt and hence decrease catalytic activity in the hydrogen fuel cell.

Experimental Procedure:

We added 33 wt% PVP, 60 wt% PVP, and 33 wt% PVP and 2.5 vol% Nafion in Sample 1, 2 and 3 respectively. The solutions underwent catalytic vapor diffusion and heat treatment at 500°C. The composites were then observed under the scanning electron microscope (SEM), x-ray diffraction (XRD), and cyclic voltammetry (CV).

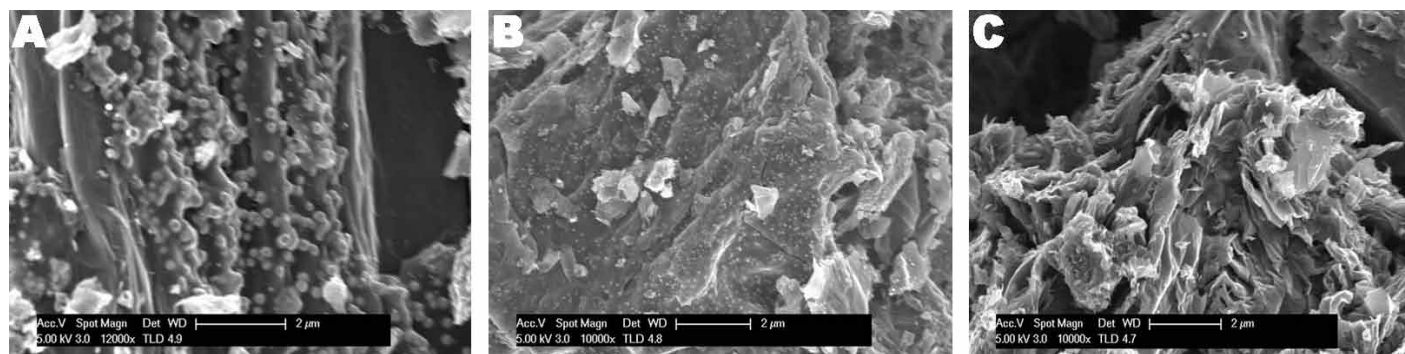


Figure 1: a) Scanning electron microscope (SEM) of Sample 1 containing 33 wt% PVP; b) SEM of Sample 2 containing 60 wt% PVP; c) SEM of Sample 3 containing 33 wt% PVP and 2.5 vol% Nafion ionomer.

Results and Conclusions:

The samples were observed through the SEM to visually understand the Pt behavior in each of the samples. In Figure 1 a), Sample 1 displayed Pt aggregation on rGO surface. With 2 μm as the resolution, the aggregated particles were estimated to be ~ 100 nm average in diameter. In Figure 1 b), the SEM image displayed significantly less Pt aggregation on the rGO surface for an increase of PVP. In Figure 1 c), an inclusion of a low concentration of Nafion depicted no visible Pt nanoparticle aggregation at a 2 μm resolution.

Each aggregated Pt particle was composed of the amalgamation of Pt nanoparticles. The average crystalline size of the aggregated particles can be calculated using the Scherrer equation for XRD data. From the summarized data in Figure 2, the Pt crystal size ranges from 5 nm to 9 nm in diameter of the Pt embedded in rGO (Pt@rGO) composites. The ACS amongst the three samples was relatively similar despite the different concentrations of stabilizing agents.

The efficiencies of the Pt in each sample were also observed with cyclic voltammetry (CV). CV was ramped from potentials of -0.4 V to 1.6 V with sweep rate of 10 mV/s. At negative potentials, the hydrogen oxidation reactions ($\text{H}_2 \rightarrow 2\text{H}^+ + 2\text{e}^-$) were measured. The total charge accumulated (proportional to the area underneath the cathodic peak) was converted into the amount of Pt surface area useful for oxidation purposes. A low concentration of PVP proved to have the lowest performance as it yielded the lowest effective surface area (ESA) of Pt. The inclusion of a low concentration of Nafion and PVP drastically increased Pt ESA. PVP was hypothesized to act as a coating layer over the Pt nanoparticles, sterically stabilized Pt nanoparticles from aggregating. Likewise, the behavior of Nafion ionomer at low concentrations could account for dramatic increase in performance. Nafion was composed of a hydrophobic backbone with hydrophilic side chains. In water-based solutions, Nafion ionomer formed micelles. These structures physically prevented Pt nanoparticles from aggregating. At a 2.5 vol% Nafion concentration, Nafion cluster size was large enough to prevent Pt conglomeration.

Sample	ACS ^[a] (d.nm)	ESA ^[b] (m ² /g)
Sample 1 (33 wt% PVP)	8.61	24.14
Sample 2 (60 wt% PVP)	5.45	28.50
Sample 3 (2.5 vol% Nafion + 33 wt% PVP)	6.76	40.85

Figure 2: Summary of results. Average crystal size (ACS) calculated from XRD data. Effective surface area (ESA) of Pt calculated from CV data.

Future Work:

The parameters are not yet optimized as these results are still preliminary results. Carbon black showed better performance than the current results, ranging from 40 m²/g - 100 m²/g as the Pt ESA. In the future, we will explore the efficiencies of platinum embedded in different carbon supporting matrix or varying the concentration of multiple dispersing agents to maximize the performance in rGO.

Acknowledgments:

I would like to thank Professor Dan Morse's group and the UCSB NNIN REU internship group for providing me with the necessary support and tools. I would personally like to acknowledge Dr. Chang Sun Kong for his unprecedented guidance during the 10-week internship. Finally, thank you to the National Nanotechnology Infrastructure Network Research Experience for Undergraduates Program for funding.

References:

- [1] "Fuel Cells." Fuel Cell Technology Program. U.S. Department of Renewable Energy, Nov. 2010. Web. 25 August 2013.
- [2] Nice, Karim; Strickland, Jonathan; "How Fuel Cells Work." How Stuff Works. Web. 25 August 2013.

An Experimental and Theoretical Investigation of Ultrasound Transmission in Bubbly PDMS Phononic Crystals

Caleb Christianson

Engineering Physics, University of Kansas

NNIN REU Site: Cornell NanoScale Science and Technology Facility, Cornell University, Ithaca, NY

NNIN REU Principal Investigator: Dr. Derek Stewart, Cornell NanoScale Science and Technology Facility, Cornell University

NNIN REU Mentor: Dr. Saikat Mukhopadhyay, Cornell NanoScale Science and Technology Facility, Cornell University

Contact: caleb.christianson@gmail.com, derek.stewart@cornell.edu, saikat.mukhopadhyay@cornell.edu

Abstract:

Phononic crystals are two- and three-dimensional structures with a periodic arrangement of two or more materials with different acoustic properties. Depending on the size, structure, and characteristics of the constituent materials, meta-materials with interesting acoustic properties can be formed. These crystals can be used to control the transmission of sound at selected frequencies, focus sound, or serve as waveguides. In this study, we investigated the transmission of ultrasonic waves through polydimethylsiloxane (PDMS) films with entrapped air bubbles. We examined how ultrasonic transmission through PDMS layers can be engineered by varying the dimensions, separation, and arrangement of air bubbles. We reproduced previously published data using two different theoretical models that describe ultrasonic transmission in air-PDMS crystals: (1) a simple scattering model for a series of partially reflective thin films, and (2) the code MULTTEL, which calculates the transmission solution using multiple scattering theory. We then used these models to predict the performance of new phononic structures by scanning a large parameter space. To create these structures, we first fabricated arrays of micron-scale pillars on a silicon wafer. PDMS layers were then cast on these pillar templates and stacked to form air bubble arrays with two- and three-dimensional periodicity. A series of processes were developed to stack layers of the crystals with unprecedented alignment. Finally, we measured the ultrasonic transmission through the films using a transducer/receiver setup in a water bath and compared it to the theoretical results.

Modeling Ultrasound Transmission:

We used two theoretical models to fit published experimental data [1] of a single PDMS layer with a square bubble lattice ($a = 300 \mu\text{m}$) and a four-layer PDMS stack with a tetragonal bubble lattice ($a_x = 300 \mu\text{m}$; $a_z = 350 \mu\text{m}$). The first analytic approach treats each bubble layer as a partially reflective plane and then iteratively calculates the reflection and transmission through all layers [1, 2]. We also used a more rigorous multiple scattering theory (MST) approach [3] where each bubble served as a scattering source for incoming ultrasonic waves. We found excellent agreement with previously measured values and the theoretical approaches gave consistent results for much of the

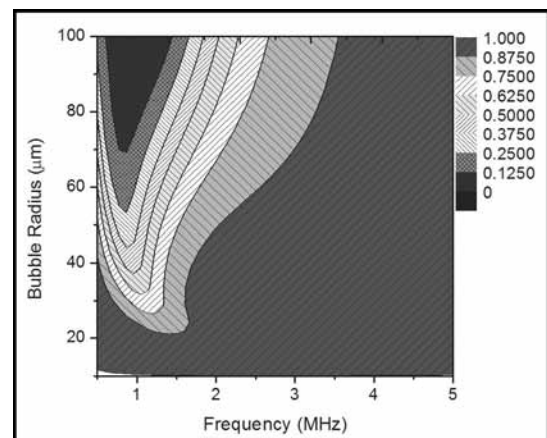


Figure 1: Contour plot of transmission for analytical model as a function of bubble radius and frequency. $N = 1$, $a_x = 300 \mu\text{m}$.

frequency range. We then used these models to explore a broad parameter space to determine the variation of transmission with the key parameters (e.g., number of layers, bubble radius and separation). Figure 1 demonstrates one such investigation, where we fixed the bubble separation and calculated the transmission up to 5 MHz as we varied the bubble radius up to $100 \mu\text{m}$. Using a similar approach, we showed that the crystal can be tuned to block certain frequencies. The blocked frequency followed the isolated bubble Minnaert resonance [4]. However, due to the bubble periodicity, we could tune the blocked frequency away from the Minnaert resonance by adjusting the in-plane bubble separation.

Phononic Crystal

Fabrication and Measurements:

After establishing our theoretical models, we set out to build the crystals to measure the transmission experimentally. Contact lithography was used to pattern an array of pillars on silicon and we then etched the wafer down $50 \mu\text{m}$. We then spun $350 \mu\text{m}$ of PDMS on the etched wafer, giving a flat, uniform film over the pillar array. PDMS was lifted off and stacked for ultrasonic measurements. Ultrasonic measurements were carried out in a

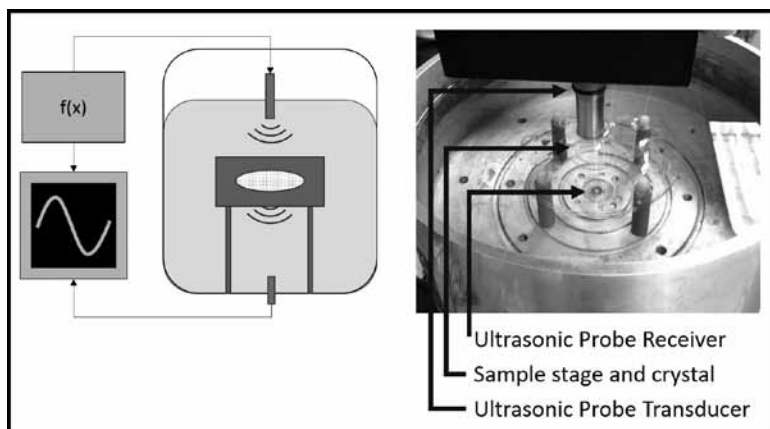


Figure 2: Schematic and image of the ultrasonic transmission experiments.

water chamber using a 10 MHz transducer positioned above the crystal (Figure 2). The ultrasonic waves were transmitted through the crystal, which was suspended on a sample stage, and the signal was then detected by a receiving probe at the bottom of the chamber.

Results and Conclusions:

A key challenge was the proper alignment of the bubble arrays in multi-layer films. Leroy et al. [1] described the alignment of the layers as, “a problematic issue” and their phononic crystal shows an offset between different bubble layers. Challenges include the inherent difficulties caused by the flexibility of the PDMS film, issues with entrapping errant air bubbles, adhering multiple PDMS layers, and perfectly aligning each layer. Figure 3 shows a top-down view of our well-aligned, two-layer film with the published two-layer film from Ref. [1] overlaid for comparison. Through a series of careful alignment procedures with a SUSS MA6/BA6 contact aligner, we were able to produce a two-layer crystal with no visible offset between bubble layers. After aligning two layers, we measured the ultrasonic transmission using the process described previously. Our transmission measurements for single- and two-layer films are plotted with our theoretical models in Figure 4. Overall, the measured transmission matches the trends expected from our theoretical models and from previously published data.

In this work, we have used two theoretical models to match published experimental data and also examine a broad parameter space for phononic crystals. We have fabricated single- and two-layer crystals and demonstrated better layer alignment than previously published work. Ultrasonic transmission measurements through these new crystals are comparable to our models and previous works.

Acknowledgments:

This work was supported by the National Science Foundation and performed at the Cornell NanoScale Facility, as part of the NNIN REU Program. Special thanks to Rob Ilic, Melanie-Claire Mallison, Christopher Alpha, Edward Camacho, Meredith Metzler, Beth Rhoades, Wolfgang Sachse, Michael Skvarla, Daron Westly, and Sam Wright.

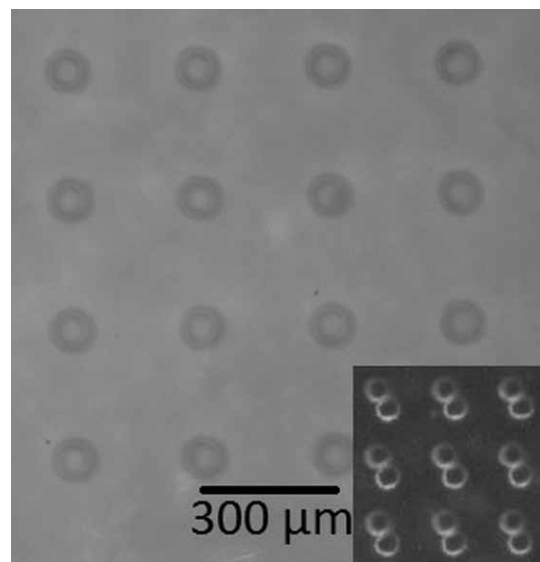


Figure 3: Micrograph of our two-layer film in comparison with previously published two-layer film [1] (inset).

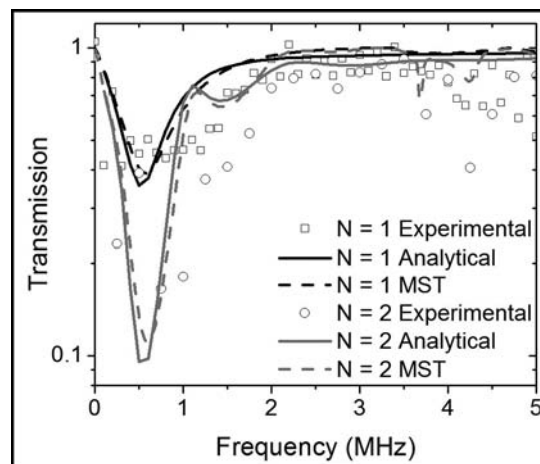


Figure 4: Transmission results for single- and two-layer films. $R = 39 \mu\text{m}$, $a_x = 300 \mu\text{m}$, and $a_z = 360 \mu\text{m}$.

References:

- [1] V. Leroy, A. Bretagne, M. Fink, H. Willaime, P. Tabeling, and A. Tourin, *Appl. Phys. Lett.* 95, 171904 (2009).
- [2] M. Devaud, et al., *Eur. Phys. J. E*, 32, 13 (2010).
- [3] R. Sainidou, N. Stefanou, I. E. Psarobas, and A. Modinos, *Comp. Phys. Comm.* 166, 197 (2005).
- [4] M. Minnaert, *Philos. Mag.* 16, 235 (1933).

Growth of Graphene on Various Substrates

Crystal T. Chukwurah

Biomedical Engineering, Duke University

NNIN REU Site: Howard Nanoscale Science and Engineering Facility, Howard University, Washington, DC

NNIN REU Principal Investigator: Dr. Gary L. Harris, Electrical and Computer Engineering, Howard University

NNIN REU Mentor: Mpho Musengua, Materials Science and Electrical Engineering, Howard University

Contact: crystal.chukwurah@duke.edu, gharris@msrce.howard.edu, mmusengua@yahoo.com

Abstract:

Graphene is a single layer of graphite. Its unique properties consist of chemical stability, high tensile strength, flexibility, and high thermal conductivity. These properties make graphene suitable for future applications such as hydrogen storage, lighter prosthetics, and flexible electronics. Past methods of graphene preparation such as exfoliation are efficient for lab purposes, but are not suited for mass production. With applications in mind, suitable substrates and methods for large quality graphene growth are necessary. This project focused on which methods of graphene growth are suitable for different substrates. Graphene was grown by the following methods: simple chemical vapor deposition (CVD), hot filament CVD, and radio-frequency plasma CVD. The methods were selected because they provide the option to use various substrates under unique conditions. From these methods, graphene growth was attempted on the following substrates: copper, 3C-silicon carbide on silicon, nickel, nichrome, and nickel films on 3C-silicon carbide. These substrates were selected for their strength, ductility, and resistance to corrosion and heat. The grown films were characterized using scanning electron microscopy (SEM) and Raman spectroscopy. Raman results have confirmed graphene on nickel films on 3C-silicon carbide, diamond nanoseeded nichrome, nickel foil, and annealed nickel foil by the hot filament CVD method. Ultimately, these results may uniquely contribute to the mass production of graphene on potentially any substrate.

Introduction:

Graphene growth is a fairly new technology and many growth methods are currently being evaluated. Popular techniques to form graphene include exfoliation, sublimation of silicon carbide, and CVD onto metal foils [1-3]. Exfoliation requires physically removing multiple layers of graphene to obtain single layer. The sublimation method is limited to silicon carbide and requires transferring to other substrates. CVD is practiced on metal foils at high temperatures to get quality graphene. Unfortunately, this limits graphene growth to only a select few substrates; of which, have little favorability for graphene applications. Enhanced CVD processes like hot filament CVD (HFCVD)

and radio-frequency plasma CVD (RFCVD), which uses hot filaments or a plasma to disassociate hydrocarbon gases, allow graphene to be grown on more substrates over a broader range of temperatures. With help from the filaments or the plasma, graphene growth no longer relies on the substrates to be at high temperatures. Enhanced CVD can grow graphene directly onto various substrates, which eliminates the transfer process and is valuable for mass production of high quality large area graphene.

Experimental Procedure:

In this work, graphene was grown on various substrates by the following methods: simple CVD, RFCVD, and HFCVD. The growth conditions are given in Figure 1. The various substrates (copper, 3C-silicon carbide on silicon, nickel, nichrome, and nickel films evaporated on 3C-silicon carbide) were pretreated through sonication in 1) trichloroethylene, 2) acetone, and 3) methanol for three minutes each. In pretreating the substrates, copper and nickel were annealed *in situ* under H_2 at $\sim 1000^\circ C$ from $\sim 0-40$ min. Additional trials were completed using other substrate pretreatments conditions namely: non-*in situ* annealed copper, unannealed substrates, and UV radiated substrates. With conventional CVD, graphene growth was attempted on copper and nickel substrates with the following growth conditions: $H_2/CH_4 = 3$ at $\sim 1000^\circ C$ for 10 min. With RFCVD, graphene growth was attempted on all substrates with the following growth conditions: $Ar/CH_4 = 19$ at $\sim 1000^\circ C$ for 5-10 min. With HFCVD, graphene growth was attempted on all substrates with

Growth Conditions	Simple CVD	RF CVD	HFCVD
Substrate Temperature	1000°C	1000°C	0-750°C
Filament Temperature	N/A	N/A	2100-2300°C
Gas Flowrates (sccm)	$H_2=5$ $CH_4(5\%)=35$	N/A	$H_2=30; 50$ $CH_4(5\%)=5; 10$
Gas Ratio H_2/CH_4	3	N/A	5; 60; 125
Gap Distance	N/A	N/A	15-45mm
Plasma Intensity	N/A	250-300 Watts	N/A
Pressure	0.3 Torr	1.3E-4 Torr	20-35 Torr
Anneal Time (min)	45 min	0-30 min	0-40
Growth Time (min)	10 min	5-10 min	5-10min

Figure 1: Graphene growth conditions for simple CVD, radio-frequency plasma CVD, and hot filament CVD.

the following growth conditions: H_2/CH_4 of 5, 60, and 125 from 5-10 min. Additionally, the substrate and filament temperatures for HFCVD were 0-750°C and 2100-2300°C, respectively. Uniquely, HFCVD's substrate temperature range was trialed for lower temperature growth.

Results and Conclusions:

The substrates were characterized using Raman spectroscopy and scanning electron microscopy (SEM). CVD and RFCVD method did not yield any graphene films. Raman results have confirmed graphene by HFCVD on nickel films on 3C-silicon carbide (Figure 2). The results correspond to multi-layer graphene. The SEM image of graphene grown on nickel films on 3C-silicon carbide shows graphene grain sizes on the order of 1-3 μm (Figure 3). Similar Raman results confirmed graphene by HFCVD on the following other substrates: diamond nanoseeded nichrome, nickel foil, and annealed nickel foil. The SEM image of graphene grown on nickel foil shows graphene grain sizes on the order of 30-40 microns (Figure 4).

Improper annealing of the copper substrate may explain the lack of graphene on copper. Lack of graphene by RFCVD may be due to the substrate temperature being significantly lower than the thermocouple reading due to heat loss. Future research will require a more extensive evaluation of the growth conditions for each system and what substrate properties are important in the formation of graphene. Also some effort will be required to increase grain size.

Acknowledgements:

I would like to thank the following for their support: PI Dr. Gary Harris, Research Mentor Ms. Mpho Musengua, Site Coordinator Mr. James Griffin, the staff at the Howard Nanoscale Science and Engineering Facility, the National Nanotechnology Infrastructure Network Research Experience for Undergraduates (NNIN REU) Program, and the National Science Foundation.

References:

- [1] Cai, Minzhen, et al. "Methods of graphite exfoliation." *Journal of Materials Chemistry* 22.48 (2012): 24992-25002.
- [2] de Heer, Walt A., et al. "Large area and structured epitaxial graphene produced by confinement controlled sublimation of silicon carbide." *Proceedings of the National Academy of Sciences* 108.41 (2011): 16900-16905.
- [3] Li, Xuesong, et al. "Graphene films with large domain size by a two-step chemical vapor deposition process." *Nano letters* 10.11: 4328-4334 (2010).

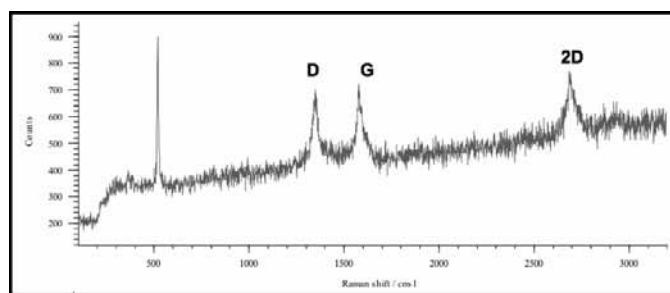


Figure 2: Raman spectroscopy results for 100 nm Ni film evaporated on SiC on Si grown by HFCVD.

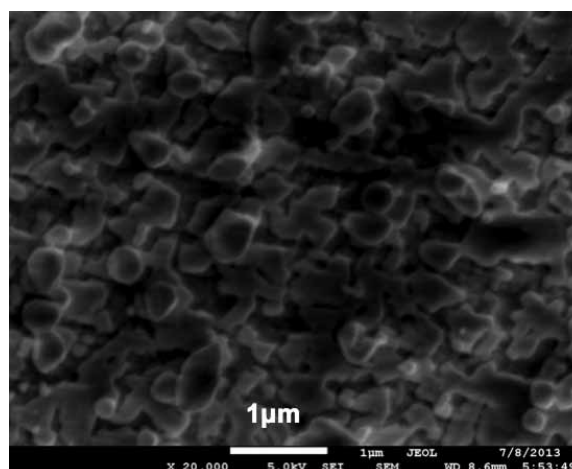


Figure 3: SEM image of graphene grown by HFCVD on 100 nm Ni film on SiC on Si.

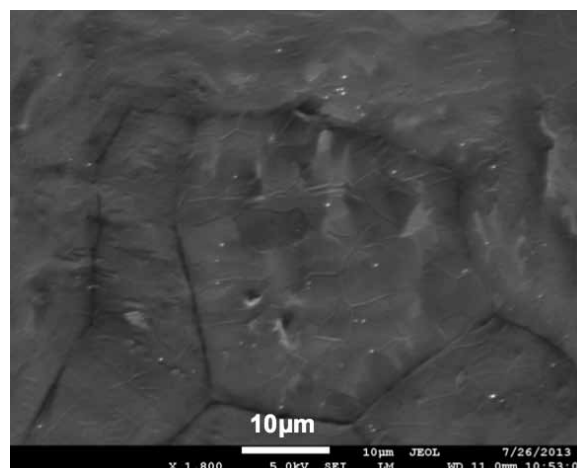


Figure 4: SEM image of graphene grown by HFCVD on Ni substrate.

Investigation of Microfluidic Integration in Magneto-Nanosensor Based Protein Biomarker Detection

Stephanie Cone

Biomedical Engineering, University of Arkansas

NNIN REU Site: Stanford Nanofabrication Facility, Stanford University, Stanford, CA

NNIN REU Principal Investigator: Professor Shan X. Wang, Electrical Engineering and Materials Science, Stanford University

NNIN REU Mentor: Daniel Bechstein, Mechanical Engineering, Stanford University

Contact: scone@uark.edu, sxwang@stanford.edu, bechst@stanford.edu

Abstract:

The use of magnetic nanoparticles in conjunction with a spin-valve type giant magnetoresistive (GMR) sensor provides a method for the detection and quantification of picomolar concentrations of proteins in biological samples. The magnetic nanoparticles act as a magnetic tag for proteins which allow the quantification of targeted proteins. Recent developments in the lab's custom microfluidic integration approach with the spin valve sensor array allow for simultaneous testing for multiple samples on a single chip and a variety of proteins within a given sample. In this work, testing is being conducted to study the distribution of magnetic nanoparticles following the completion of microfluidic assay experimental procedures. Specifically, the final locations and local densities of the magnetic nanoparticles and the presence of washing buffer fluid following the assay are being compared to the geometry of the microfluidic channels. The comparison of these patterns may lead to improvements in the efficiency and reproducibility of the bioassays.

An SEM was used as the primary source of images in this study. Some potential applications for this technology include multiplexing of surface interface sensors within automated point-of-care diagnostic devices.

Experimental Procedures:

Lab-on-a-Chip Devices. Lab-on-a-chip tools are self-contained devices that can run immunoassays on protein samples. These devices are useful for many reasons. One major benefit is their portability, which permits their use in remote locations that would otherwise require the transportation of samples for diagnostic tests. Another major point is that with small devices, very little material is required during a single

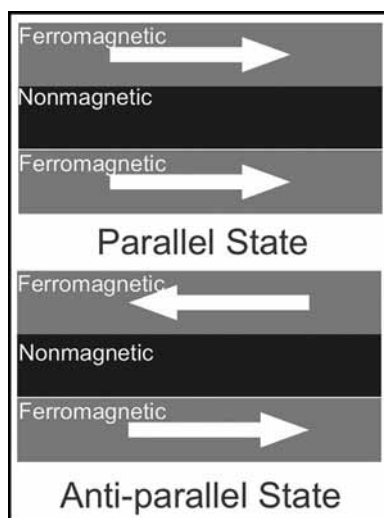


Figure 1: View of the magnetic parallel and antiparallel states.

test, leading to both lower material costs and the generation of less waste. Finally, there is often minimal training required for operators of such tools, as they are primarily self-contained, and highly automated.

Giant Magneto Resistance Sensors (GMR). GMR is a large change in resistance in certain materials and structures upon the application of a magnetic field. With the example of our sensors as pictured in Figure 1, the bottom ferromagnetic layer has a fixed magnetic field, while the field in the top ferromagnetic layer is switched between the parallel and anti-parallel states in order to induce a change in the magnetic field. The observed change in resistance is due to more electrons being scattered when they pass through the material in the anti-parallel state as opposed to the parallel state.

When magnetic nanoparticles, which act as tags for proteins, are added to the top of the GMR, the strength of the magnetic field is affected. This leads to a change in the magnetoresistance which is measured and normalized, resulting in the GMR acting as a sensor to analyze the sample composition.

Bioassays. Bioassays can provide information on the concentration of targeted proteins in samples. In these experiments, BSA was used as a negative control that produced no change in the magnetic resistance, biotin was the positive control that produced a very high signal, and test proteins were applied to sensors in a range of concentrations, resulting in a signal bands located between the controls.

Standard Well Assays. Standard well assays were performed by applying reagents in a preset order to a chip, and adding magnetic nanoparticles while the chip was located in the GMR sensor. These reagents included proteins and matching antibodies, magnetic nanoparticles, biotin, and BSA. Data from bioassays can be plotted in the format of change in

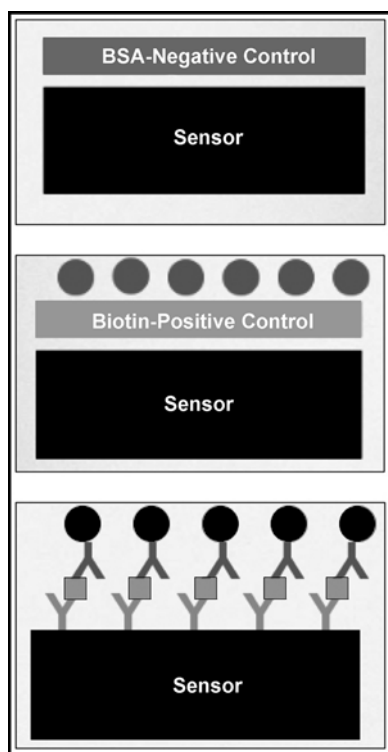


Figure 2: Negative control, positive control, and test biosensors with reagents attached.

magnetic resistance versus time. In Figure 2, the test protein was C-reactive protein, which is a common protein released as a part of the complement system in the inflammatory response. Throughout the summer, C-reactive protein and FLT3LG were both used as test proteins in various concentrations.

Following the bioassay, the results were recorded in the form of corrected change in magneto-resistance versus time. An example of this data can be seen in Figure 3.

Microfluidic Assays. When used in conjunction with GMR sensors, microfluidics could improve both the reliability and efficiency of bioassays. Some reasons for this are that the use of microfluidics can automate much of the bioassay procedure, it directs reagent material to the sensors, and it can provide separate channels, allowing for concurrent testing of multiple samples. The reliability of microfluidic testing depends on

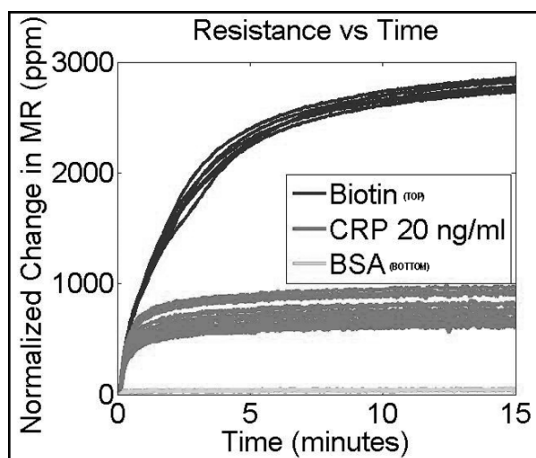


Figure 3: Data plot of corrected resistance versus time from standard well bioassay.

factors including the physical structure of the channels, the surface chemistry of the sensor, and the alignment of the chips.

Conclusions:

Multiple proteins were detected at picomolar concentrations through the use of GMR sensors and magnetic nanoparticles. Microfluidic channels were found to be an effective means of directing reagents along the surface of sensor chips. No cross-contamination was witnessed between the channels, meaning that a variety of tests could be run simultaneously on a single chip.

Future Work:

This research will be continued by the addition of tests involving new proteins, as well as experiments with an expanded range of concentrations, in order to better evaluate the sensitivity of the tool. More research and development will be done to increase the portability of the total diagnostic device, thus increasing its functionality as a Lab-on-a-Chip.

Acknowledgments:

I would like to thank CIS, NNIN REU, NSF, the REU staff at SNF, Daniel Bechstein, Professor Shan X Wang, and the Wang lab group for their assistance in this research.

References:

- [1] Gaster, R., et al.; "Matrix-insensitive protein assays push the limits of biosensors in medicine"; *Nature Medicine*, 15, 1327-1332 (2009).
- [2] Gaster, R., et al.; "nanoLAB: An ultraportable, handheld diagnostic laboratory for global health"; *Lab Chip*, 11, 950-956 (2011).
- [3] Osterfield, S., et al.; "Multiplex protein assays based on realtime magnetic nanotag sensing"; *PNAS*, 105, 20637-20640 (2008).

Ion Transport Through Porous Graphene

Katelyn Conrad

Biomedical Engineering, Arizona State University

NNIN REU Site: Colorado Nanofabrication Laboratory, University of Colorado, Boulder, CO

NNIN REU Principal Investigator: Professor Scott Bunch, Mechanical Engineering, University of Colorado at Boulder

NNIN REU Mentor: Lauren Cantley, Mechanical Engineering, University of Colorado at Boulder

(2010 NNIN REU at the University of Colorado at Boulder)

Contact: kmconra1@asu.edu, scottbunch@gmail.com, laurencantley@gmail.com

Abstract:

Graphene is a two-dimensional carbon material that is only one atom thick with exceptional strength and remarkable gas separation properties [1-3]. Graphene membranes have great potential for applications in DNA sequencing, desalination and water filtration, as well as lab on a chip processes. The focus of this project was to investigate the potential of graphene membranes for liquid separations. A microfluidic device was designed and fabricated to test graphene's separation properties in liquids. Chemical vapor deposition (CVD) graphene was freely suspended over a thin copper foil and attached to a polydimethylsiloxane (PDMS) microfluidic substrate. Suspended graphene was fabricated via standard photolithography while a PDMS substrate was fabricated via soft lithography techniques. To observe the permeability of graphene membranes, pressurized deionized water was introduced onto the underside of a graphene membrane through a microfluidic channel and the graphene membrane deflection was measured via atomic force microscopy (AFM) in air. Future work includes electrical testing of water and ionic transport across porous monolayer graphene membranes.

Introduction:

Graphene is a two-dimensional material made of carbon, the same material as the three-dimensional graphite that can be found in pencils. This material is only one atom thick, yet for being so thin, it has exceptional strength. In fact, it is the thinnest and strongest material known [1]. It has been found to have remarkable gas separation properties, and be impermeable to all molecules including helium when in its pristine form [2, 3]. Graphene membranes also have great potential for applications involving liquid separations such as DNA sequencing, desalination, and water filtration, as well as lab on a chip processes [4]. The focus of this project was to investigate the potential of graphene membranes for liquid separations.

Experimental Procedure:

In order to investigate the potential of graphene membranes for liquid separations, first the suspended graphene membrane was

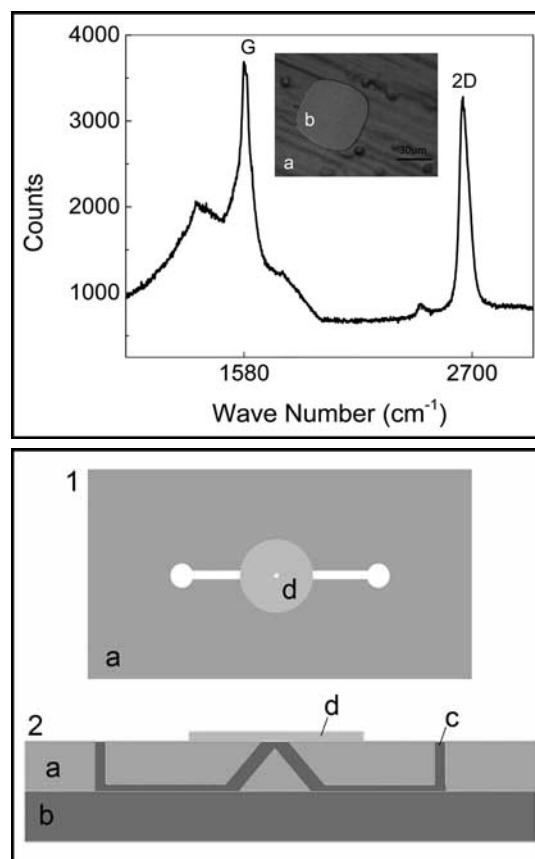


Figure 1, top: Optical image of the copper foil (a) containing suspended CVD graphene (b); Raman spectrum of the suspended CVD graphene.

Figure 2, bottom: (1) Top view of final device. (2) Side view of final device. Key: (a) PDMS (b) glass slide (c) DI water (d) copper.

fabricated. Graphene was grown on a thin copper foil via CVD. The copper was then patterned using standard photolithography techniques and etched by floating the copper in a 0.1M solution of ammonium persulfate. After floating in the etchant for three hours, the copper was inspected every half hour for the next one to nine hours until the copper with graphene on it became a

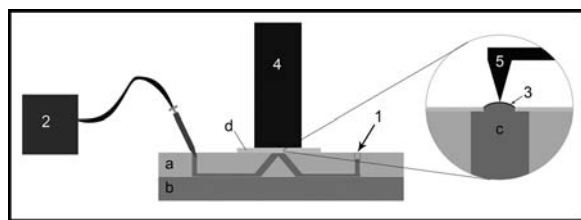


Figure 3: Experimental setup: One end of the channel was plugged with a piece of PDMS (1) and a pump was inserted in the other side of the channel (2). The deflection of the graphene membrane (3) was monitored using the AFM (4) by having the AFM tip (5) move across the surface of the membrane. Key: (a) PDMS (b) glass slide (c) DI water (d) copper.

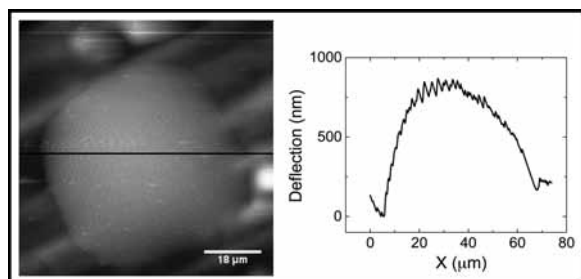


Figure 4: AFM data.

copper disc approximately 7 mm in diameter with a hole in the center approximately 15 μm in diameter, over which graphene was suspended. This copper disc was then critical point dried to avoid damaging the graphene membrane. Raman spectroscopy was used to confirm that graphene was suspended, as indicated by the G peak at approximately 1580 cm^{-1} and the 2D peak at approximately 2700 cm^{-1} , as shown in Figure 1.

The copper disc containing suspended graphene was then adhered to a microfluidic channel made from PDMS. The microfluidic channel was fabricated via standard soft lithography techniques and measured 50 μm deep and 500 μm wide with through holes 1.5 mm in diameter. The final device is shown in Figure 2.

Next, the graphene membrane was pressurized from below by pumping deionized water into the microfluidic channel. To do so, one end of the channel was plugged with a piece of PDMS and a syringe pump introduced deionized water to the other end of the channel, as shown in Figure 3. The effects of this pressurization were monitored using both optical and atomic force microscopy, as shown in Figure 4.

Results and Conclusions:

Initial tests were observed using only an optical microscope and revealed that when the underside of the membrane was pressurized to large values, the graphene quickly burst due to the large pressure difference. To decrease the pressure differential across the membrane, subsequent tests were carried out by pressurizing the graphene membranes at a slower rate. For the duration of these tests, the top surface of the graphene was monitored using AFM, as shown in Figure 3. AFM data revealed that when pressurized from below, the graphene membrane bulged up in response to the increased pressure difference, as shown in Figure 4. Changes in pressure were reflected in the deflection of the membrane. The ability to image the pressurized graphene membranes without the obvious penetration of water across the membrane is an indication that the CVD graphene membranes fabricated via the method described above are indeed impermeable to the transport of water.

Future Work:

The next step in this project will be to etch pores in the CVD graphene membrane using UV-ozone etching. The introduction of pores will allow for exploration into how water moves across porous graphene membrane as well as exploration into ion transport and molecular separation.

Acknowledgments:

I would like to thank the National Nanotechnology Infrastructure Network Research Experience for Undergraduates Program and the National Science Foundation for their support of this project. I would also like to thank Professor Scott Bunch, Lauren Cantley, the Bunch Research Group, and the Colorado Nanofabrication Laboratory for their guidance in this research.

References:

- [1] Geim, A. K. and Novoselov, K. S.; "The Rise of Graphene"; *Nature Materials*, 6, 183-191 (2007).
- [2] Bunch, J. Scott, et al.; "Impermeable Atomic Membranes from Graphene Sheets"; *Nano Letters*, 8.8, 2458-2462 (2008).
- [3] Koenig, Steven P., et al.; "Selective molecular sieving through porous graphene"; *Nature Nanotechnology*, 7, 728-732 (2012).
- [4] Garaj, S., et al.; "Graphene as a sub-nanometer trans-electrode membrane"; *Nature*, 467, 190-193 (2010).

Nanocharacterization of Wood Fibers in Cement

Christopher Florencio-Aleman

Materials Science and Engineering, Columbia University

NNIN REU Site: Nanotechnology Research Center, Georgia Institute of Technology, Atlanta, GA

NNIN REU Principal Investigator: Dr. Kimberly E. Kurtis, Civil and Environmental Engineering, Georgia Institute of Technology

NNIN REU Mentor: Passarin Jongvisuttisun, Civil and Environmental Engineering, Georgia Institute of Technology

Contact: cf2480@columbia.edu, kimberly.kurtis@ce.gatech.edu, p.jongvisuttisun@gatech.edu

Abstract:

Early-age cracking resulting from the absence of water is a major problem in high-performance concrete in which the low water-to-cement ratio is used. This is solved through internal curing methods where absorptive materials, such as saturated lightweight aggregates (LWAs) and super absorbent polymers (SAPs), are added to the cement mix to aid the hydration process. Because of its hygroscopic properties, natural fibers are a novel material in internal curing methods and have often been thought of as an inert material in cementitious composites. However, these fibers are not inert and the nanocharacterization of the cement-fiber system grants insight to the interactions between these fibers and the cement. Through this nanocharacterization, it has been determined that fiber is acting as both a nucleation site and as a semi-permeable membrane which interacts with the cement system and ultimately changes the kinetics of the hydration process.

Introduction:

In terms of worldwide resource consumption, only water is used in greater quantities as compared to concrete each year [1]. Early age cracking is one of the main problems high performance concrete faces due to the low water to cement ratio that is required to achieve high performance. High performance concrete is typically very dense and traditional methods of supplying water through external curing methods, where water is ponded on top of the concrete, are not very effective. A novel method to provide water to high performance concrete

is internal curing. These methods aid the cement hydration process by uniformly distributing a hygroscopic material throughout the concrete mix.

A novel material used to internally cure concrete is natural fiber. When evaluating the effect of fiber in ordinary Portland cement and white Portland cement, the calorimetry curves in Figure 1 have shown that fiber alters the systems in such a way that it not only aids cement hydration reactions, it also accelerates them to occur earlier in white cement. This suggests that the interactions between fiber and white cement at early ages mainly depends on the chemical composition of the cement.

There are two possibly ways in which the fiber may be interacting with the fiber; 1. The fiber's surface is acting as a nucleation site onto which cement hydration products are forming, and 2. The fiber could be acting as a semi-permeable membrane which changes the ion concentrations and therefore alter the kinetics of the reactions.

Experimental Procedure:

In order to determine certain aspects between these interactions, nanocharacterization techniques were applied in the form of inductive coupled plasma spectroscopy (ICP), scanning electron microscopy (SEM) images, atomic force microscopy (AFM), and x-ray photoelectron spectroscopy (XPS). ICP was used to determine the ion concentrations of both cements used to determine if chemical composition was a factor in these changes, SEM images were taken in order to determine if the fibers were acting as nucleation sites that facilitated the formation of cement hydration products, AFM imaging was used to survey the fiber surface and better understand the surface morphology, and XPS was used to determine ion concentrations at different depths to determine if the fiber was acting as a semi-permeable membrane which ultimately affected the kinetics of the system.

Results and Conclusions:

From the ICP ion analysis, different concentrations were determined for the gray and white cements. Gray cement pore solution was found to contain 60% potassium, 29% sulfur,

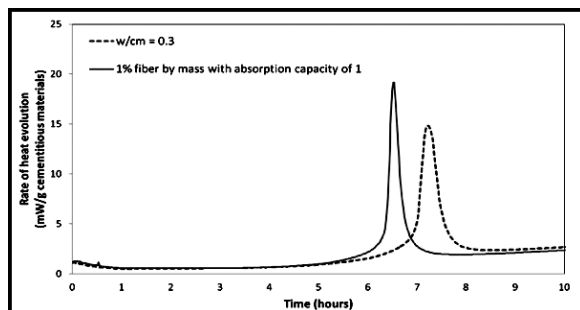


Figure 1: Heat released from the white cement paste compared with that of the fiber-white cement paste.

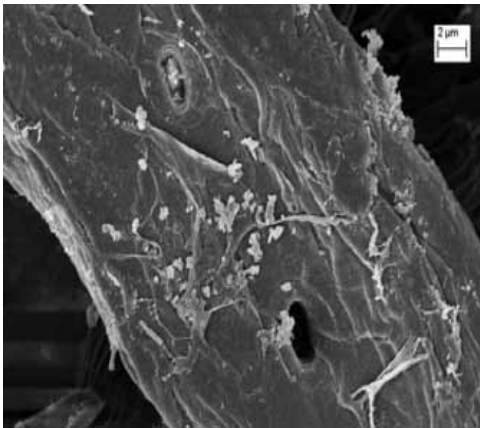


Figure 2: SEM image of fiber exhibits hydration product formation at 24 hour in cement pore solution.

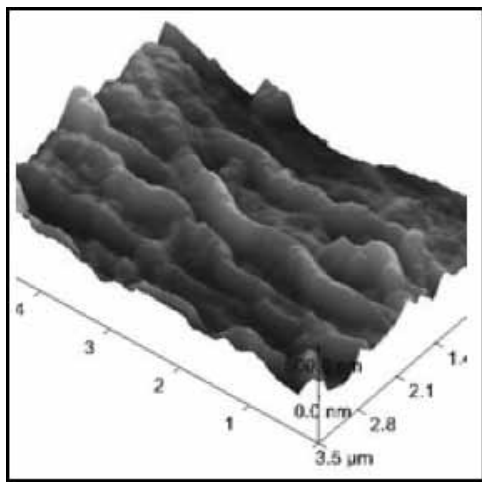


Figure 3: AFM 3D image of a detail of the fiber surface. Fiber features are about 500 nanometers in height.

8% sodium, and 3% calcium. In contrast, white cement pore solution contained 40% calcium, 23% sulfur, 19% potassium, and 18% sodium. Since the chemical composition of the cement pore solution was one of the factors which was hypothesized to be a primary factor of the acceleration in the cement, the calcium difference between the two cements should be noted as the primary difference.

From the SEM and AFM images, the fiber's rough surface could be observed. Further SEM images showed cement products forming onto the rough areas of the fiber. AFM imaging showed the rough features found on the fiber surface were about 1000 nanometers. There was no observable difference between the white cement and grey cement.

From XPS analysis, the main thing that should be noted is the difference in calcium ion concentrations at different depths. Again, there were no notable differences in our analysis between the gray and white cement. The importance of this was factored in when the membrane-like properties of the fiber were

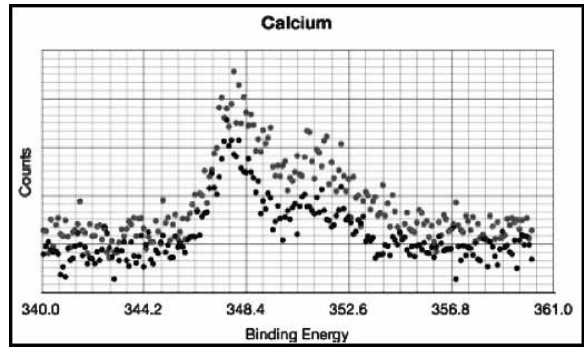


Figure 4: High-resolution XPS spectra of fiber sample in Ca 2p energy region.

considered. The XPS data also showed that the calcium ions were favored due to the selectivity of the fiber membrane.

Since the main difference in the cement chemical composition was the difference of calcium where gray cement had almost no calcium present (3%) and the white cement had an abundance (40%), the selectivity of the fiber for this calcium is what causes this acceleration in the hydration reactions in the white cement as shown in the calorimetry curves.

Future Work:

Additional research into investigating the effect of altering the surface morphology of the fiber could provide additional insight into the physical effects that fiber plays in cement hydration. Experiments that alter the fiber's surface through chemical manipulation to become more rough and therefore accelerate the nucleation properties of the fiber could provide additional insight into the cement hydration phase. Also, further insight into the role of the fiber's cell wall and the effects it has on the kinetics of the hydration reactions could be beneficial.

Acknowledgments:

I would like to thank my principal investigator, Dr. Kimberly E. Kurtis; my mentor, Passarin Jongvisuttisun; Dr. Nancy Healy, and Leslie O'Neill; the National Nanotechnology Infrastructure Network Research Experience for Undergraduate (NNIN REU) Program and the National Science Foundation for funding and making this research possible.

References:

- [1] Ashby, M. F., "Materials and the Environment", Butterworth-Heinemann Publisher, 2nd edition (April 11, 2012).
- [2] Weiss, J.W., Bentz, D.P., Schindler, A.K., and Lura, P., "Internal curing construction more robust concrete", Structure, January 2012:10-14.

Determination of Strength Degradation Mechanisms of Native Oxide on Silicon Nanostructures

Rafael Jesus Haro

Mechanical Engineering, University of Arizona

NNIN REU Site: Cornell NanoScale Science and Technology Facility, Cornell University, Ithaca, NY

NNIN REU Principal Investigator: Prof. Alan Zehnder, Mechanical and Aerospace Engineering, Cornell University

NNIN REU Mentor: Scott Grutzik, Field of Theoretical and Applied Mechanics, Cornell University

Contact: rharo06@email.arizona.edu, atz2@cornell.edu, sjg242@cornell.edu

Abstract:

Understanding what affects the strength of micro- and nanoelectromechanical systems (MEMS and NEMS) is essential to effectively designing load bearing MEMS / NEMS. Research by Alan, et al. [1], suggests that oxide growth on silicon nanostructures leads to a decrease in strength, therefore increasing the likelihood of failure [1]. To interpret how silicon strength is affected as native oxide grows on the beams, the beams were failure tested weekly for five weeks allowing continuous growth of oxide, after which strength had decreased to 81% of the original strength. After the oxide was removed, strength recovered to 96% of the original strength. Silicon beam failure tests were performed using an atomic force microscope (AFM), which recorded the deflection of the AFM cantilever and the displacement of the piezo. A reference cantilever was used to find the stiffness of the AFM cantilevers used for failure tests. The beam's failure stress was calculated from the beams' failure force using the finite element method.

Introduction:

Due to factors such as large surface to volume ratio and low defect density, nanoscale strength cannot be determined using macroscale experiments. Silicon is a brittle material that fails stochastically, which is why many beams must be tested to obtain accurate strength data. Research suggests that uneven oxide layer growth may form a rough surface on silicon beams, thus causing the AFM cantilever forces to concentrate at one

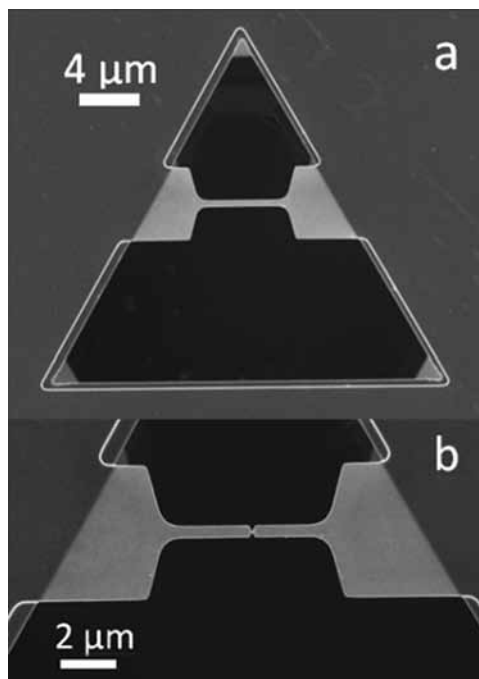


Figure 1: a) Top view scanning electron microscope image of beam and triangular trench. b) Beam with fracture at center.

of these stress points [1]. If roughness occurs, the beams' strength before and after oxide removal would be similar. Furthermore, if the strength is changed due to chemical interaction between oxide and silicon, the strength should increase after removal. To find how the mechanisms of native oxide growth correlate to silicon strength, nanoscale fracture specimens were fabricated and allowed to oxidize while tracking the reduction in strength. At the end, the oxide was removed and a final measurement of strength was made. The fabrication and strength analysis of the beams using an AFM was performed as described in Alan, et al. [2], and Namazu, et al. [3].

Methods:

Silicon $\langle 111 \rangle$ orientated wafers were used to fabricate the single crystal silicon beams. A photolithography step outlined the shape, and the beam thickness was etched using reactive ion etching (RIE). An oxide coat was grown on the wafer, and a second photolithography and RIE step defined the depth of the beam trenches. An anisotropic potassium hydroxide/ tetramethylammonium hydroxide etch released the beams by etching horizontally beneath them and terminating on their $\langle 111 \rangle$ orientation bottom surface. The beams were immersed into a buffer oxide etch removes the oxide to start performing the failure strength tests. The final beam sample is shown in Figure 1. To control the effect of humidity on rate of oxidation, the beams were stored at 100% relative humidity between strength tests.

The failure strength was measured using the deflection of the AFM cantilever and displacement of the piezo. The interaction between the piezo, AFM cantilever, and the beam were taken as springs in series (Figure 2); the piezo displacement equals the sum of the beam and AFM cantilever deflection [4]. A reference cantilever with a known stiffness was used to calculate the force applied on the beams. Finite element analysis was used to calculate the failure stress from the failure force (Figure 3). The failure stresses for each week fit a Weibull distribution as a group, which was used to measure average strength and plot as a function of time.

Results and Conclusions:

Testing in weeks two and three did not reflect the strength decrease as shown in Alan, et al. The beam strength, however, did increase surprisingly after oxide removal and resembled the strength prior to oxidation. Previous tests show that oxide reduces silicon beam's strength, which is not reflected from weeks two, three, and four (Figure 4). Our hypothesis about the cause of this discrepancy is the repetitive use of the same AFM cantilever. Since the same AFM cantilever was used for weeks one through four, debris from numerous beam fractures may have accumulated and caused this error in the data.

If only the data taken with new AFM cantilevers (weeks one, five, and six) are considered, then the results would fully reflect the degradation and restoration of beam strength. Techniques to protect silicon nanostructures from oxidizing and prevent strength reduction must be developed. Further analysis on the repetitive use of the AFM cantilever is needed to understand if this caused the error in the first few weeks.

Acknowledgments:

This project was performed using facilities at the Cornell NanoScale Facility (CNF), supported by NSF Grant ECS-0335765, with the collaboration of the National Nanotechnology Infrastructure Network Research Experience for Undergraduates (NNIN REU) Program — as well as the facilities at the Cornell Center for Materials Research (CCMR), supported by NSF grant DMR-1120296. Assistance provided by Scott Grutzik was greatly valued, and my sincere appreciation to Professor Alan Zehnder and future research.

References:

- [1] T. Alan, A. T. Zehnder, D. Sengupta, and M. A. Hines. Methyl monolayers improve the fracture strength and durability of silicon nanobeams. *App.Phys.Letters*, 89:231905, 2006.
- [2] T. Alan, M. A. Hines, and A. T. Zehnder. Effect of surface morphology on the fracture strength of silicon nanobeams. *Applied Physics Letters*, 89:091901, 2006.
- [3] T. Namazu, Y. Isono, and T. Tanaka. Evaluation of Size Effect on Mechanical Properties of Single Crystal Silicon by Nanoscale Bending Test Using AFM. *Journal of Microelectromechanical Systems*, 9(4):450-459, 2000.
- [4] S. Sundararajan and B. Bhushan. Development of AFM-Based Techniques to Measure Mechanical Properties of Nanoscale Structures. *Sensors and Actuators*, 101:338-351, 2002.

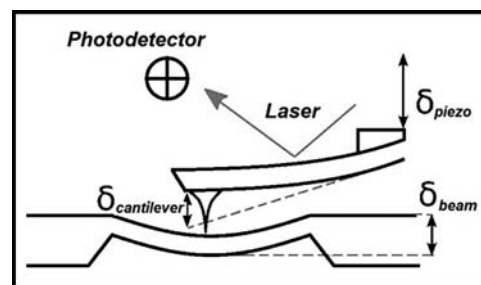


Figure 2: Side view schematic of the AFM cantilever and beam deflections.

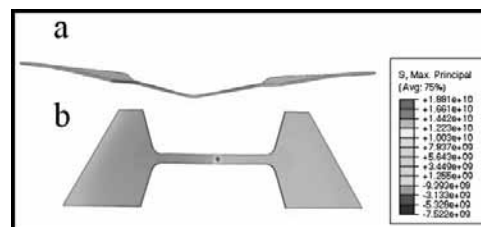


Figure 3: a) Side view finite element model of deflected beam. b) Top view of stress simulation. (See full-color version on inside cover.)

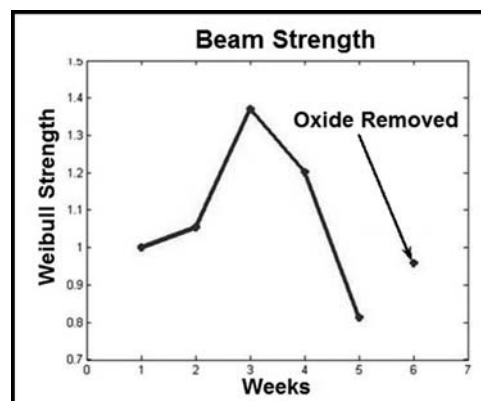


Figure 4: Normalized beam strength and weeks.

The Effects of Lanthanum-Doping on Strontium-Titanate Thin Films Grown on Si <001> Substrates

Christine Karako
Chemistry, University of Dallas

NNIN REU / NASCENT Site: Nanomanufacturing Systems for Mobile Computing
and Mobile Energy Technologies, The University of Texas at Austin, Austin, TX

NNIN REU / NASCENT Principal Investigator: Dr. John Ekerdt,

McKetta Department of Chemical Engineering, University of Texas at Austin

NNIN REU / NASCENT Mentor: Martin D. McDaniel, McKetta Department of Chemical Engineering, University of Texas at Austin

Contact: cmkarako@gmail.com, ekerdt@utexas.edu, mcdanimd@che.utexas.edu

Abstract:

Lanthanum-doped strontium titanate (La:STO) films were grown on silicon <001> substrates at a thickness range of 6-25 nm. Atomic layer deposition was used to grow the films after buffering the substrate with four unit cells of STO deposited via molecular beam epitaxy. La:STO films were successfully grown on silicon (Si) while maintaining a single-crystal structure and achieving good conductivity, in comparison to the insulating properties of undoped STO. The charge density of the La:STO film was calculated to be $2.18 \times 10^{21} \text{ cm}^{-3}$. Charge densities obtained for varying La concentrations ranged from 6.72×10^{20} to 3.86×10^{21} . Only 6% La-doping would be required to obtain the IBM specification of 1×10^{21} charges/cm³ for use in a transistor [1]. When tested electrically, a 15% La-doped thin film had a resistivity of about $1.6 \times 10^{-3} \Omega\text{-cm}$; however, this is still more resistive than bulk La:STO at the same La-doping concentration ($\sim 1 \times 10^{-4} \Omega\text{-cm}$) [2].

Introduction:

In the fast-paced, ever-developing silicon industry, research is being done to grow crystalline oxides on silicon. Strontium titanate (STO) is one of the few oxides that is chemically stable when deposited on silicon and would be useful in a variety of applications when integrated with other oxides such as the ferroelectric barium titanate [1]. Although research has been successful in such integration, there is a need to find better and more efficient deposition methods. The commonly used molecular beam epitaxy (MBE) process is costly and impractical for large-scale production. This research focuses on using a chemical deposition method, known as atomic layer deposition (ALD), to deposit La:STO thin films.

Experimental Procedure:

Silicon wafers were obtained and diced into $20 \times 20 \text{ mm}^2$ pieces. They were solvent cleaned and exposed to ozone radiation to remove carbon contamination, according to the procedure outlined by McDaniel et al. [3]. Using MBE growth methods, four unit cells of crystalline STO were grown on the Si interface to provide a crystalline template for the La:STO. The samples were transported *in vacuo* to the ALD chamber, where La:STO films were grown at thicknesses of 6-20 nm. Before removal from the vacuum system, these films were analyzed by x-ray photoelectron spectroscopy (XPS) to determine if the ALD was successful in depositing the correct stoichiometric amounts of the elements. After removal, the crystalline structure and film thicknesses were analyzed by x-ray diffraction (XRD) and x-ray reflectivity (XRR) methods. Contacts for electrical testing were made by gold sputter deposition and liquid gallium-indium metal. Electrical measurements were performed using a four-point probe station.

Results and Conclusions:

The XPS data revealed that the ALD growth method was successful in growing perovskite-structured La:STO. It also showed that increased lanthanum activation occurred after annealing at a substrate temperature greater than 600°C; this further corresponded to a decreased resistivity of the film when tested electrically. High doping concentrations ($\sim 30\%$) distorted the crystal, as was discovered in analysis of the XRD data. The rocking curve was an XRD analysis performed at a set angle to show the degree of crystallinity; it revealed that increasing film thickness as well as high doping concentrations

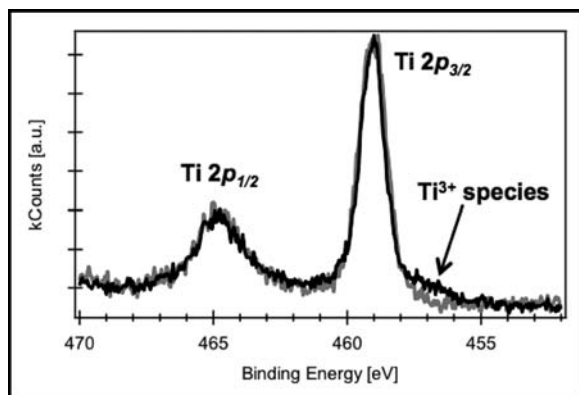


Figure 1: XPS Ti scans, before and after 600°C anneal, showing increased Ti³⁺ concentration from greater La activation.

(>30%) contributed to crystalline defects. Because the STO was compressively strained to match the lattice structure of Si, increasing film thickness would require greater energy to keep the crystals strained. Therefore, thicker films were unable to maintain this higher energy order and the STO relaxed back to its original lattice constant.

XRR analysis was used to determine the thicknesses of the films according to the relationship between the x-ray reflectivity and the film thickness given by Bragg's law: $\lambda = 2d\sin\theta$. It was estimated that the film thickness grown by ALD was the total thickness determined minus ~ 1.5 nm from the MBE template growth.

Future Work:

Future work would be required to study the electrical properties of thin film La:STO. Because a proposed transistor model by IBM would use a thin La:STO film of only 3 nm, it would be important to understand the impact of such a small scale on the mobility of the films [1].

Furthermore, it was hypothesized that uniform, perovskite crystallinity played an important role in the conductivity of these films since thicker, polycrystalline films had a higher measured resistance. Further research would need to be done to validate this supposition. In order to further the purpose of this research to eliminate the need for MBE growth methods, growth on a different substrate such as germanium may be necessary.

Acknowledgments:

This work is based upon work supported primarily by the National Science Foundation under Cooperative Agreements No. EEC-1160494 and No. DMR-1207342. Any opinions, findings and conclusions or recommendations expressed in this material are those of the author(s) and do not necessarily reflect the views of the National Science Foundation.

This research was performed through the support of the National Nanotechnology Infrastructure Network Research Experience for Undergraduates (NNIN REU) Program with funding provided by Nanomanufacturing Systems for Mobile Computing and Mobile Energy Technologies (NASCENT).

Much appreciation goes to Martin McDaniel and Dr. John Ekerdt for their guidance with this project.

References:

- [1] Dubourdieu, Catherine A., et al., "Ferroelectric Semiconductor Transistor Devices having gate modulated conductive layer," Patent publication number: 0292677, Nov. 22, 2012.
- [2] Marina, Olga A., et al., "Thermal, electrical, and electrocatalytic properties of lanthanum-doped strontium titanate," *Solid State Ionics*, Vol. 149, Issues 1-2, pp. 21-28, (2002).
- [3] McDaniel, Martin D., et al., "Epitaxial strontium titanate films grown by atomic layer deposition on SrTiO₃-buffered Si<001> substrates," *Journal of Vacuum Science and Technology A*, Vol. 31, Issue 1, 01A136-(1-9) (2012). <http://dx.doi.org/10.1116/1.4770291>

Developing Bioinspired Slippery Coating on Industrial Steels

Keiko Kato

Materials Science and Engineering, University of Illinois at Urbana-Champaign

NNIN REU Site: Penn State Nanofabrication Laboratory, The Pennsylvania State University, University Park, PA

NNIN REU Principal Investigator: Dr. Tak-Sing Wong, Mechanical and Nuclear Engineering, The Pennsylvania State University

NNIN REU Mentor: Jing Wang, Mechanical and Nuclear Engineering, The Pennsylvania State University

Contact: kato2@illinois.edu, tswong@enr.psu.edu, juw246@psu.edu

Introduction:

Creating an omniphobic coating on industrial metals that can repel various liquids and solids would have numerous industrial and medical applications, yet the development of such a coating has been very challenging. Conventional approaches utilize the lotus effect to create liquid-repellent coating, which capitalizes the idea of trapped air pockets within micro/nanotextures to create low-friction and low-adhesion surfaces. As these surfaces cannot sustain their property under extreme conditions such as high temperatures and pressures, another lesson was learned from nature to develop novel liquid/solid repellent mechanisms. Inspired by the insect trapping mechanism of a pitcher plant, a novel repelling surface was developed, which was termed as "Slippery Liquid-Infused Porous Surfaces" (SLIPS) [1]. SLIPS is consisted of chemically functionalized micro/nanostructured substrate and infused with a lubricating liquid. In this project, the protocol to apply SLIPS to industrial steels was explored.

Fabrication:

First micro/nanotextures were created on steel surface through chemical etching. Then the surface was chemically functionalized through oxygen plasma cleaning and silanization processes. At last, lubrication was applied to the functionalized micro/nanotextured surface.

Results and Discussion:

The resulting SLIPS-treated metal showed excellent liquid repellent properties against a broad range of fluids, including both water and oils, as well as complex fluids, such as blood. Figure 1 shows the change in surface repellency to octane after the SLIPS treatment.

First, the etched surface was investigated through field emission scanning electron microscope (FESEM) to ensure the existence of micro/nanoscale textures, as shown in Figure 2. Second, the repellent property of the surface was studied by measuring sliding angles with a goniometer. A droplet of 10 μL and a CSS camera were used to capture pictures of droplet's movement at each second. Those pictures were used to determine the sliding angle. Significant decrease of sliding angle was observed for various liquids in Figure 3 as a result of SLIPS treatment. The sliding angle of 90° was decreased to below 3° after the SLIPS coating.

Since the micro/nanoscale textures are mono-lithographically integrated with the metal surfaces, our SLIPS coatings demonstrate excellent robustness against multiple physical damages. The physical damage was demonstrated by applying adhesive tape on the etched metal surface with 500 gram of weight to add an extra force to the tape. The tape was removed and the sliding angle was measured to observe the change in surface repellent properties after the physical damages. Additionally, the application of SLIPS on metals of any geometries was succeeded including a flat surface, sphere, and pipe tube as shown in Figure 4.

The ability to apply omniphobic slippery coatings on industrial steels would enable a broad range of industrial and medical applications including multi-functional coatings for anti-icing, anti-corrosion, anti-scaling, friction reduction, and anti-fouling purposes [2, 3].

Future Work:

SLIPS will be applied to different metals to explore various industrial and medical applications of SLIPS.

Acknowledgements:

I would like to show my appreciation to my principal investigator, Dr. Tak-Sing Wong, and my mentor Jing Wang for the assistance to guide me through the research. I would also like to thank my colleagues, Alexandre P. Blois, and Nanofab and Material Characterization Laboratory staff for their support to prepare the data. I would also like to thank the National Nanotechnology Infrastructure Network Research Experience for Undergraduates (NNIN REU) Program and National Science Foundation for the financial support and the opportunity.

References:

- [1] Wong, T.-S., et al. "Bioinspired self-repairing slippery surfaces with pressure-stable omniphobicity", *Nature* 477, 443-447 (2011).
- [2] Kim, P., et al. "Liquid-Infused Nanostructured Surfaces with Extreme Anti-Ice and Anti-Frost Performance", *ACS Nano* 6, 6569-6577 (2012).
- [3] Epstein, A. K., et al. "Liquid-infused structured surfaces with exceptional anti-biofouling performance", *PNAS*, 109, 13182-13187 (2012).

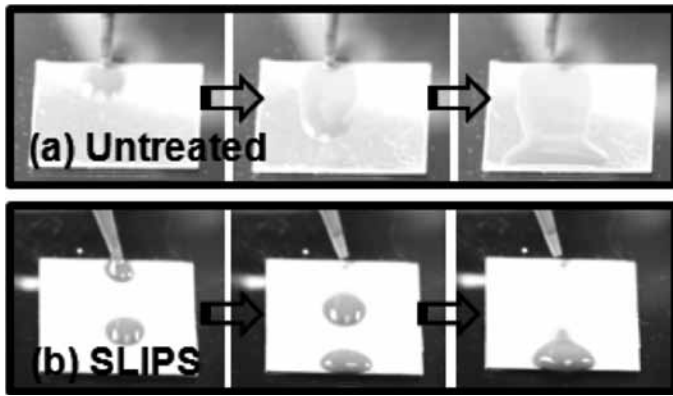


Figure 1: The surface repellency of stainless steel 304 to octane; (a) Untreated steel, (b) SLIPS-coated steel. (See full-color version on inside cover.)

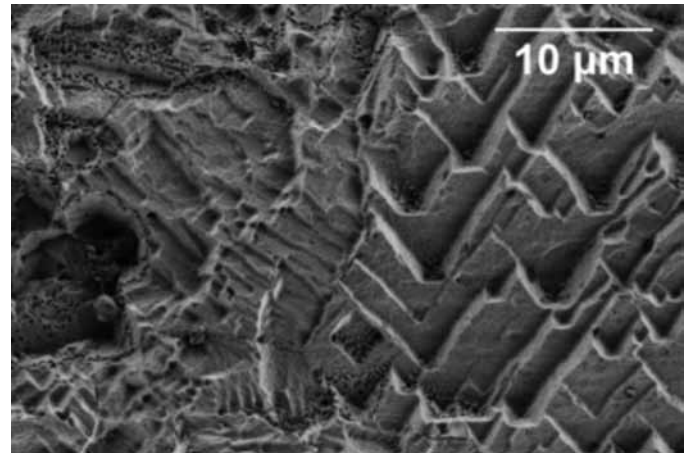


Figure 2: FESEM image of etched stainless steel 304 surface.

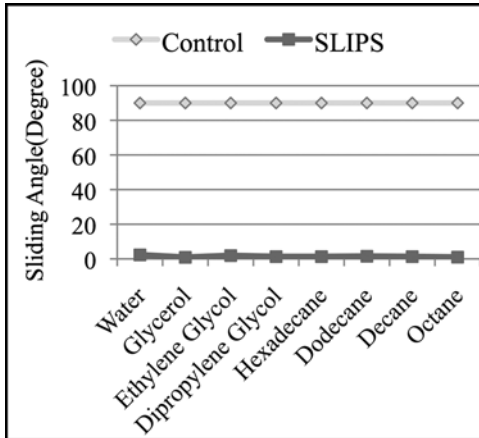


Figure 3: Sliding angles of various fluid droplets on untreated and SLIPS-coated stainless steel 304. The sliding angle before SLIPS treatment resulted in 90°, which decreased to less than 3° after SLIPS treatment against broad range of liquids.

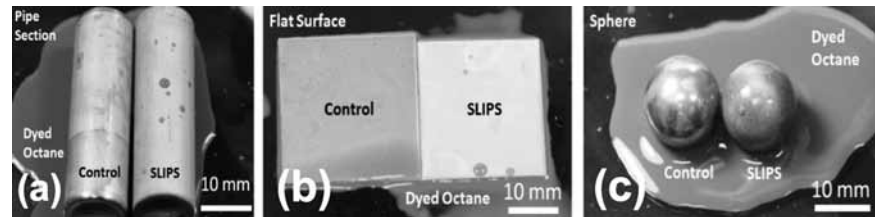


Figure 4: SLIPS was applied on different geometries of stainless steel 304 and the surface repelled octane (dyed in yellow-orange color). In each picture, the left sample is untreated steel and the right sample was SLIPS-treated steel. (a) pipe tube, (b) flat surface, and (c) sphere. (See full-color version on inside cover.)

The Effect of Surface Roughness on Chemical Vapor Deposition of Hexagonal Boron Nitride

Daniel David Kuddes
Physics, University of Texas at Dallas

NNIN REU / NASCENT Site: Nanomanufacturing Systems for Mobile Computing
and Mobile Energy Technologies, The University of Texas at Austin, Austin, TX
NNIN REU / NASCENT Principal Investigator: Prof. Rodney Ruoff, The Department of Mechanical Engineering
and the Materials Science and Engineering Program, The University of Texas at Austin
NNIN REU / NASCENT Mentor: Dr. Ariel Ismach, Department of Mechanical Engineering, The University of Texas at Austin
Contact: ddk091020@utdallas.edu, r.ruoff@mail.utexas.edu, aismach@austin.utexas.edu

Abstract:

Hexagonal boron nitride (h-BN) is a favorable substrate for graphene and other two-dimensional molecules due to its lack of inter-planar covalent bonds, smooth topology, insulating properties, and a near epitaxial lattice to graphene. Additionally because of its wide band gap, h-BN has potential applications in electronics as an insulator, in transistors, and in electroluminescent devices [1]. Our strategic goal for h-BN was to find a means to synthesize a large scale homogenous h-BN mono-layer with few gaps, breaks, or lattice defects. The focus of our project was to better understand the role of surface roughness when using chemical vapor deposition to grow h-BN on a catalytic metal and apply that knowledge to create high quality h-BN films. Our experiments showed flatter Ni surfaces lead to considerably more homogenous h-BN with fewer ad-layers and more uniform coverage than h-BN grown on rougher Ni surfaces.

Purpose and Introduction:

The purpose of our experiment was to determine the effect, if any, of catalytic metal's surface roughness on low pressure vapor chemical deposition (LPCVD) of hexagonal boron

nitride (h-BN) [2]. H-BN was grown on two samples using the same growth conditions in the same system. Preliminary results show the smoothed sample exhibits a more continuous mono-layer of h-BN containing fewer ad-layers (h-BN layers on top of other h-BN layers).

The experiment took place in two steps. The first step was to determine if a smooth Ni surface would remain smooth despite being heated to 1050°C. After determining that the Ni film remained smooth despite the high heat, the second experiment compared the deposition of h-BN on smooth and rough Ni foils.

Experimental Procedure:

A. Polishing. Mechanical polishing was used to smooth the surface of a 25 μm thick 1-inch by 1-inch Ni film. To polish,

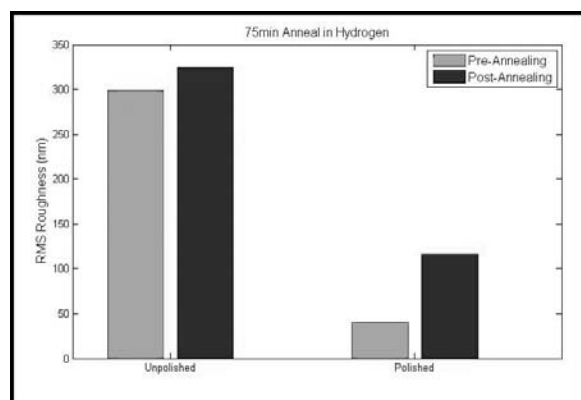


Figure 1: The roughness of the polished Ni sample more than doubled after annealing, but it remained at least three times smoother than the as received sample.

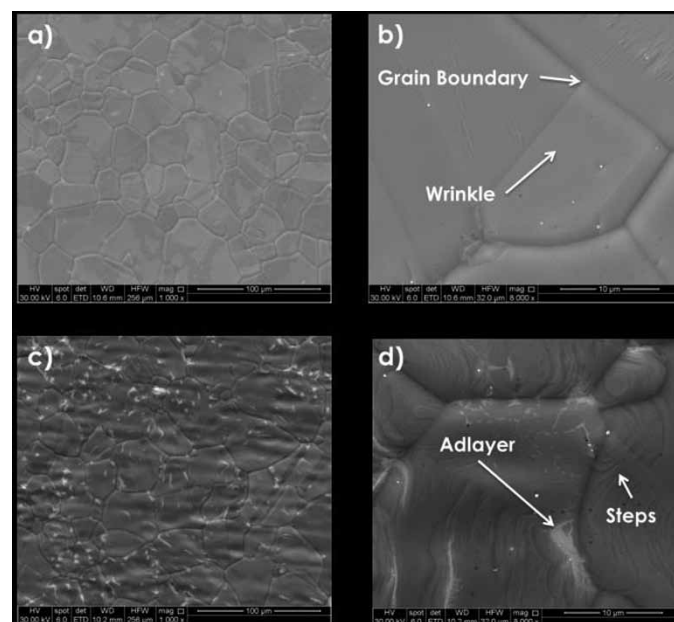


Figure 2: SEM images of h-BN on Ni Taken at 1,000x and 8,000x magnification. Images a) and b) show polished Ni. Images c) and d) show unpolished Ni.

a hand dremel and 1.0 μm grit alumina-based polish were used. The film was polished five minutes per inch, resulting in a surface roughness of 29 nm RMS from an as-received roughness of 300 nm.

B. Low Pressure Chemical Vapor Deposition. Our method of using LPCVD to deposit h-BN on Ni films involved heating the samples to 1050°C — the melting point of Ni is 1455°C. By bringing the temperature of the metal close to the melting point, the metal surface becomes semi-molten. Therefore, it was unclear if any smoothing done to the surface before annealing would have an effect on the surface after annealing.

After determining that the polished Ni film remained substantially smoother than the as-received Ni film, the next experiment involved the growth of h-BN on a polished Ni surface. LPCVD was used to grow h-BN. Our gas flow furnace, where the growth occurred, had a base pressure of 5 mTorr. An ammonia borane vial was heated such that the resulting gas, along with methane, was flowed over the samples — resulting in h-BN being deposited on the Ni films.

Results and Conclusions:

It was shown, using an optical profilometer, that the smoothed Ni film remained substantially smoother than the rough nickel film after annealing (see Figure 1).

SEM images were used to compare the smooth and rough samples (see Figure 2). The h-BN on the polished sample showed a number of favorable attributes. The polished film seemed to have more uniform coverage of h-BN. There were fewer steps in the polished film — indicating a smoother surface and fewer ad-layers in the polished film.

While not verified, polishing a Ni surface prior to h-BN growth seemed to lead to fewer ad-layers and a larger continuous area of h-BN. Polishing not only smoothed the surface, but also left alumina particles, eliminated as received features, and cleaned the surface of contaminants. While it seemed that more favorable films resulted from polishing, it is not entirely clear that this was a result of a change in surface smoothness and not some other effect of the polishing.

Future Work:

Polishing leaves residual contaminants on the film — identified as Al_2O_3 by energy dispersive x-ray spectroscopy. Eliminating this extra variable could lead to more decisive evidence that a change in surface smoothness is responsible for the changes in h-BN growth and not some other product of the smoothing procedure. Using a smoothing technique that doesn't use a polishing compound, such as pressure induced surface deformation that does not leave contaminants on the Ni surface, would be illuminating [3].

Shifting grain boundaries and other effects resulted in changes in smoothness post-annealing. The effects of these shifts might be reduced by annealing at or above the growth temperature and then applying a smoothing procedure followed by growth of h-BN. Furthermore, the use of glassy metal may allow for a smoother surface.

Acknowledgments:

I wish to thank Prof. Rodney Ruoff, Dr. Ariel Ismach, Harry Chou, Ruderesh Ghosh, Marylene Pallard, the NASCENT Research Undergraduate Experience coordinators, the National Nanotechnology Infrastructure Network Research Experience for Undergraduates (NNIN REU) Program, and the National Science Foundation for their help in making this work possible.

References:

- [1] Colombo, L., R.M. Wallace, and R.S. Ruoff. "Graphene Growth and Device Integration." *Proceedings of the IEEE*, 101 (7), 1536-1556 (2013).
- [2] Pakdel, A., C. Zhi, Y. Bando, and D. Golberg, "Low-dimensional boron nitride nanomaterials." *Materials Today*, V15, Issue 6, June 2012, Pages 256-265, ISSN 1369-7021, [http://dx.doi.org/10.1016/S1369-7021\(12\)70116-5](http://dx.doi.org/10.1016/S1369-7021(12)70116-5).
- [3] Logeeswaran, V.J., M.-L. Chan, Y. Bayam, M. Saif Islam, D.A. Horsley, X. Li, W. Wu, S.Y. Wang, and R.S. Williams, "Ultra-smooth metal surfaces generated by pressure-induced surface deformation of thin metal films." *Applied Physics A*. 2007.

Thermodynamic Control of Lead Content in the Piezoelectric Thin Film

Fumiya Kurokawa

Mechanical Engineering, Kobe University, Hyogo Prefecture, Japan

NNIN iREG Site: Penn State Nanofabrication Laboratory, The Pennsylvania State University, University Park, PA

NNIN iREG Principal Investigator: Susan Troler-McKinstry, Materials Science and Engineering, The Pennsylvania State University

NNIN iREG Mentor: Daniel Marincel, Materials Science and Engineering, The Pennsylvania State University

Contact: fumiya.kurokawa.kobe.ma2@gmail.com, stmckinstry@psu.edu

Abstract:

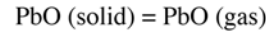
Recently, piezoelectric thin films have become attractive as a component for low voltage MEMS applications. Lead-based perovskite materials are used because of their excellent ferroelectric and piezoelectric properties. However, the volatility of lead creates difficulties in the deposition process, because high temperature annealing process is required for perovskite phase development. Conventionally, excess lead is added to thin films in order to control lead content during high temperature processing. However, it is still difficult to precisely control the stoichiometry of lead-based piezoelectric thin film, since the proper amount of excess lead depends on deposition process or conditions.

In this study, lead composition control is being pursued in the piezoelectric thin film via thermodynamic, rather than kinetic control. Post annealing is being conducted for lead deficient piezoelectric thin films in a PbO furnace. Theoretical calculation suggests that it should be possible to control lead content via thermodynamics. Experimentally, we found PbO thin films can be deposited using this system. These results suggest that we could also deposit PbO thin film on Pb-deficient PZT thin film and crystallize stoichiometric PZT thin film.

Introduction:

Recently, piezoelectric thin film has become attractive for low voltage microelectromechanical system (MEMS) applications. Among various piezoelectric materials, lead-based materials, especially lead zirconate titanate [Pb(Zr,Ti)O₃, PZT], are used because of their excellent piezoelectric properties [1]. However, the volatility of lead creates difficulties in the deposition process, because high temperature annealing is required for perovskite phase development. Conventionally, excess lead is added to thin films in order to control lead content during high temperature processing. However, it is still difficult to precisely control the stoichiometry of the piezoelectric thin film, since the proper amount of excess lead depends on deposition process or conditions.

We focused on thermodynamic method to control the lead content in the piezoelectric thin film in a PbO metalorganic chemical vapor deposition system using tetra-ethyl lead [TEL] as a lead source. The vapor pressure of PbO was calculated from the thermodynamic reaction:



$$\log P_{\text{PbO}} = -\frac{15030}{T} + 9.51 \quad [\text{atm}]$$



$$\log P_{\text{PbO}} = -\frac{13660}{T} + 7.15 \quad [\text{atm}]$$

where P and T are the pressure and temperature [2]. These equations suggest that lead content can be controlled by PbO pressure and temperature.

In this study, we suggest a new method to control lead content in the piezoelectric thin film via thermodynamic method. We conducted post-annealing process in the furnace with controlled PbO pressure and annealing temperature.

Experimental Procedure:

Figure 1 shows an optical image and schematic diagram of PbO furnace to deposit PbO thin film and control lead content in a PZT thin film. Tetra-ethyl lead [TEL] is used as a source of PbO. It was supplied by Gelest packaged in bubbler. In this system, we have three important parameters; TEL flow rate, bubbler temperature, and chamber temperature.

At first, we conducted theoretical calculation to estimate the conditions to control lead content. Theoretical values of PbO pressure in the chamber are calculated from the following equation:

$$P_{\text{TEL,Chamber}} = \frac{10^{9.361 - \frac{2910}{T_{\text{Bubbler}}}} \times f_{\text{TEL}} \times T_{\text{Chamber}}}{(f_{\text{N}} + f_{\text{O}} + f_{\text{TEL}}) \times T_{\text{Bubbler}}}$$

where f_{N} , f_{O} , f_{TEL} , T_{Bubbler} and T_{Chamber} are the nitrogen flow rate, oxygen flow rate, TEL flow rate, bubbler temperature and annealing temperature, respectively. Then f_{N} and f_{O} were fixed at maximum flow rates of 3448 sccm and 1000 sccm, respectively. Figure 2 shows the PbO pressure in the chamber as a function of TEL flow rate at a bubbler temperature of 45°C and an annealing temperature of 750°C. The (▲) and (●) lines indicate boundary pressure for the chemical reaction from PbO gas to PbO solid and from PbZrO₃ to PbO gas and ZrO₂,

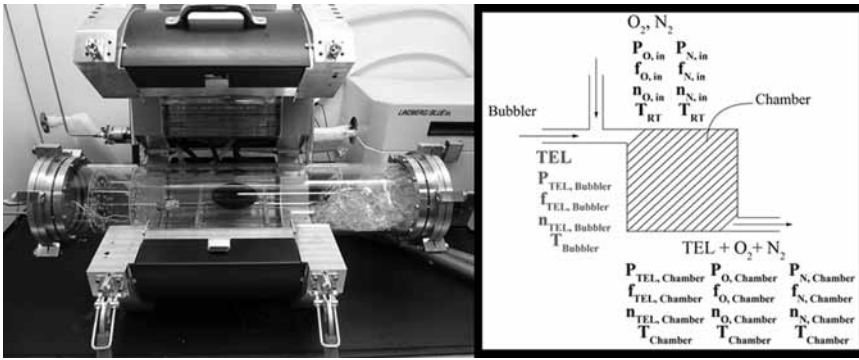


Figure 1: PbO furnace; (a) Optical image, (b) Schematic diagram.

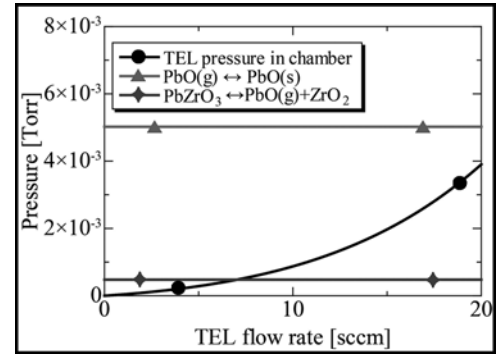


Figure 2: PbO pressure in the chamber as a function of TEL flow rate.

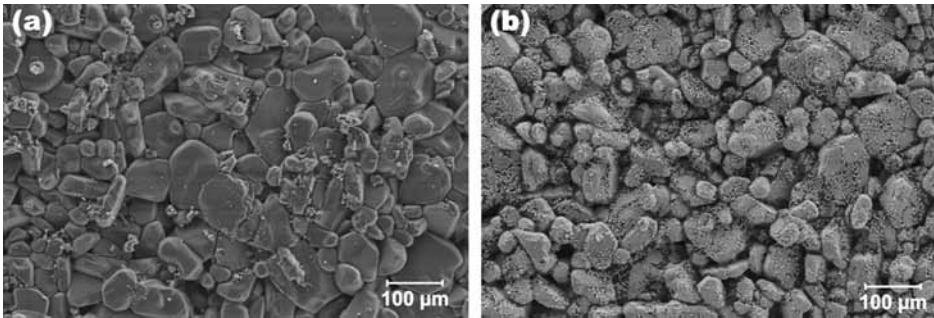


Figure 3: Surface SEM images of Al_2O_3 substrate (a) before (b) after PbO thin film deposition.

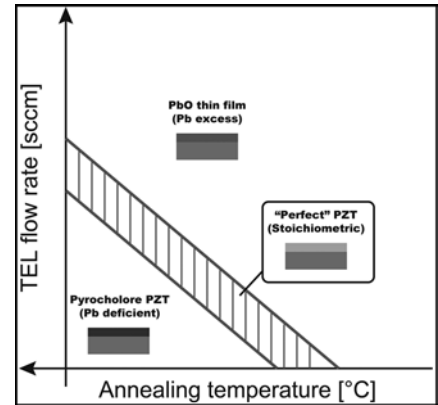


Figure 4: Phase diagram of PZT thin film as a function of annealing temp and TEL flow rate.

respectively. This figure suggests we could compensate lead content with TEL flow rate from 8 to 20 sccm under a bubbler temperature of 45°C and an annealing temperature of 750°C.

Results and Conclusions:

As an initial experiment, we tried to deposit PbO thin film on an aluminum oxide (Al_2O_3) substrate, which doesn't react with lead chemically, to confirm whether this system is useful or not. We conducted annealing at a TEL flow rate 20 sccm, a bubbler temperature of 45°C, and an annealing temperature 500°C. Figure 3 shows surface SEM images before and after PbO deposition. We found PbO thin film can be deposited on Al_2O_3 substrate using this system. Additional experiments need to be conducted to evaluate the growth rate.

We suggest a new approach to control lead content in piezoelectric thin films. Theoretical calculation suggests that we could control lead content via thermodynamic method. Furthermore, we found PbO thin film can be deposited using this system. These results suggest that we could also deposit PbO thin film on Pb-deficient PZT thin film and crystallize stoichiometric PZT thin film.

Future Work:

Figure 4 shows phase diagram of PZT thin film as a function of TEL flow rate and annealing temperature. This diagram is the final objective of this research. To find the boundary of this phase diagram, we should conduct post-annealing for Pb-deficient PZT thin film.

Acknowledgements:

This work was made possible under the NNIN iREG Program, together with Nanotechnology Platform, Japan. I also appreciate my principal investigator Dr. Susan Trolier-MacKinstry, mentor Mr. Dan Marincel, and all group members.

References:

- [1] P. Murali, R. G. Polcawich, and S. Trolier-McKinstry, "Piezoelectric Thin Films for Sensors, Actuators, and Energy Harvesting", *MRS. Bull.*, vol. 34, no. 9, pp. 658-664, 2009.
- [2] K. H. Hardtl, and H. Rau, "PbO vapour pressure in the $Pb(Ti_{1-x}Zr_x)O_3$ system", *Solid. State, Commun.*, vol. 7, pp. 41-45, 1969.

Improvement of Lithium Ion Batteries with Selected Dopants

Deanna Lanigan

Materials Science and Engineering, University of Wisconsin-Madison

NNIN REU Site: Nano Research Facility, Washington University in St. Louis (WUSTL), St. Louis, MO

NNIN REU Principal Investigator: Professor Richard Axelbaum, Energy, Environmental, and Chemical Engr., WUSTL

NNIN REU Mentor: Miklos Lengyel, Energy, Environmental, and Chemical Engineering, Washington University in St. Louis

Contact: dlanigan@wisc.edu, axelbaum@wustl.edu, mlengyel@wustl.edu

Introduction:

For electric vehicles to be a feasible option for the general public, batteries need to deliver higher capacities, higher rate capabilities, and longer cycle life at a fraction of the current cost. Nanostructured lithium-ion battery cathode material formed through spray pyrolysis is promising because of its beneficial morphology along with the scalability of the process for mass production. We focused on the layered $\text{Li}_{1.2}\text{Mn}_{0.53}\text{Ni}_{0.13}\text{Co}_{0.13}\text{O}_2$ composition due to its excellent capacity of over 250 mAhg^{-1} . However, this specific structure suffers from voltage fade upon cycling. The purpose of our investigation was to determine the effects of dopant substitution on the voltage fade characteristics of the batteries. Through this study, we hoped to achieve a better understanding of the voltage fade phenomena to aid in the commercial implementation of these materials in electric vehicles.

Experimental Procedure:

The precursor solutions were made of nitrate solutions dissolved in deionized water for use in spray pyrolysis. The precursor solution was placed in a nebulizer, which created a fine mist. The aqueous droplets were carried into a preheater using air as the carrier gas. There, they underwent rapid drying and then were conveyed into a hot furnace reactor heated to 575°C, where they decomposed, forming oxide particles. The particles were collected downstream of the reactor on porous polycarbonate filters. After each hour, the material was collected and weighed. The as-synthesized particles were then annealed at 900°C for two hours in a box furnace. The powders were converted into a thin film using the doctor blade method. The binder solution contained 10% carbon black, 10% PVDF (poly-vinylidene-fluoride) and 1-methyl-2-pyrrolidinone. The

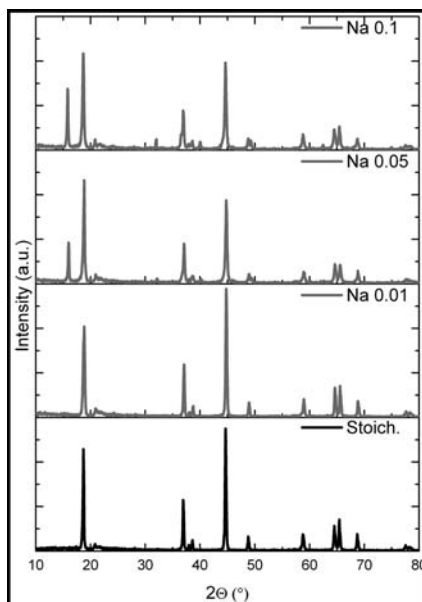


Figure 1: XRD.

cathodes were then tested in 2032 type coin cells using 1M LiPF_6 in ethylene-carbonate:diethyl-carbonate:dimethyl-carbonate (EC:DEC:DMC, 1:1:1).

Battery tests included rate capability tests, cycling tests, and voltage fade tests. All electrochemical testing was performed at room temperature. Rate capability tests demonstrated how well the structure responded to different charge and discharge rates. The rates chosen were C/10, C5, C2, C1, and then C/10 again (where 1C = 200 mA/g). Cycle tests demonstrated the cell's ability to maintain capacity over extended cycling. The entire test spanned over 100 cycles. The cycle test was used for seven different doped batteries, along with an undoped battery cell for comparison. The rates used for this test were C/10 and C/3. The activation cycle was between 2.0-4.8V at

C/10 and subsequent cycles were between 2.0-4.6V for cycle and rate tests. Voltage fade tests were performed for 30 cycles, but have not yet been completed. After an initial activation cycle between 2.0-4.8V at C/20, the remaining cycles were performed at C/10.

The powders were characterized using both powder x-ray diffraction (XRD) and scanning electron microscopy (SEM). XRD, as seen in Figure 1, was used to verify the crystal structure of the powders. At low dopant levels, the crystal structure should not have strayed far from the undoped material. However, when the dopant level was too high for the structure to accommodate the dopants, it formed a separate phase, indicated by additional peaks in the diffraction spectrum. Figure 1 shows four different particle compositions, where part of the lithium was substituted for different Na levels.

It is clear that when the 0.05 Li atoms are replaced by Na atoms additional peaks start to occur in the XRD spectra, which become more pronounced as the concentration increases.

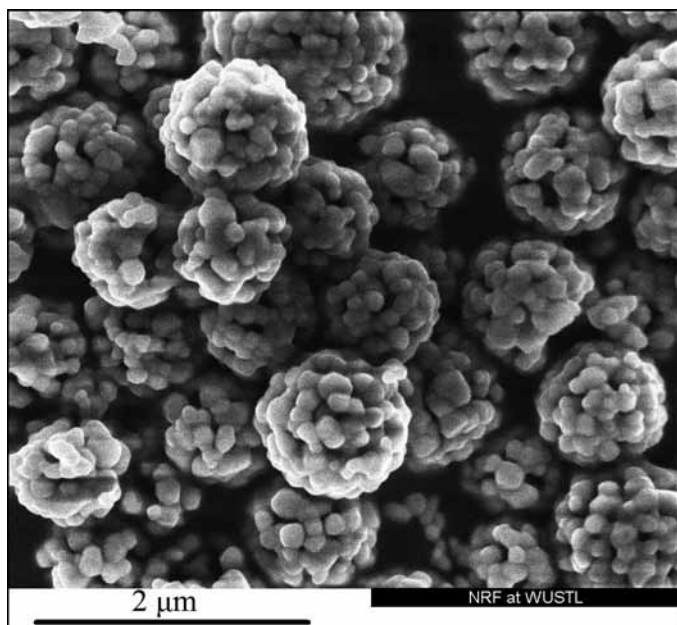


Figure 2: SEM.

Figure 2 shows an SEM image of chromium-doped particles. The particles are primarily spherical in shapes and have 200-400 nm size primary grains, while forming loosely aggregated secondary particles, which range between 0.5-5.0 μm .

Results:

Figure 3 shows the results of the rate test of selected materials compared to the undoped composition. Although there were not significant differences, the battery with the strontium-doped cathode material seemed to outperform the undoped battery in the final C/10 segment by maintaining a high capacity.

Cycle test results are displayed in Figure 4. From these initial results, no significant difference could be observed in the capacity fade behavior of the various dopants. However, the battery with the aluminum-doped cathode material maintained a higher capacity than the undoped sample after 100 cycles. As it can be seen from Figure 4, some of the dopants, most notably magnesium, may have reduced the capacity of the cell. This could be the consequence of exchanging transitional metal ions, which have multiple oxidation states by metal ions, which only have a single oxidation state. This way the host structure may become electrochemically inactive. However these results may indicate that the capacity and stability can be tuned to optimal performance for specific battery applications.

The voltage fade studies that are underway will help determine the dependence of this relationship to dopant levels.

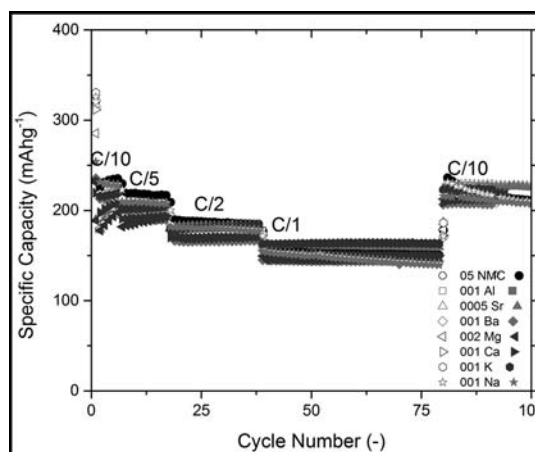


Figure 3: Rate test.

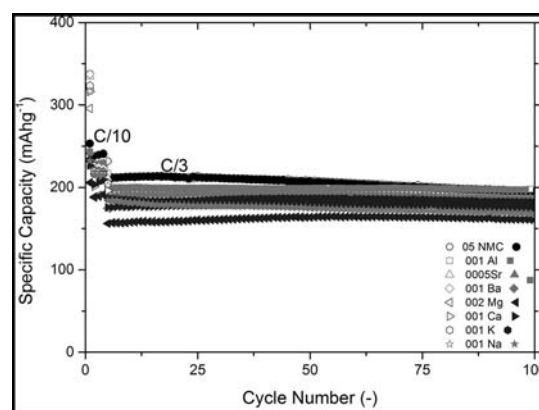


Figure 4: Cycle test.

Future Work:

Future work will focus on evaluating results from the voltage fade study. These results will be used in conjunction with impedance spectroscopy to determine more detailed data about diffusion mechanisms within the material and optimize the composition to reduce and hopefully eliminate the voltage fade of these materials. Studies focusing on two or more dopants will be performed based upon the results of the current study.

Acknowledgements:

I would like to thank my Mentor, Miklós Lengyel, and my Principal Investigator, Dr. Richard Axelbaum. I would also like to thank Dee Stewart, Nathan Reed, and all of the Nano Research Facility staff at Washington University in St. Louis. Finally, I would like to thank the NNIN REU Program and the National Science Foundation for making this research opportunity possible.

Preparation of Transparent Conducting Copper Aluminum Oxide Films

Jeremy Leshin

Chemical Engineering, University of Florida

NNIN REU Site: Nano Research Facility, Washington University in St. Louis, St. Louis, MO

NNIN REU Principal Investigator: Dr. Parag Banerjee, Mechanical Engr. and Materials Science, Washington University in St. Louis

NNIN REU Mentor: Fei Wu, Department of Mechanical Engineering and Materials Science, Washington University in St. Louis

Contact: jleshin@ufl.edu, parag.banerjee@wustl.edu, wufei5433@gmail.com

Introduction:

Most optically transparent materials are electrical insulators. Transparent conducting oxides (TCOs) are exceptions and are used in optoelectronics such as photovoltaics and flat panel displays which need transparent electrodes. Currently, all mass produced TCOs are n-type, such as Sn-doped In_2O_3 and Al-doped ZnO. However, p-type TCOs are also necessary for electronic devices that require the entire p-n junction to be transparent, which would allow for devices that both generate electricity and transmit visible light (e.g. functional windows). P-type TCOs have been under study in recent years after the discovery of p-type conducting CuAlO_2 thin films by Kawazoe et al. with light transmittance of up to 70% [1].

However, most known ways of producing CuAlO_2 involve high temperature sintering of binary oxides for extended periods of time. In this project, CuAlO_2 synthesis was attempted using a DC-sputtering process employing elemental copper and aluminum targets. In this study, films were attempted by depositing Cu/Al bilayer films as well as co-sputtered films formed in the presence of oxygen. Only the co-sputtering process shows promise as a method of CuAlO_2 preparation, as the bilayer structure proved an ineffective route for production of such films.

Experimental Procedure:

Films were deposited using direct current (DC)-sputtering physical vapor deposition with a Kurt J. Lesker PVD 75 system, creating both bilayer and co-sputtered structures. To deposit the bilayer structure, a 50 nm layer of silicon dioxide (SiO_2) was grown on 2-inch silicon wafers to act as a diffusion barrier between the metallic film and substrate. Aluminum (Al) was deposited for 250 seconds at 300W for a 39 nm layer. Copper (Cu) was deposited for 43 seconds at 300W to form a 26 nm layer. These thicknesses were chosen to have a one-to-one stoichiometric equivalence of Cu and Al atoms in the bilayer structure. Samples were then annealed in an oxidation furnace for four to 12 hours at temperatures ranging from 400°C-900°C.

Reactive co-sputtering was employed to produce a single layer structure on glass substrate. Cu and Al were deposited simultaneously for 1000 seconds with Cu at 30W and Al at 60W. Deposition was performed in an argon/oxygen (Ar/O₂) atmosphere with oxygen content ranging from 2-10%. During the deposition process, the glass was heated to temperatures ranging from 100°C-300°C. Bilayer samples were characterized using x-ray diffraction crystallography (XRD) to determine composition. Co-sputtered samples were characterized using energy dispersive x-ray spectroscopy (EDX) to determine atomic composition, as well as UV-Vis spectrophotometry to characterize optical properties of the films at wavelengths between 300 nm and 1100 nm.

Results:

Films produced in the bilayer structure were shown by XRD to be composed primarily of Cu and Al oxides. CuAlO_2 reached a maximum purity of approximately 10% at 900°C annealed for 8h. Lower temperatures formed the binary oxides and CuAl alloy. Shorter annealing times also formed a large amount of unoxidized metal (Figure 1). At longer annealing durations, the SiO_2 barrier failed and metal diffused into the wafer forming silicides. Reactive co-sputtered films could not be characterized by XRD (Figure 2); this is an indicator that the films formed through this process were amorphous in nature [3].

UV-Vis showed the transparency of the co-sputtered films to decrease on average with increasing substrate temperature (Figure 3), and increase with the oxygen content present during deposition. Films formed at 100°C showed the highest level of transmittance, while those formed at 300°C and 2% O₂ showed the lowest. The higher oxygen content likely allowed for increased oxidation of the metals in the film to form the transparent CuAlO_2 phase. All films except those formed at 300°C and 10% O₂ displayed a peak at about 550 nm, caused by the Cu content in the films.

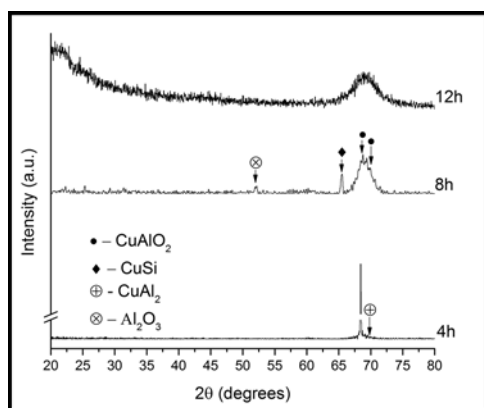


Figure 1: XRD of bilayer films at 900°C.

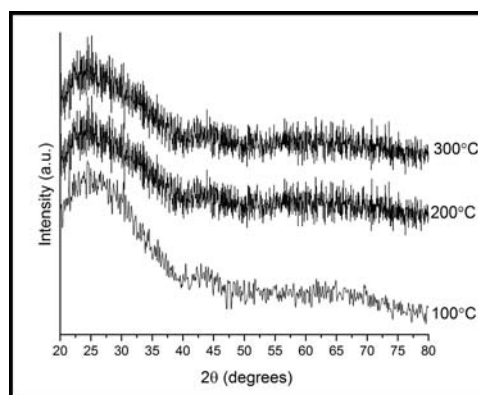


Figure 2: XRD of co-sputtered films in 5% O₂.

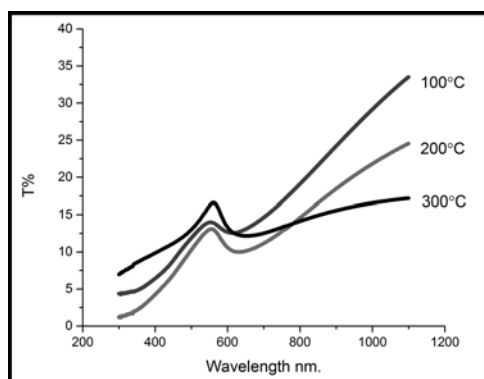


Figure 3: UV-Vis transmittance of Co-sputtered films in 5% O₂.

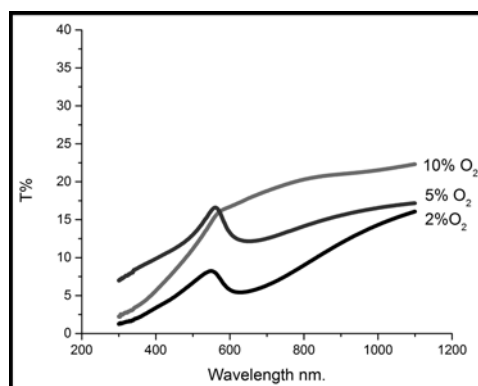


Figure 4: UV-Vis transmittance of Co-sputtered films at 300°C.

EDX was performed on films prepared via co-sputtering at 100-300°C and 5% O₂. Films formed at 100°C and 200°C were shown to have nearly the same relative amounts of Cu and Al. At 300°C, Al content of the film decreased significantly when compared to the Cu content. However, none of the films had the 1:1 Cu:Al ratio necessary for the formation of pure phase CuAlO₂.

Conclusions and Future Work:

Ultimately, use of the Cu-Al bilayer structure was proven to be an unviable method of CuAlO₂ thin film preparation. Reactive co-sputtering formed films with up to 30% transparency, short of pure phase CuAlO₂, but proper characterization of the films would require a crystalline structure. Literature and our preliminary results suggest that CuAlO₂ can be formed using this process. Better characterization of the deposition process at various oxygen levels and substrate temperatures will be needed to maintain proper stoichiometric ratios of Cu and Al in order to prepare the CuAlO₂ phase.

Possible inclusion of post-deposition annealing will also be tested as a method of ensuring crystalline structure of the films.

Acknowledgements:

I would like to thank Dr. Parag Banerjee, Fei Wu, and the Laboratory for Emerging and Applied Nanomaterials for all of their help and guidance. I would also like to thank the Nano Research Facility, National Nanotechnology Infrastructure Network Research Experience for Undergraduates Program, and the National Science Foundation for this opportunity.

References:

- [1] H. Kawazoe, M. Yasukawa, H. Hyodo, M. Kurita, H. Yanagi, and H. Hosono, *Nature* 389, 939-942 (30 October 1997).
- [2] Nandy, S., Maiti, U.N., Ghosh, C.K., and Chattopadhyay, K.K., "Optical and electrical properties of amorphous CuAlO₂ thin film deposited by RF magnetron sputtering," *IWPSD 2007*, pp.443,445, 16-20 Dec. 2007.

Challenges for Diamond Integrated Circuits

Clay T. Long

Physics, The Pennsylvania State University

NNIN iREU Site: National Institute for Materials Science (NIMS), Tsukuba, Ibaraki, Japan

NNIN iREU Principal Investigator: Dr. Yasuo Koide, National Institute for Materials Science

NNIN iREU Mentors: Dr. Eiichiro Watanabe, Dr. Masataka Imura, and Dr. Tsuya Daijyu, National Institute for Materials Science

Contact: clayl@andrew.cmu.edu, koide.yasuo@nims.go.jp, watanabe.eiichiro@nims.go.jp, daijyu.tsuya@nims.go.jp

Abstract:

Diamond is a nontraditional material for use in the transistor industry. It poses many challenges for consistent fabrication over semiconductors such as silicon or gallium arsenide. However, diamond has several desired material characteristics for integrated circuits (ICs). We therefore explored the properties of several simple devices on diamond — namely, transistors, inverters, and ring oscillators.

Introduction:

Integrated circuits developed using silicon technology in the last several decades have radically changed our way of life. However for some applications such as high power or frequency equipment, silicon is not ideal. Diamond with its large band gap and thermal conductivity and bulk insulating properties could be used. In this experiment, we investigated hydrogen terminated diamond [1]. In this case, the last carbon atoms of the diamond were bonded to hydrogen (H). The difference in electronegativity between the carbon and hydrogen atoms yielded a very thin two-dimensional layer of holes that can be used for a transistor channel.

To illustrate the possibilities of ICs on diamond, we attempted to fabricate several simple electronic devices, namely, transistors, logic inverters, and ring oscillators. A transistor is the fundamental building block of ICs that only allows current flow if a voltage is applied to the gate. An important property for device fabrication is that transistors be normally off, or have no current flowing when no voltage is applied to the gate. Inverters simply flip logic high (1) into a logic low (0) and vice versa. Ring oscillators are more complex device made of an odd number inverters connected in a ring. An input signal is then continually flipped from high to low, ideally yielded an output sine wave. To fabricate these devices, we used a process called microlithography, which uses light to ‘draw’ on an optically sensitive material covering the sample.

Experimental Procedure:

The electronic devices were fabricated using a standard sequence of nanofabrication steps.

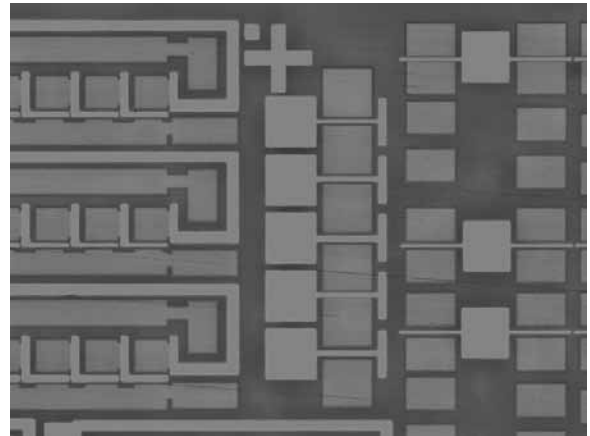


Figure 1: The sample just before the gold source-drain layer was deposited.

First, a square 5 mm H-terminated diamond sample was chosen as the substrate. We used the software Vectorworks to create a layout, measuring 3.5 mm × 4 mm, that was eventually patterned onto the substrate. The patterning process built the devices in a series of layers. The general sequence of steps was spin coat the resist, apply laser lithography, develop, deposit material, and finally liftoff. Once one layer was completed, we systematically moved onto the next.

Photolithography was conducted on a maskless system. Unfortunately our samples were not perfectly flat so the auto-aligning system could not be used. The material deposition step varied based on the layer. For example, the mesa layer consisted of ozone cleaning to strip the hydrogen terminated ends and remove conductivity from the uncovered regions. All other layers deposited a palladium (5nm)/titanium (10nm)/gold (150nm) onto the surface. For the gate region, 30 nm of aluminum oxide was deposited first by atomic layer deposition.

See Figure 1 for a visual representation of the sample, late in the process. Here, lithography and development have already happened for the final layer, so the bare substrate is visible.

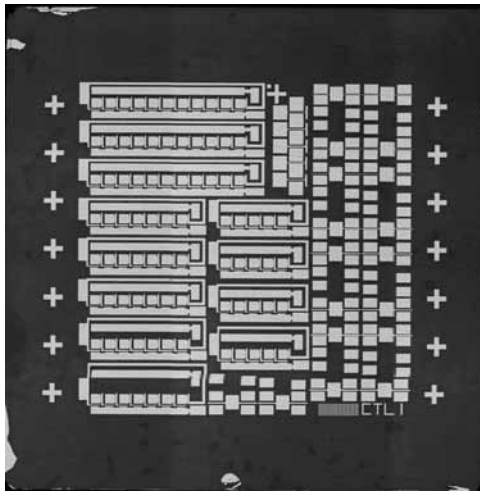


Figure 2: The completed chip with ring oscillators on the left and inverters on the right.

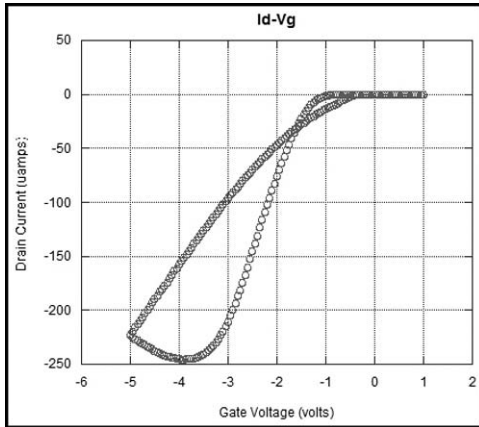


Figure 3: Plot of drain current (I_d) versus gate voltage (V_g), sweeping the voltage in both directions to observe hysteresis.

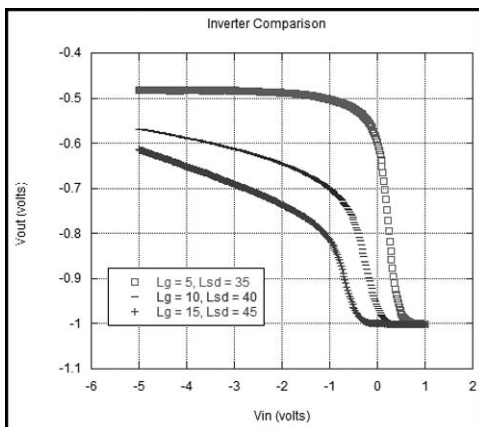


Figure 4: Illustration that inverter operation is more successful for smaller values of gate length.

Results and Conclusions:

We successfully fabricated functioning transistors and inverters on a hydrogen terminated diamond substrate. During the experiment, we fabricated devices in two different orders. In the first batch, they were source-drain first and the second gate first. In theory, the order should not have a large effect on the final functionality of the device. In practice, the normally on/off characteristics were dependent on this order. Depositing the gate first yielded a much higher percentage of normally off devices. This satisfied one of our goals to consistently fabricate normally off devices.

Figure 3 illustrates this using an I_d - V_g graph. Here it is clear that the no current is flowing when zero voltage is applied to the gate. In these transistors, the average drain current achieved was on the order of a milliamp.

A second interesting conclusion can be drawn from Figure 3; there was a major difference in the transistor properties depending on if we swept the gate voltage in forward or reverse. This is known as hysteresis. A possible explanation for this comes from the two-dimensional nature of the charges in the channel, and capture and emission phenomena between holes and defect trap. This may have contributed to the ring oscillators not functioning.

Finally, Figure 4 shows successful inverter operation. Ideal inverters would very sharply transition from high to low voltage. Greater separation between the high and low voltage is also desired. Therefore we observe that inverters with narrower gate lengths perform better. In the same way (graph not pictured), smaller source drain distances perform better. These results were expected because transistors generally perform better at smaller scales.

Future Work:

Possible directions that this research could take in the future include theoretical explanations of the normally off and hysteresis behavior. The causes of these effects are still only loosely understood. There is also a chance that a good model for the hysteresis could facilitate ring oscillator construction.

Acknowledgements:

I would like to thank the National Nanotechnology Infrastructure Network International Research Experience for Undergraduates and the National Science Foundation for funding this research. Additionally, the welcoming and friendly environment that the National Institute for Materials Science provided was appreciated. Finally I would like to thank my research group for guiding and helping me through the project: Dr. Koide, Dr. Watanabe, Dr. Imura, Dr. Liu, and Dr. Tsuya.

References:

- [1] H. Kawarada, et al., Appl. Phys. Lett. 65, 1563-1565 (1994).

Mobility of the Two-Dimensional-Electron-Gas in Lattice-Matched InAlN/GaN Grown by Ammonia Molecular Beam Epitaxy

Frank John Luciano, IV
Material Science and Engineering / Physics / Mathematics,
University of Florida

NNIN REU Site: UCSB Nanofabrication Facility,
 University of California, Santa Barbara, CA
 NNIN REU Principal Investigator: Dr. James S. Speck, Materials Department,
 University of California, Santa Barbara
 NNIN REU Mentor: Erin C.H. Kyle, Materials Department, UCSB
 Contact: fluciano4@ufl.edu, speck@mrl.ucsb.edu, kylee5042@gmail.com

Introduction:

Transistors are components on electronic boards that amplify signals and power and relay these to the rest of the electronics board. A novel model of a transistor is the high electron mobility transistors (HEMTs), which has several advantages over other transistors: high power per unit width, high frequency, high voltage operation, and low noise [1]. HEMTs operation occurs from the modulation of a two-dimensional-electron-gas (2DEG). The 2DEG channel is created at the interface of two different materials where the conduction band bends below the Fermi-level. In this channel, the material acts like a metal, hence a high mobility. The $\text{In}_{0.18}\text{Al}_{0.82}\text{N}/\text{GaN}$ material, abbreviated InAlN/GaN, has great potential as a HEMT. One reason is that the material is lattice matched — meaning there is no internal strain [2]. Despite this, growing the bi-material system is difficult because InAlN must be grown at lower temperatures than GaN for In incorporation, typically resulting in poor material quality [3].

A method of growing InAlN/GaN is using molecular beam epitaxy (MBE); conventionally, plasma-assisted MBE using pure nitrogen is used, whereas using ammonia as the nitrogen source is less thoroughly studied. However, ammonia-MBE has potential due to higher achievable growth temperatures and a nitrogen-rich environment. This project studied the effects of the growth-temperature-interrupt-depth and InAlN-layer thickness on electrical properties.

Experimental Procedure:

Samples were grown using molecular-beam-epitaxy (MBE) which uses high temperatures and low pressures to sublime gallium (Ga), aluminum (Al), and indium (In) metal targets onto a substrate and simultaneously flowing ammonia (NH_3) to grow the InAlN/GaN layers. Two series were grown: the first to optimize the growth-temperature-interrupt-depth (GTID), and a second series was grown to optimize the InAlN-layer thickness (See Figure 1). All samples had a very thin 1 nm layer of AlN at the InAlN/GaN interface to improve the mobility [3]. All samples from Series-1 had an arbitrary InAlN thickness of 10 nm, and the samples from Series-2 (dependent on electrical results from Series-1) had a GTID of 2.5 nm. The Series-2 sample with an InAlN thickness of 10 nm was the same sample from Series-1 with a GTID of 2.5 nm. A photolithography procedure was used to pattern parts of the sample for electrical measurements (See Figure 2).

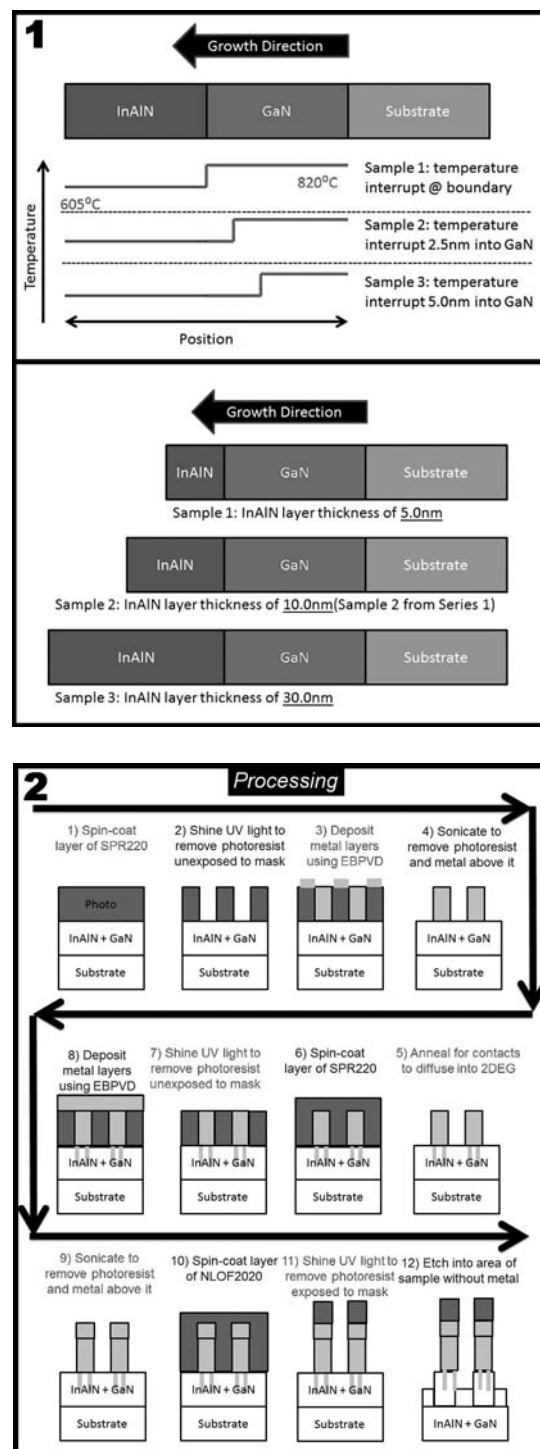


Figure 1, top: (a) Series-1 variation of growth-temperature-interrupt-depth. (b) Series-2 variation of InAlN thickness.

Figure 2, bottom: Overview of photolithography procedure, including before and after images, process flow chart, and Hall/TLM patterns.

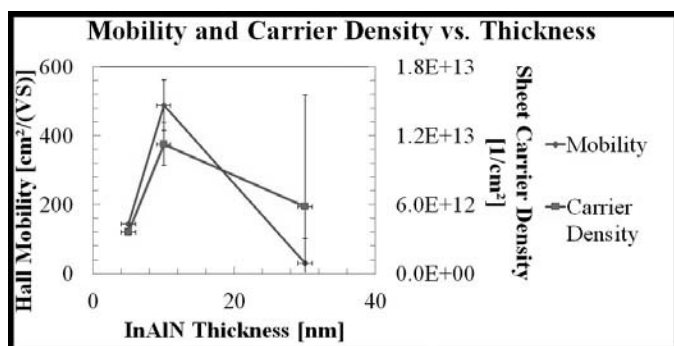


Figure 3: Series-2 mobility (blue) and carrier density (red) dependence on InAlN thickness.

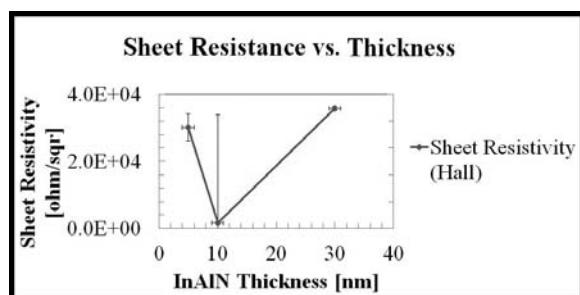


Figure 4: Series-2 sheet resistance dependence on InAlN thickness.

Results and Conclusions:

High-resolution-x-ray-diffraction (HRXRD) was performed on the MRD PRO Thin Film Diffractometer instrument to determine the crystallographic structure and to validate the atomic ratio of In:Al. The $\langle 002 \rangle$ peak was analyzed; using Bragg's law, known lattice constants of $\text{In}_x\text{Al}_{1-x}\text{N}$ materials, and the spacing between peaks, the In:Al ratio were calculated in all samples to be $0.15 < x < 0.20$, near-desired $x \sim 0.18$.

Atomic force microscopy (AFM), performed using the Asylum MFP3D instrument, was used to characterize surface topography and roughness, which is defined to be the root-mean-square (RMS) height of a scanned region of the sample. An inversely proportional relationship between roughness and InAlN thickness would be expected, which was not observed in Series-2. For this series, the 10.0 nm InAlN-layer thickness had a RMS roughness of 1.82 nm, much lower than the other two samples grown.

Electrical results (see Figure 3 and 4), done using the Hall patterns from photolithography, were measured using the Lake Shore Hall measurement system; parameters investigated include mobility, carrier density, and sheet resistance.

The average hall mobility of the 2.5 nm GTID sample of Series-1 was a factor five higher than the other two samples, at a value of $488 \text{ cm}^2/\text{Vs}$. Additionally, its carrier density was the highest at a value of $1.13 \times 10^{13} \text{ cm}^{-2}$, and it had the lowest sheet resistance of $1570 \text{ } \Omega/\square$. When the Series-2 samples were grown to optimize InAlN-layer thickness, the 10.0 nm InAlN-layer thick sample had the highest mobility, carrier density, and lowest sheet resistance.

At a deeper GTID, the portion of the GaN layer grown at the lower temperature would be much rougher, causing the 2DEG and the InAlN-layers to also be rough and the material quality would be poor. A GTID at the interface will add a high unintentional dopant concentration near the 2DEG, scattering carriers. These arguments could explain why optimum electronic properties were observed at the 2.5 nm GTID. For the InAlN-layer thickness, a thinner layer will cause a loss of charge in the 2DEG from the Schottky barrier height but a thicker layer will decrease transconductance for HEMT devices.

Despite the observations of this work, there are several further steps to be made on the project before the material can be commercialized. The first includes confirming these reported trends to confirm the optimization of these growth parameters. Beyond this, there are other growth conditions that can be worked on, such as growing the precise stoichiometric $\text{In}_{0.18}\text{Al}_{0.82}\text{N}$.

Acknowledgments:

This work was supported by the U.S. Defense Threat Reduction Agency (Dr. James Reed), and the National Science Foundation (MRSEC) to the University of California: Santa Barbara. F. Luciano acknowledges the NSF National Nanotechnology Infrastructure Network Research Experience for Undergraduates Program for the financial support, and the UCSB Nanofabrication Facility.

References:

- [1] Mishra, U. K., Parikh, P., and Wu, Y. F AlGaIn/GaN HEMTs; an overview of device operation and applications. *Proceedings of the IEEE*, 90(6), 1022-1031 (2002).
- [2] Hoi Wong, M., Wu, F., Humi, C. A., Choi, S., Speck, J. S., and Mishra, U. K. Molecular beam epitaxy of InAlN lattice-matched to GaN with homogeneous composition using ammonia as nitrogen source. *Applied Physics Letters*, 100(7), 072107-072107 (2012).
- [3] Jeganathan, K., Shimizu, M., Okumura, H., Yano, Y., and Akutsu, N. Lattice-matched InAlN/GaN two-dimensional electron gas with high mobility and sheet carrier density by plasma-assisted molecular beam epitaxy. *Journal of crystal growth*, 304(2), 342-345 (2007).

Electro-Mechanical Characterization of Gold Nanowire Meshes

Connor G. McMahan

Mechanical Engineering, Massachusetts Institute of Technology

NNIN REU Site: Colorado Nanofabrication Laboratory, University of Colorado, Boulder, CO

NNIN REU Principal Investigator: Dr. Mark P. Stoykovich, Chemical and Biological Engineering, University of Colorado at Boulder

NNIN REU Mentor: Ian P. Campbell, Department of Chemical and Biological Engineering, University of Colorado at Boulder

Contact: cmcmahan@mit.edu, mark.stoykovich@colorado.edu, ian.p.campbell@colorado.edu

Abstract:

The fabrication of stretchable interconnects is imperative for producing stretchable and flexible microelectronic devices, but current patterning approaches are limited to micron-scale features. Successful fabrication of smaller stretchable devices requires the use of new patterning methods, and block copolymer lithography is an emerging technique capable of patterning feature sizes below 10 nm. Upon self-assembly, lamellar-forming block copolymers generate a pattern colloquially known as the “fingerprint” morphology, due to the loops, whorls, and curved interfaces. The lamellar pattern shares many structural features with stretchable interconnects for macroelectronics, and successful translation of the pattern into functional materials may enable the production of stretchable electronic devices at sizes magnitudes smaller than state-of-the-art.

In this work, lamellar-forming polystyrene-block-poly(methyl methacrylate) (PS-*b*-PMMA) was used as a template to fabricate continuous gold nanowire networks (nanomeshes). The sheet resistance of these nanomeshes was below 1000 Ω/\square and the nanomeshes were nearly transparent, with transmittances greater than 85% across the visible spectrum. Successful transfer of the nanomeshes to stretchable substrates showed that nanomesh continuity was maintained during strain — because the path length between network nodes was much greater than the distance between nodes, allowing individual nanowires to elongate and straighten in the direction of strain while maintaining continuous pathways for charge transport.

Introduction:

The motivation of our research is the miniaturization of stretchable and flexible electronic devices. The fabrication of stretchable and flexible microelectronics depends on the fabrication of stretchable and flexible interconnects that present nanoscale features, but current interconnects, known as microribbons, are several microns wide. The nanoscale morphological analogues of microribbons are nanowire networks that assume patterns created by the random self-assembly of lamellar block copolymer structures.

The block copolymer template we use is polystyrene-block-poly(methyl methacrylate) (PS-*b*-PMMA). Since we want

continuous nanowire networks, it is important to adjust the composition of PS-*b*-PMMA so that there is a continuous PMMA domain over the wafer. The curvy domains of the block copolymer ensure that the nanowire network will be stretchable once fabricated because the path length between two points is significantly larger than the distance between them. When submitted to a strain, wires will straighten and align themselves in the direction of the force, ensuring that network continuity is maintained.

Fabrication Process:

Block copolymer self-assembly was the first step in the fabrication process of the nanowire networks. A polymer brush was applied to a silicon oxide wafer. This allowed the lamellar structures of PS-*b*-PMMA to orient themselves perpendicularly to the wafer, assuming a two dimensional structure. To achieve lamellar PS-*b*-PMMA structures with a PMMA domain that was continuous throughout the wafer area, the block copolymer’s volume fraction had to be adjusted so that there was slightly more PMMA than PS. The end result of this process was a block copolymer that presents a “fingerprint” morphology.

The next step in the process was to remove the continuous PMMA domain from the wafer by exposing the sample to UV light and submerging it in acetic acid. This was followed by a descum step with an oxygen plasma reactive ion etch (RIE), completing a template for continuous nanowire networks. A 2 nm chrome adhesion layer was evaporated, followed by evaporating the desired thickness of gold. PS was then removed by sonicating the sample in toluene, and the nanowire network was all that remained on the silicon oxide, as seen in Figure 1.

Finally, the nanowires were undercut by an SF₆ plasma RIE and transferred to a stretchable or flexible substrate.

Results and Conclusions:

The nanomesh sheet resistance was measured using a two-point probe. We used manually-placed silver epoxy dots as electrodes, verifying under an optical microscope that the electrodes were not short-circuiting the probe measurement, and found areas that were conductive over distances of a few hundred microns.

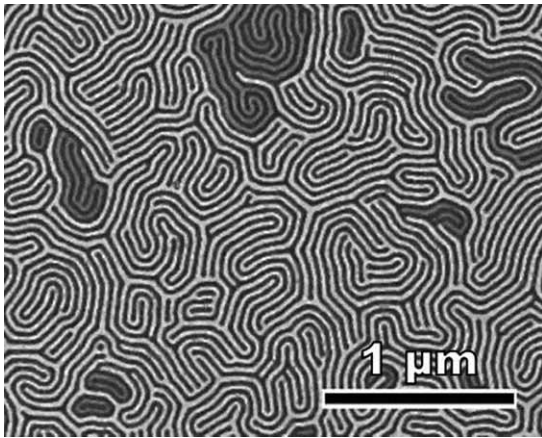


Figure 1: Gold nanomesh. The brighter nanowires are part of a continuous network.

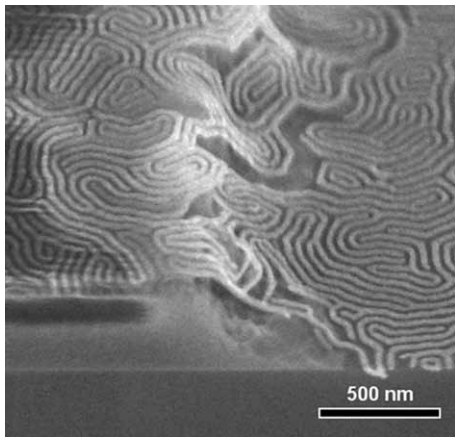


Figure 2: Nanowires stretching to accommodate different step heights.

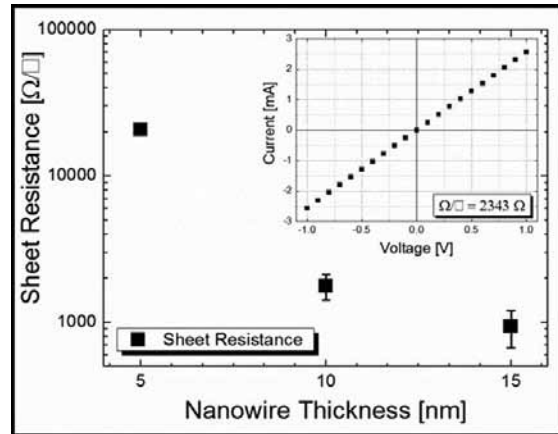


Figure 3: Sheet resistance of nanomeshes of various thicknesses.

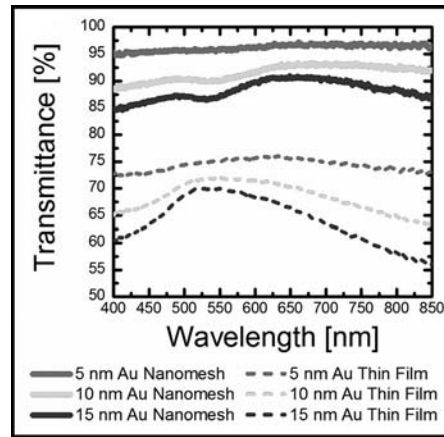


Figure 4: Optical transmittance of nanomeshes throughout the visible spectrum.

Prior to transferring the nanowires to a flexible or stretchable substrate, sheet resistances for nanomeshes of different thicknesses were measured. Nanomeshes that were 15 nm thick had sheet resistances of under 1000 Ω/\square . As the nanomesh thickness decreased to 10 nm, the sheet resistances increased to 2000 Ω/\square . Transmittances of over 85% were achieved throughout the visible spectrum for 15 nm thick nanowires, a very significant improvement over gold films of the same thickness.

After transferring a different 15 nm nanomesh to a flexible substrate, we achieved a sheet resistance of 3200 Ω/\square , showing that the continuity of the network was preserved during the process of transferring the nanowires to a stretchable or flexible substrate.

Our fabrication process was not exclusive to gold nanomeshes. We have also fabricated chrome, zinc oxide, aluminum, silver, copper, and amorphous silicon networks. As a side project, we used nanowire networks composed of these different materials as etch masks for high aspect-ratio anisotropic etching, achieving etches that were several hundred nanometers deep with mask structures that were 25 nm wide. This significantly

increased the light absorption of silicon, and could potentially be used to increase the efficiency of solar cells.

Future Work:

The focus of the project was to characterize the electrical and optical properties of gold nanowire networks, as we strived to achieve low sheet resistance and high optical transmittance over the visible light spectrum. We reached these goals and determined that the next step that should be taken in future research is to fabricate devices that are connected by stretchable nanomeshes, as the end goal is to enable the fabrication of stretchable or flexible microelectronics.

Acknowledgements:

I would like to thank Ian P. Campbell, Prof. Mark Stoykovich, and his group, my fellow REU interns, the Colorado Nanofabrication Laboratory and the Nanomaterials Characterization Facility at the University of Colorado at Boulder, the NNIN REU Program and the National Science Foundation.

Growth of Molybdenum Disulfide Atomic Layers

Brendan McMurtray

Chemical Engineering, University of Maryland, Baltimore County

NNIN REU Site: Howard Nanoscale Science and Engineering Facility, Howard University, Washington, DC

NNIN REU Principal Investigator: Dr. Jason Matthews, Department of Chemistry, Howard University

NNIN REU Mentor: Mr. Crawford Taylor, Department of Electrical and Computer Engineering, Howard University

Contact: bmcourt1@umbc.edu, jsmatthews@howard.edu, crawford@msrce.howard.edu

Abstract:

The deposition of atomic layers of molybdenum disulfide (MoS_2) using a single-source precursor has been investigated. The single-source precursor tetrakis (diethylaminodithiocarbamate) molybdate(IV) ($\text{Mo}(\text{Et}_2\text{NCS}_2)_4$) was synthesized via two routes: a) Molybdenum hexacarbonyl $\text{Mo}(\text{CO})_6$ was reacted with tetraethylthiuram disulfide ($\text{Et}_2\text{NC}(\text{S})\text{SSC}(\text{S})\text{NET}_2$), and b) Potassium diethylaminodithiocarbamate ($\text{KS}_2\text{CN}(\text{C}_2\text{H}_5)_2$) was reacted with $\text{Mo}(\text{CO})_6$. The precursor was purified by annealing at 150°C in a tube furnace, and utilized in the metal-organic chemical vapor deposition (MOCVD) growth of MoS_2 on SiO_2 . The resulting atomic layers of MoS_2 were analyzed via scanning electron microscopy (SEM) and accompanying energy-dispersive x-ray spectroscopy (EDS).

Introduction:

Atomically-thin MoS_2 is a direct band gap semiconductor that exhibits interesting optical and electric properties [1, 2]. MoS_2 has been used to fabricate invertors, Negated AND (NAND) gates, and ring oscillators [2]. There are only a few single-source precursors that have been investigated for use in the deposition of thin films of MoS_2 via MOCVD. Factors affecting implementation of CVD precursors include volatility, thermal stability, and the ability to deposit the desired material in high purity. Our current study examined several synthetic routes towards producing an air and moisture stable precursor, tetrakis (diethylaminodithiocarbamate) molybdate(IV) ($\text{Mo}(\text{Et}_2\text{NCS}_2)_4$) [3, 4].

Experimental Procedure:

Tetraethylthiuram disulfide (2.25g, 7.6 mmol) and acetone (25 mL) were added to a 100 mL Schlenk flask. In an inert atmosphere glove box, molybdenum hexacarbonyl (1.00g, 3.8 mmol) was added to a separate 100 mL Schlenk flask. The $\text{Mo}(\text{CO})_6$ was removed from the glove box, and the acetone solution of tetraethylthiuram disulfide was added via

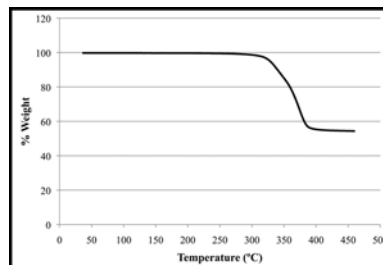


Figure 1: Mass % of sample as a function of temperature.

cannula. The mixture was stirred at reflux for two hours, and the formation of a purple precipitate was observed. The reaction mixture was allowed to cool, and the solvent was removed under vacuum allowing for the isolation of the solid purple precipitate.

The resulting product was vacuum filtered and washed with pentane, dried, and annealed at 150°C in a tube furnace to remove unreacted starting material. The formation of the desired precursor was confirmed using Thermogravimetric Analysis (TGA), with a single weight-loss step at 320°C that can be clearly identified in Figure 1 [4].

The second synthetic route made use of a two-step approach. A solution of potassium hydroxide (KOH) and diethylamine in ethanol was stirred for 15 minutes; a slight molar excess

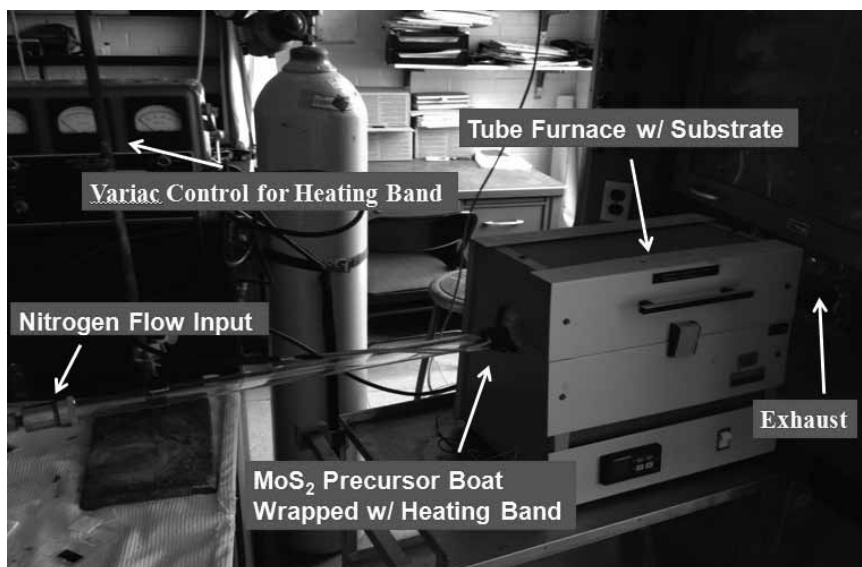
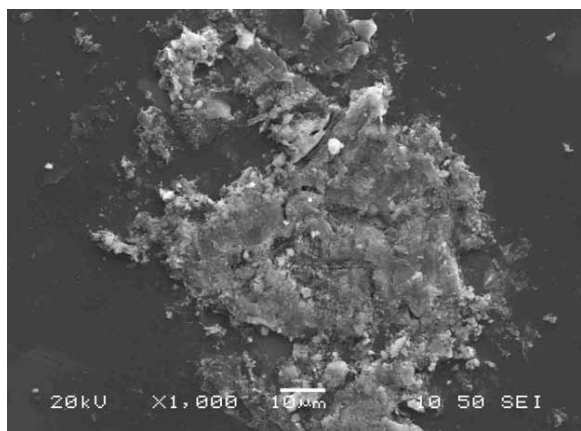


Figure 2: Horizontal hot-wall CVD reactor for growing MoS_2 thin films.



Element	Atomic%
S	57.11
Ca	0.42
Zr	2.71
Mo	39.76
Totals	100.0

Table 1: Atomic percent by element.

Figure 3: Patch of MoS_2 on SiO_2 substrate.

of carbon disulfide (CS_2) was added. The resulting mixture was allowed to stir for two hours, after which the solvent was removed via a rotary evaporator. Using a three-step trituration process, the dried precipitate ($\text{KS}_2\text{CN}(\text{C}_2\text{H}_5)_2$) was purified. The yellow powder was dried overnight, and the potassium salt was confirmed via ^1H nuclear magnetic resonance analysis. The potassium diethylaminodithiocarbamate was refluxed in a 4:1 molar ratio with $\text{Mo}(\text{CO})_6$ using the same synthetic procedure as was used with tetraethylthiuram disulfide. Unfortunately, this synthetic route did not yield significant amounts of the desired precursor.

Once the desired precursor was synthesized, the horizontal hot-wall CVD reactor was designed as shown in Figure 2. Several different substrates were tested, including silicon (Si), silicon dioxide (SiO_2), gold-plated Si, nickel-plated Si, gold-plated SiO_2 , and nickel-plated SiO_2 . The substrate was placed vertically in a boron nitride boat in the CVD reactor and held at temperatures of 425°C , 550°C , and 675°C for three different experiments. The precursor was sitting in a boron nitride boat approximately three inches from the substrate at a temperature of 320°C or 365°C . We carried out all trials with a nitrogen flow rate of $7\text{ cm}^3/\text{min}$, $10\text{ cm}^3/\text{min}$, $15\text{ cm}^3/\text{min}$, or $25\text{ cm}^3/\text{min}$. All specific treatment combinations were tested in the CVD reactor in order to elicit the most effective means of producing pure thin films of MoS_2 .

Results and Conclusions:

After examining all combinations of independent variable levels, it was determined that the prime conditions for obtaining MoS_2 were a substrate temperature of 675°C , a precursor temp-

erature of 365°C , and a nitrogen flow rate of $15\text{ cm}^3/\text{min}$. The precursor boat was refilled twice for a total of three runs, and each run lasted for 15 minutes. Unfortunately, no combination of parameter values achieved an even coating of the substrate, but we were able to obtain patches of MoS_2 , one of which can be seen in Figure 3.

MoS_2 patches were accurately identified via EDS; Table 1 displays the EDS results from the patch seen in Figure 3. As we can see, the atomic percentage of the deposited MoS_2 sample is 57.11:39.76 or $\sim 1.44:1$, which is approximately a 28% error from the 2:1 atomic ratio of sulfur and molybdenum in MoS_2 . Therefore, MoS_2 was successfully deposited; however, a more suitable precursor needs to be identified.

Moving forward, further analysis is needed on the deposited material to confirm the presence of MoS_2 . In addition, the second synthetic method involving the potassium salt needs to be refined in order to promote the production of the desired precursor. TGA results in Figure 1 indicate the synthesized precursor is thermally unstable; that is, the first synthetic method leaves residual impurities. This coupled with the fact that large-area MoS_2 deposition was not obtained, means that there is a need for further study of this single-source precursor platform in the form of a structure activity relationship.

Acknowledgements:

I would like to thank Mr. Crawford Taylor, Dr. Jason Matthews, and all the staff at the Howard Nanoscale Science and Engineering Facility (HNF) and Howard Chemistry Department. I also would like to express my gratitude towards the National Nanotechnology Infrastructure Network Research Experience for Undergraduates (NNIN REU) program and the National Science Foundation (NSF) for making this awesome internship opportunity possible.

References:

- [1] K.F. Mak, et al., Phys. Rev. Lett. 2010, 105.13605, 1-4.
- [2] H. Wang, et al., Nano Lett. 2012, 12.9, 4674-80.
- [3] T. Ouyang, et al., The Journal of Phys. Chem. B. 2004, 108.45,17537-45.
- [4] R. Lozano, et al., An. Quim. 1983, B79, 41.

Growth and Characterization of Synthetic Diamond

Veronica Medrano

Electrical Engineering, Texas A&M University

NNIN REU Site: Howard Nanoscale Science and Engineering Facility, Howard University, Washington, DC

NNIN REU Principal Investigator: Dr. Gary Harris, Electrical Engineering, Howard University

NNIN REU Mentor: James Griffin, Electrical Engineering, Howard University

Contact: ronniem08@neo.tamu.edu, gharris@msrce.howard.edu, jagriffin@howard.edu

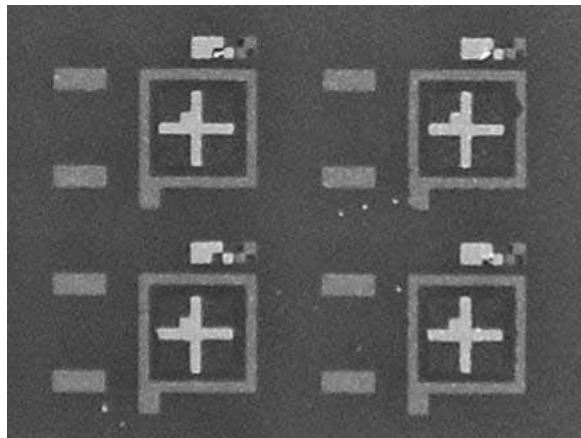


Figure 1: Top view of fabricated diamond device (crosses are Schottky contacts and outer squares are ohmic contacts).

Abstract:

Diamond exhibits superior material properties such as high breakdown field, high saturation velocity, high carrier mobilities, optical transparency over a wide transmission range, and the highest thermal conductivity of all materials [1]. These properties make it desirable to deliver future high quality electronic devices and detectors. Hot filament chemical vapor deposition (HFCVD) was used to grow polycrystalline diamond on various substrates. Atomic force microscopy (AFM) and scanning electron microscopy (SEM) confirmed diamond growth due to the resulting diamond facets on the substrate surfaces. Diamond grown on diamond yielded the highest grain size. A Raman shift value of 1332 cm^{-1} confirmed the presence of high quality polycrystalline diamond. Titanium-gold (Ti-Au) ohmic contacts were fabricated and annealed at 950°C for ten minutes in an H_2/Ar ambient environment. Linear-IV curves confirmed ohmic behavior. Nickel (Ni) was used as a Schottky contact and its IV curve was nonlinear as expected. Electrical properties of selected diamond films were also analyzed using the Hall effect. Diamond grown on 3C-SiC yielded a mobility of $221\text{ cm}^2/\text{v}\cdot\text{s}$ and carrier concentration of $7.2\text{E}16\text{ cm}^{-3}$.

Introduction:

The first “manmade diamond” was created by General Electric in 1956, using a process called high pressure high temperature (HPHT). This method imitates natural diamond formation, but with carefully selected input materials to catalyze crystal growth [2]. In recent years, chemical vapor deposition (CVD) has been used to produce diamond from a heated mixture of hydrocarbon gas and hydrogen in a vacuum chamber at very low pressures. The method is less expensive and more suitable for diamond growth in the semiconductor industry. This project employed a hot filament CVD system to grow synthetic diamond on various substrates.

Experimental Procedure:

Silicon dioxide (SiO_2)-coated Si, 3C-SiC coated Si, and 6H-SiC were seeded with nanodiamond slurry solution in an ultrasonic bath for ten minutes. This was done in order to create nucleation centers for diamond growth. The samples were then loaded in the HFCVD reactor. Also, the backside of a nanocrystalline diamond layer removed from silicon was loaded. The filament-to-sample gap was set to 20 mm, and hydrogen (H), methane (CH_4), and argon (Ar) gases were introduced. The H_2 flow rate was set to 60 sccm and the CH_4 flow rate was set to 1 sccm.

When the process pressure (20 torr) and the sample temperature (750°C) were reached, the filament temperature was raised to 2300°C . Growth of diamond was then initiated. After growth, the samples were removed and characterized. Titanium (Ti, 20 nm) and gold (Au, 150 nm) were deposited by electron-beam evaporation to fabricate ohmic contacts while Ni (100 nm) was deposited to make the Schottky contacts. The ohmic contacts were annealed at 950°C for ten minutes in an H_2/Ar ambient environment using a tube furnace.

Figure 1 shows the top view of the created device. A Hall effect setup was used to measure mobility, resistivity, and carrier concentration.

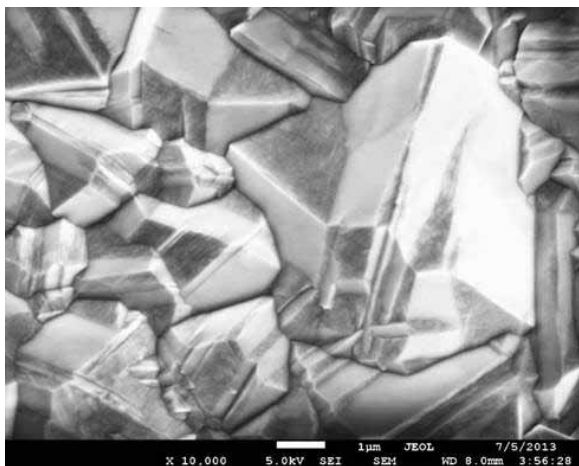


Figure 2: SEM image of diamond grown on diamond.

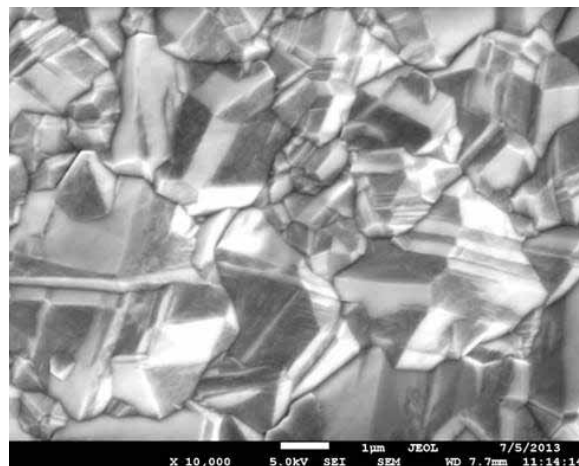


Figure 3: SEM image of diamond grown on 3C-SiC.

Results and Conclusions:

Diamond growth using HFCVD was conducted successfully, as seen in the resulting polycrystalline facets shown on SEM and AFM images. Diamond grown on diamond yielded the largest grain size ($\sim 7 \mu\text{m}$), compared to sizes of $5 \mu\text{m}$ (Si) and $4 \mu\text{m}$ (6H-SiC and 3C-SiC) as shown in Figures 2 and 3. Larger grain sizes should translate into improved carrier transport.

Diamond grown on all substrates had a thickness of $12.3 \mu\text{m}$. Roughness did not play a huge role in the results since the AFM revealed similar roughness (210-254 nm) for diamond on the various substrates. A Raman spectroscopy graph confirmed the presence of high quality polycrystalline diamond growth due to the diamond peak value of 1332 cm^{-1} (Figure 4). The full-width half-maximum value was measured to be 15 cm^{-1} , close to diamond's true value. Ti-Au ohmic and Ni Schottky contacts were successfully fabricated with linear and nonlinear curves, respectively, although the Schottky behavior was not ideal. Hall effect measured a mobility of $221 \text{ cm}^2/\text{v}\cdot\text{s}$, resistivity of $0.39 \Omega\cdot\text{cm}$, and carrier concentration of $7.2\text{E}16 \text{ cm}^{-3}$. These measurements are similar to previously published data.

Successful diamond growth and electrical fabrication indicates the potential use of these materials in engineering applications. This project is significant for promoting further research of diamond growth and characterization, especially since this novel material has been complex to study over the years.

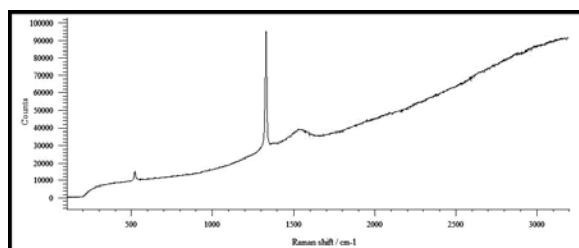


Figure 4: Raman curve of polycrystalline diamond film grown by HFCVD.

Future Work:

The barrier heights of various metals on diamond by internal photoemission will need to take place in the future in order to further analyze metal-diamond interfaces in fabricated diamond devices. The doping of diamond needs to be investigated as well. In addition, research must be done on finding ways to grow single crystal diamond in order to generate more advanced electronics. It may also be necessary to see how different metal contacts play a role in the quality of electrical devices.

Acknowledgements:

I wish to thank my Principal Investigator Dr. Gary Harris, Ph.D., P.E, the National Nanotechnology Infrastructure Network Research Experience for Undergraduates (NNIN REU) Program, Howard Nanoscale Facility, and the National Science Foundation (NSF) for making this project possible and giving me the opportunity to be a part of it. In addition, the mentorship of James Griffin and assistance of Laila Carter and Bokani Mtengi was invaluable over the summer.

References:

- [1] Gabrysch, M. (2008). Electronic Properties of Diamond. Uppsala, Sweden: Division for Electricity Dept of Engineering Sciences. Retrieved from http://www.el.angstrom.uu.se/Seminar/MGabrysch_Lic.pdf.
- [2] <http://www.e6cvd.com/cvd/page.jsp?pageid=405>. Accessed 7/20/2013.

High Strain Low Voltage Induced Densified Vertically Aligned Carbon Nanotube Ionic Actuators

Joshua Michalenko

Electrical Engineering, New Mexico State University

NNIN REU Site: Penn State Nanofabrication Laboratory, The Pennsylvania State University (PSU), University Park, PA

NNIN REU Principal Investigator: Professor Qiming Zhang, Electrical Engineering and Materials Science, PSU

NNIN REU Mentor: Mehdi Ghaffari, Materials Science, The Pennsylvania State University

Contact: joshm44@nmsu.edu, qxz1@psu.edu, mxg1019@psu.edu

Abstract:

Electroactuation materials that can generate high strain under low voltages are crucial components in artificial muscles, robotics applications, and micro- and nano- electromechanical (MEMs and NEMs) devices. This project developed ultra-high volume density carbon nanotube (CNT)-based ionic actuators that would increase the actuation strain from a current < 1% to 20% under low voltages (< 4 volts). Using a biaxial mechanical densification (BMD) process increased the volume fraction (V_f) of the vertically aligned carbon nanotubes (VA-CNT) from 1% to 40% [1]. The densification process maintained the vertically aligned morphology of the CNTs, providing non-tortuous pathways for ion transportation. This characteristic is crucial to creating fast, efficient, and high strain actuation devices. One percent V_f CNT forests were densified to 40% V_f , infiltrated with 40%wt Nafion polymer, and immersed in two separate ionic liquids, 1-ethyl-3-methylimidazolium trifluoromethanesulfonate ([EMI⁺][Tf⁻]) and 1-butyl-3-methylimidazolium tetrafluoroborate ([BMI⁺][BF₄⁻]), for strain testing. Experimentation revealed [BMI⁺][BF₄⁻] showed largest strains of 13% under 0-3V triangular wave signals, while using [EMI⁺][Tf⁻] showed ~ 5% strains under the same conditions. These results indicated that the size difference between the cations and anions in the ionic liquid was one critical factor that drove the actuation of the device.

Introduction:

Electroactuation materials are simple devices that perform energy conversion between electrical and mechanical forms. Creating electroactuation devices that can generate large movement under low voltages is one key component to advancing the prominence of actuators in everyday life. VA-

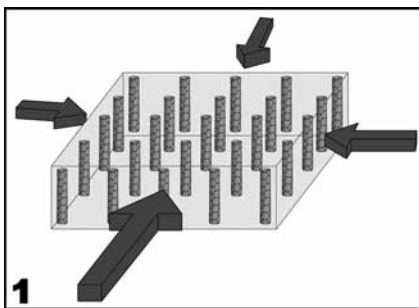


Figure 1, top: Biaxial densification process of CNT forest.

CNT based ionic actuators are a proven concept with the potential to produce high strain under low voltages [2]. By densifying the VA-CNTs, it has been theoreticized that the actuation efficiency can be significantly increased.

Fabrication and Experimental Procedure:

One percent V_f VA-CNTs were grown, 500 μm thick, on a silicon substrate using a modified chemical vapor deposition process with a Fe-on-alumina catalyst system [3]. After removal from the substrate, samples were put through a BMD process (Figure 1) to decrease the spacing between the CNTs and increase the density from 1% V_f (10 mm^2) to 40% V_f (1.6 mm^2). CNT samples were then placed in 3D metal cages with a metal mesh on the top side and were infiltrated with a 2.5% Nafion (NR-211) dispersion in DMF to contain 40% wt of NR-211. Samples were placed under vacuum at 5 mmHg for 5-7 days or until the solvent had completely dissolved. The samples were then annealed at 110°C for one hour and immersed in ionic liquid under vacuum at 5 mmHg for one day.

Various waveforms were applied to the CNT actuators in an actuation testing station and their actuation (Figure 2) was characterized with a fiber optic displacement sensor. Both ionic liquids, [EMI⁺][Tf⁻] and [BMI⁺][BF₄⁻], were utilized separately in the testing process and triangular waveforms ranging from -3-3V were tested under a 5 mv sec^{-1} scan rate.

Results, Discussion, and Conclusions:

A graph from a test showing the applied voltage as a -3-3V triangular wave and the response of the actuator is shown in

Figure 3. As voltage increased/decreased, the conductive, porous, CNT forests acted as electrodes that attracted/repelled ions of the opposite charge that filled the CNTs, causing expansion/contraction and therefore strain.

Strain is defined as the thickness difference between the initial and final states of the actuator after applying voltage. Figure 4 shows the maximum percent strain recorded from six different testing scenarios of different waveforms and ionic liquids. Phase separation in the applied voltage and response of the actuator were noted and more investigation on this topic is needed.

It was also observed that for the first 10-20 cycles of applied voltage, the actuators mostly expanded during a conditioning phase. After the conditioning phase, the actuators entered into a steady state in which the difference in sizes between the cations and anions in the ionic liquid drove the actuation process [1]. Using three different waveforms and two ionic liquids for each waveform showed that $[BMI^+][BF_4^-]$ was a more effective ionic liquid than $[EMI^+][Tf^-]$. This observation is due to the size difference between the cations and anions of the $[BMI^+][BF_4^-]$, which was greater than the difference in $[EMI^+][Tf^-]$ [4].

As higher voltage was applied, more actuation was observed. Maximum strain of 13.2% occurred under a 0-3V waveform using $[BMI^+][BF_4^-]$. These results are quite significant due to the fact that previous researchers, using undensified samples have achieved < 1% strain [5]; concluding that the densification of VA-CNTs create ionic actuators with the capability of creating higher strain than undensified samples.

Future Work:

Atomic force microscopy (AFM) measurements to obtain the elastic modulus of the CNTs will be used to calculate columbic and electromechanical efficiencies of the devices. Subsequently, a mathematic representation of the system will be formed in the sense of an electrical circuit for simulation purposes. By altering the %wt of N-211 to be added to the samples, the strain on the actuators can also be optimized.

Acknowledgments:

Thank you to my PI, Dr. Qiming Zhang, my mentor, Mehdi Ghaffari, and all of the members of the Zhang group for their guidance and support on the project. Thank you to the REU Site Coordinator Kathy Gehoski, all the members of the Nanofabrication staff, as well as our collaborators at MIT. Lastly, thanks to the National Science Foundation and the National Nanotechnology Infrastructure Network Research Experience for Undergraduates (NNIN REU) Program for funding and organizing the project.

References:

- [1] Zhou, Y., and Ghaffari, M., revision submitted to Advanced Energy Materials.
- [2] Liu, S., and Yang, Y., Advanced Functional Materials, vol. 20, pp. 3266-3271 (2010).
- [3] Wardle, B., and Saito, D., Advanced Materials, vol. 9999, pp. 1-8 (2008).
- [4] Liu, S., and Wenjuan, W., Society of Chemical Industry, vol.59, pp. 321-328 (2010).
- [5] Liu, S., PhD. thesis, The Pennsylvania State University, (2010).

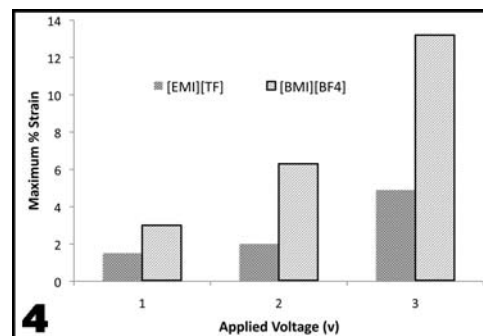
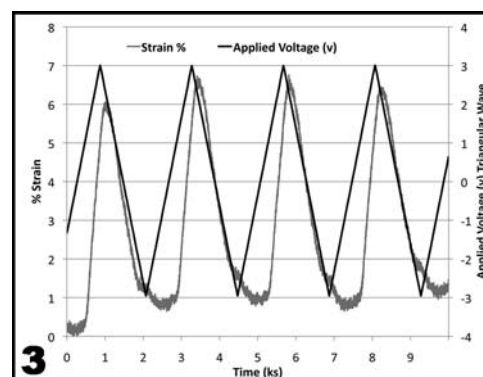
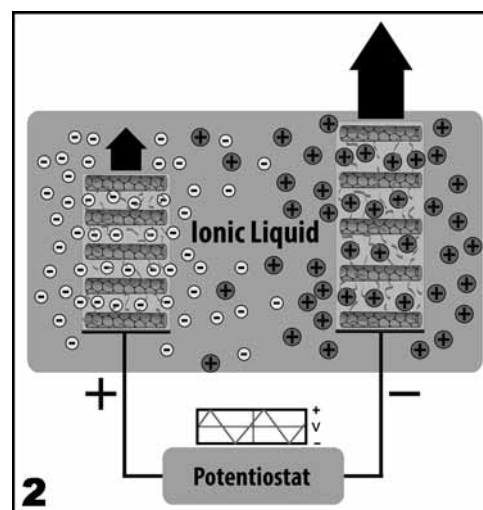


Figure 2, top: Applied voltage to CNT ionic actuators showing expansion of actuators.

Figure 3, middle: Line graph of -3-3v triangular wave being applied to actuators and response of the actuators.

Figure 4, bottom: Maximum strain percent as a function of applied voltage and ionic liquid.

Carbon Coated Tin-Seeded Silicon Nanowires for Lithium-Ion Battery Anodes

Daichi Oka

Department of Chemistry, School of Science, The University of Tokyo, Tokyo, Japan

NNIN iREG Site: Microelectronics Research Center, The University of Texas, Austin, TX

NNIN iREG Principal Investigator: Prof. Brian A. Korgel, Department of Chemical Engineering, The University of Texas at Austin

NNIN iREG Mentor: Timothy D. Bogart, Department of Chemical Engineering, The University of Texas at Austin

Contact: oka@chem.s.u-tokyo.ac.jp, korgel@che.utexas.edu, tbogart@utexas.edu

Introduction:

Lithium-ion batteries (LIBs) are widely used in many applications, such as mobile phones, laptops, and electric vehicles due to their high power density compared to other battery types. However, improvements are needed to meet the upcoming demands of new technology. Silicon (Si) has the potential to increase the power density of LIBs by replacing commercial carbon-based anodes because it has a high lithium-ion insertion capacity (Si: 3579 mA h g⁻¹ vs. C: 372 mA h g⁻¹ [1]). To accommodate the lithium (Li), the Si lattice must expand by up to 280%. While bulk Si pulverizes under these conditions, Si nanowires (SiNWs) can tolerate this volume expansion (and contraction upon delithiation [2]). However, there are challenges that must be overcome before Si can be used commercially.

Si is a poor electrical conductor, and anodes require the addition of some conductive carbon to improve anode conductivity. Additionally, gold, the typical seed metal to grow SiNWs, is known to have a negative impact on conductivity of SiNWs as gold impurities create deep electron traps in Si. Also, gold catalyzes electrolyte decomposition resulting in continuous growth of a solid electrolyte interphase (SEI) layer, reducing anode stability [3]. Tin-seeding [4] and coating with conductive graphitic carbon [5] are promising ways to overcome these difficulties. In this report we demonstrate the synthesis of carbon coated tin-seeded SiNWs via the supercritical-fluid-liquid-solid (SFLS) growth and their performances as LIB anodes.

Growth of SiNWs:

A reactant solution of 0.5 mL of monophenylsilane and 24 μ L of bis(bis(trimethylsilyl)amino)tin (Sn(HMDS)₂) in 25 mL of toluene was injected to supercritical-fluid of toluene in a titanium reactor that was heated to 490°C and pressurized to 10.8 MPa at a rate of 0.5 mL/min for 40 minutes. The amount of Sn(HMDS)₂ was changed from 24 μ L to 48, 72, or 96 μ L, corresponding to Si:Sn ratios of 65:1, 32:1, 22:1, and 16:1, respectively, in order to optimize the morphology of the SiNWs. The obtained SiNWs were characterized by scanning electron microscopy (SEM) and transmission electron microscopy (TEM).

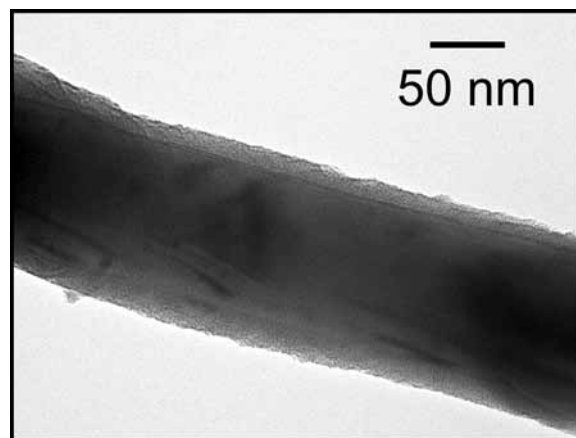
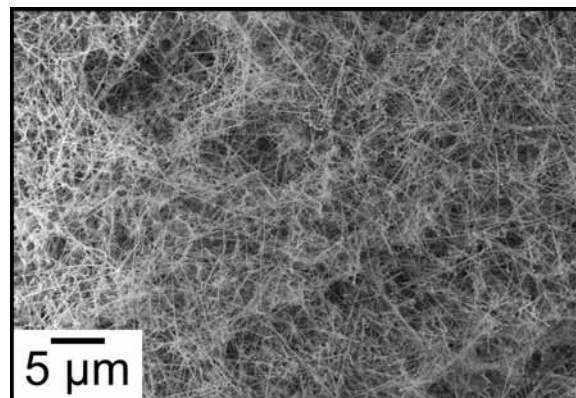


Figure 1, top: SEM of polyphenylsilane-coated tin-seeded SiNWs.

Figure 2, bottom: TEM of polyphenylsilane-coated tin-seeded SiNWs.

When the Si:Sn ratio was as high as 65:1 or 32:1, SiNWs were tortuous and highly kinked with particulate reaction byproduct. TEM also showed that there was a thick carbonaceous shell surrounding the nanowires. At a Si:Sn ratio of 22:1, the SiNWs were predominantly straight and long, 10's to 100's of microns, with no significant particulate inclusions. Figure 1 shows an SEM image of a typical nanowire sample. Figure 2 shows a TEM image of a Si nanowire with a crystalline Si core and polyphenylsilane shell.

Although the Si:Sn ratio of 16:1 also provided with straight and long SiNWs, there was almost no phenylsilane shell on these nanowires. The Si nanowires made with Si:Sn ratio of 22:1 were studied for LIB applications by electrochemically cycling against Li metal in a coin cell.

Battery Assembly and Testing:

The polyphenylsilane shell was converted to conductive graphitic carbon by annealing the nanowires under forming gas (7% H₂ in N₂) at 900°C for one hour (pyrolysis). Nanowires were tested in LIB coin cells with and without this heat treatment.

For testing in LIB coin cells, SiNWs were combined with poly(acrylic acid) binder with a 4:1 weight ratio. No conductive carbon particles were added. The mixture was dispersed in 1-methyl 2-pyrrolidinone to obtain a viscous slurry. The slurry was doctor-bladed (150 μm gap) onto copper (Cu) foil and vacuum-dried. Individual 11 mm diameter circular electrodes are hole-punched from the coated Cu foil and combined in coin cells. The assembly and testing procedures are detailed in Ref. 4.

Charge and discharge capacities were measured at rates of one cycle per ten hours (C/10) and one cycle per one hour (1C) (Figures 3, 4). At both rates, the charge capacities of the unpyrolyzed SiNWs were very low (< 1000 mA h g⁻¹) in the first cycle and decayed to 0 mA h g⁻¹ after a few cycles. On the other hand, the pyrolyzed SiNWs showed high capacities over 2500 mA h g⁻¹. Even at the higher rate of 1C, the capacities of the pyrolyzed SiNWs were over 1000 mA h g⁻¹ and stable for more than 200 cycles.

These results revealed that the carbon-coated Si nanowires have sufficient electrical conductivity for good battery performance without the need for additional carbon in the formulation, thus increasing the total battery anode gravimetric charge storage capacity.

Conclusions:

Long and straight SiNWs with nanometers-thick polyphenylsilane coatings were synthesized by SFLS growth with tin seeds. Pyrolysis of the polyphenylsilane shell to carbon led

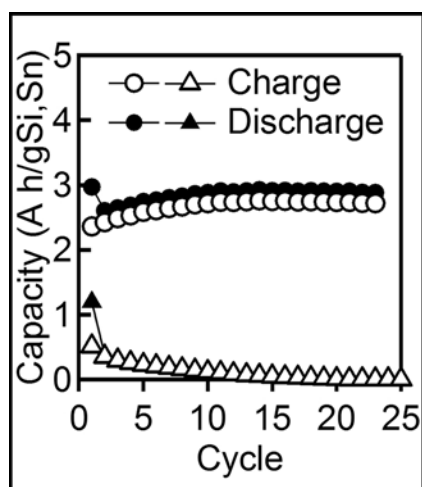


Figure 3: Charge and discharge capacities of the lithium-ion batteries with the pyrolyzed/unpyrolyzed carbon coated tin-seeded SiNWs anodes at the cycle rate of C/10.

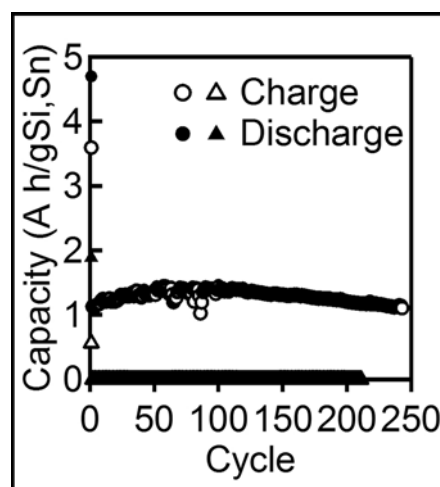


Figure 4: Charge and discharge capacities of the lithium-ion batteries with the pyrolyzed/unpyrolyzed carbon coated tin-seeded SiNWs anodes at the cycle rate of 1C.

to SiNWs with high and stable lithium insertion capacities, eliminating the need to use gold seeds for nanowire growth and the need for additional conductive carbon in the Si-based battery anode.

Acknowledgments:

I would like to thank Prof. Brian A. Korgel, Timothy D. Bogart, and all the other members of Korgel group, for their support in the research. Dr. Marylene Palard and Christine Wood helped me as the site coordinators. This work was funded by the National Nanotechnology Infrastructure Network International Research Experience for Graduates (NNIN iREG) Program/National institute for Material Science Graduate Exchange Program Fellowship, and the National Science Foundation.

References:

- [1] X. H. Liu, et al. Nano Letters 11, 2251-2258 (2011).
- [2] H. Wu, et al. Nano Today 7, 414-429, (2012).
- [3] A. M. Chockla, et al. The Journal of Physical Chemistry C 116, 18079-18086 (2012).
- [4] A. M. Chockla, et al. Chemistry of Materials 24, 3738-3745 (2012).
- [5] A. M. Chockla, et al. Journal of the American Chemical Society 133, 20914-20921 (2011).

Advanced Synthesis and Nano-Characterization of Graphene on Platinum <111> Substrates

Stephen A.O. Olson

Applied Physics, Bethel University; Electrical Engineering, University of Minnesota

NNIN iREU Site: National Institute for Materials Science (NIMS), Tsukuba, Ibaraki, Japan

NNIN iREU Principal Investigator: Dr. Daisuke Fujita, Division Director, Advanced Key Technologies Division, NIMS

NNIN iREU Mentors: Dr. Nobuyuki Ishida and Dr. Hongxuan Guo, NIMS Postdoctoral Researchers,

Nano Interface Characterization Group, NIMS; Dr. Jian-hua Gao, International Center of Young Scientists, NIMS

Contact: olso5576@umn.edu, fujita.daisuke@nims.go.jp, ishida.nobuyuki@nims.go.jp,

guo.hongxuan@nims.go.jp, gao.jianhua@nims.go.jp

Abstract:

Transition metal substrates enable growth of high-quality graphene in large sheets. We investigated graphene grown by surface precipitation and chemical vapor deposition (CVD) on platinum <111> substrates. Surface chemical composition and estimated film thickness were determined using Auger electron spectroscopy (AES). Platinum-graphene work function differences were measured with Kelvin probe force microscopy (KPFM) and shown to be correlated with fabrication methodology. Likewise, x-ray photoelectron spectroscopy (XPS) indicated that platinum-graphene charge transfer and interlayer interaction was affected by growth technique. Inverted surface topographies were observed by atomic force probe microscopy (AFM); the possibility of selective adsorption of water molecules on the substrate surface is proposed. Surface defect states were analyzed with scanning tunneling spectroscopy (STS). Supplemental topographical analysis was conducted using helium ion microscopy (HIM).

Introduction:

Graphene's many unique properties make it ideally suited for application in future technologies. An obstacle facing the commercialization of graphene-based technologies is the efficient production of large-area, defect-free graphene sheets. Transition metal substrates enable the growth of large high-quality graphene sheets; they may be well suited for the large-scale manufacturing of graphene. Platinum (Pt) <111> is one of the weakest interacting graphene-metal systems [1]; there will be less interference from the substrate affecting structural and electronic states of graphene. We wish to characterize graphene films grown on Pt <111> substrates by two methods: chemical vapor deposition (CVD) and the precipitation and segregation of carbon doped substrates (SEG). We consider the two growth methods by measuring monolayer graphene's interaction with the platinum substrate and analyzing unique surface features.

Experimental Procedure:

We began by growing the graphene films.

Segregation. Using carbon-doped platinum substrate, we initiated an 800-1000°C anneal at high vacuum. Carbon precipitated out of the substrate forming a graphene monolayer on the surface.

Chemical Vapor Deposition. At high temperature and vacuum, ethylene gas was introduced in the sample chamber. The carbon bonded to the substrate, forming a graphene monolayer on the surface.

Graphene Monolayer Existence Confirmation. Using AES, we confirmed the existence of graphene on both substrates and were able to estimate the film thickness using a simple model [2].

$$I_{sub} = I_{sub,pure} \exp\left(\frac{-d}{\lambda(E) \sin(\theta)}\right)$$

Film thickness is represented by d , θ is the Auger electron take-off angle (system dependant), λ is the electron inelastic mean free path (energy dependent), I_{sub} is the intensity of the attenuated substrate peak, and $I_{sub,pure}$ is the intensity of the pure substrate peak. This estimation does not take diffractive effects or the number of contributing platinum layers into account. It assumes AES peak intensity attenuation is caused solely by the presence of graphene. Therefore, we estimate 20-30% error using this method. However, even with this error margin, we were able to confirm that the graphene was indeed one monolayer thick.

Surface Potential Measurements. KPFM surface potential mapping revealed statistically significant relative differences in surface potentials between SEG and CVD graphene films. This voltage difference is proportional to a work function difference. We observed an average potential difference of 78 mV for SEG graphene and 103 mV for CVD graphene. We conclude that the two samples have different electronic state compositions.

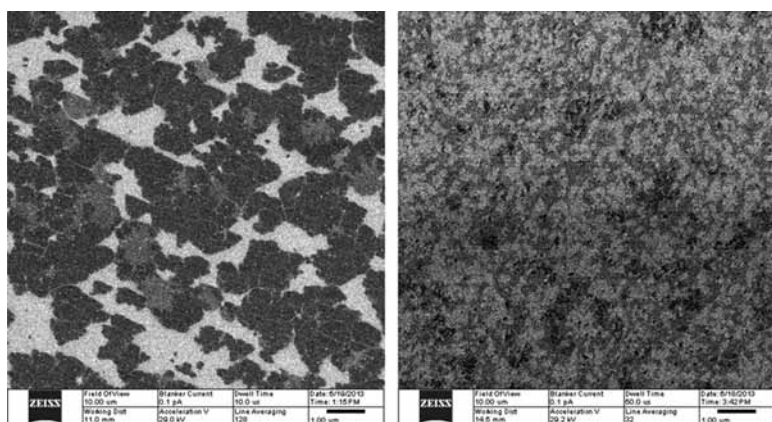


Figure 1: Helium ion microscopy images of SEG (a) and CVD (b) graphene surfaces.

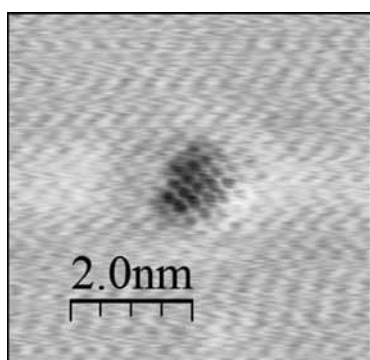


Figure 2: Atomically resolved STM image of suspended graphene.

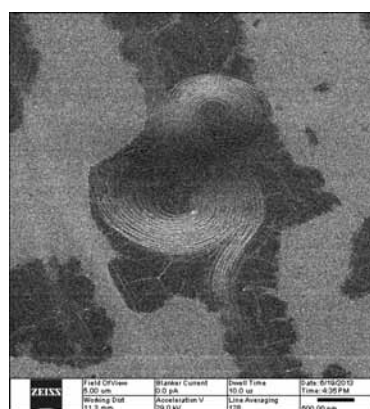


Figure 3: Unexplained graphene defect observed on surface.

XPS Measurements. X-ray photoelectric spectroscopy (XPS) measurements indicated that the binding energy of CVD graphene is lower than binding energy of SEG graphene. The binding energy of CVD graphene was measured to be 284.0 eV, while SEG graphene was at 284.2 and 284.3 eV. This indicates that CVD graphene has less interlayer interaction than SEG graphene. In contrast, segregation graphene on nickel has a binding energy of 284.9 eV, indicating stronger interlayer interaction [3].

AFM Measurements. During atomic force probe microscopy (AFM) measurements, we found the graphene-platinum height relationship inverted. Platinum was measured to be 1.2-1.4 nm higher than graphene. We believe there is a possibility that water was being adsorbed on the hydrophilic Pt <111> surface. If this was the case, it would mark the first instance of such an observation on this scale. Under vacuum, using scanning

tunneling microscopy (STM), the graphene and Pt surfaces were observed to be nearly equivalent in height. Because the surfaces were both conductive, we know that the STM tip was in close proximity to the surface, and a difference of 1.2-1.4 nm would certainly have been observed if material was present.

Finally, we observed a suspended graphene defect while performing scanning tunneling microscopy measurements. We found that the dA/dV doubled at the center of the defect, telling us that the localized density of states (proportional to dA/dV) also doubled.

Results and Conclusions:

We observed a statistically significant difference of 25 mV in average surface voltage potential between SEG and CVD graphene. This is proportional to a difference in surface work function for these two growth methods, which is correlated to the composition of electronic states in the material. We also observed a shift of 0.2-0.3 eV in binding energy when comparing SEG and CVD samples. This indicates that CVD graphene has less chemical interaction with platinum. STM analysis of the defects indicates an increased density of electronic states in SEG graphene suspended over a 10-20 Å diameter pit.

Acknowledgments:

The author thanks Daisuke Fujita, Nobuyuki Ishida, Hongxuan Guo, JianHua Gao, and NIMS technical staff. Support was provided by the National Science Foundation and the National Nanotechnology Infrastructure Network's International Research Experience for Undergraduates (NNIN iREU) Program.

References:

- [1] Ugeda, M. M., et al. "Point Defects on Graphene on Metals"; *Phys. Rev. Lett.*, 10, 116803 (2011).
- [2] Xu, M., et al. "Production of Extended Single-Layer Graphene"; *ACS Nano*, 5, 2, 1522-1528, (2011).
- [3] Fugita, D., Yoshihara, K. "Surface precipitation process of epitaxially grown graphite (0001) layers on carbon-doped nickel(111) surface"; *J. Vac. Sci. Technol. A* 12, 2134 (1994).

Study of the Electron Blocking Layer in Gallium Nitride Devices

Eric Reichwein

Physics, University of California Santa Cruz

NNIN REU Site: UCSB Nanofabrication Facility, University of California, Santa Barbara, CA

NNIN REU Principal Investigator: Dr. Shuji Nakamura, Material Science and Engineering, University of California, Santa Barbara

NNIN REU Mentor: Stacy Kowsz, Material Science and Engineering, University of California, Santa Barbara

Contact: ereichwe@ucsb.edu, shuji@engineering.ucsb.edu, stacy.kowsz@gmail.com

Abstract:

The electron blocking layer (EBL) is thought to increase efficiency in gallium nitride (GaN) light emitting diodes (LEDs) and laser diodes. In the LED, electrons pass through the active region, which is the region where electrons transition to a lower energy level and emit a photon. An EBL will rebound electrons that escape the quantum well back into the active region and produce light. For our project, we looked at how two different substrate growth planes, m-plane and c-plane, affect the potency of the EBL. The LED m-plane and c-plane samples were grown using metal organic chemical vapor deposition (MOCVD) on sapphire substrate and bulk GaN substrates, respectively. After processing the samples, we looked at external quantum efficiency (EQE), which is the percentage of electrons that produce photons, and its dependence on temperature and current. For the c-plane LEDs without an EBL there was a decrease in EQE by up to 15% as compared to the samples with an EBL. The m-plane samples, however, showed that there is possibly a slight efficiency gain for samples with an EBL as compared to those without and EBL for the currents considered in this study. This shows that growth plane has a significant effect on the necessity of the EBL.

Introduction:

With lots of energy waste being created by inefficient lighting, LED research is important to combat the energy crisis. LEDs significantly reduce heat output, last longer, have faster response times, and are safer than traditional light sources.

LEDs work by taking advantage of quantized electronic transitions. During a transition from higher energy to lower, the energy released is in the form of a photon. This happens billions of times a second, which produces the beautiful bright light of LEDs. For every electron that enters the LED on the negative electrode there is an electron vacancy, called a hole, flowing toward the electron. The electron and hole meet at the active region and recombine. This recombination produces light and the electron travelling in its original direction but of lower energy. LEDs are more efficient than incandescent bulbs because LEDs do not rely on current heating up a filament to produce light, rather just by reducing an electron's energy.

Experimental Procedure:

We grew the LEDs using metal organic chemical vapor deposition (MOCVD) and used two different growth planes, c-plane and m-plane, for our substrates. The c-plane LEDs were grown using a sapphire substrates, while the m-plane LEDs used bulk GaN substrate. After growing the LED using MOCVD, we processed them in the UCSB Nanofabrication Facility.

The first step was removing surface oxide with hydrofluoric acid, and then laying down an indium-tin-oxide (ITO) current-spreading layer for the positive electrode, using photolithography and electron beam deposition. After that, we etched down to the negatively doped material. Finally, we applied an electrode so we could pass current from the positive electrode through the active region and into the negative electrode. After fabrication, we used Nakamura's Packaging Lab to test the LEDs.

After testing multiple wavelength LEDs for c-plane, we concluded that the c-plane samples all needed EBLs. This was due to the polarization of the c-plane quantum well (QW), the region where the electrons make an energy transition, because we had to decrease the width of the QW to correct for the fact that the electrons and holes are separated spatially. The spatial separation of electrons and holes allowed electrons to accumulate on the p-side of the QW and this made it easier for electron escape. The EBL rebound most escaped electrons from leaving into the QW, where they recombine to produce light.

Results and Conclusions:

It is difficult to draw conclusions from our m-plane data because of our lack of devices without an EBL. But there may be improvements in efficiency from having an EBL, though efficiency gains are lesser than those seen for the c-plane devices. However, we found that for every other wavelength from 415 nm to 490 nm there was a slight difference in efficiency between LEDs with an EBL and LEDs without an EBL. But once again, there was a larger difference in efficiencies for longer wavelengths.

We also did temperature dependence measurements on both m-plane and c-plane samples, but could not determine conclusively if the EBL affected the thermal droop.

Energy Efficiency & Energy Costs	Light Emitting Diodes	Incandescent Light Bulbs	Compact Fluorescent
Life Span	50,000+ hours	1200 hours	8000 hours
Watts of electricity used	6-8 Watts	60 Watts	13-15 Watts
Kilowatts used	329kW/yr	3285kW/yr	767kW/yr
Annual operating cost	\$32.85/yr	\$328.60/yr	\$76.70/yr

Figure 1: This table is based on each type of light bulb producing 800 lumens of light.

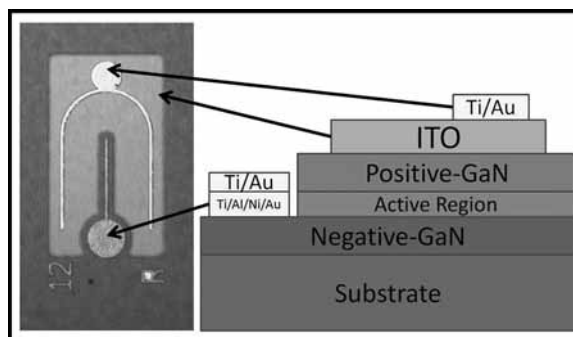


Figure 2: A diagrammatic schematic of our LED.

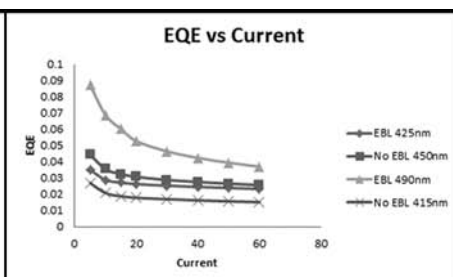
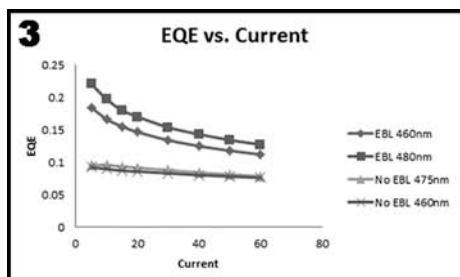


Figure 3: The EQEs of c-plane LEDs on the right are higher due to apparatus change. However, the overall trend is that the EBL increases the EQE of the c-plane LED.

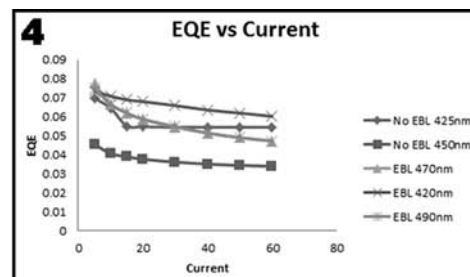


Figure 4: From the graph we see, for m-plane samples, that longer wavelength devices might benefit from an EBL more than shorter wavelength devices.

Future Work:

This study only investigated the wavelengths of 415 nm to 490 nm and only two growth planes. This research was performed as a follow up project of a paper published in Japan Applied Physics in April 2013. Kawaguchi, et al., concluded that, for non-polar and certain semi-polar growth planes, above a certain critical wavelength there is no increase in efficiency resulting from including an EBL. There are still more semi-polar growth planes on which to explore the impact of EBLs.

Acknowledgements:

I would like to thank my mentor, Stacy Kowsz, and the principal investigator of the project, Dr. Shuji Nakamura, and the NNIN UCSB coordinator, Samantha Cruz. I would also like to thank the NNIN REU Program, the National Science Foundation, and the Solid State Lighting and Energy Center (SSLEC). Finally, I would like to thank the Mitsubishi Chemical Corporation for supplying free standing GaN substrates.

Hydrogen as a Potential Cause for Native n-type Conductivity in Tin Dioxide

Emily M. Ross

Engineering, Harvey Mudd College

NNIN iREU Site: National Institute for Materials Science (NIMS), Tsukuba, Ibaraki, Japan

NNIN iREU Principal Investigator: Professor Naoki Ohashi, Optoelectronic Materials Group, NIMS

NNIN iREU Mentor: Dr. Ken Watanabe, Rechargeable Battery Materials Group, NIMS

Contact: emross@hmc.edu, ohashi.naoki@nims.go.jp, watanabe.ken@nims.go.jp

Abstract:

Tin dioxide (SnO_2) has been widely used for chemical sensors and transparent conductive films because of its wide band gap energy of 3.6 eV and n-type conductivity. The exact cause of this native n-type conductivity is not well-known, but density functional theory (DFT) calculations suggest that hydrogen (H) act as “hidden” shallow donors in SnO_2 [1]. To overcome the difficulty of analyzing hydrogen-related phenomena, this analytical study was performed using ^2H as an isotopic tracer. Pure and In-doped SnO_2 ceramics were annealed in humid O_2 gas enriched with $^2\text{H}_2\text{O}$ to introduce ^2H into the SnO_2 lattice. Characterization was performed with thermal desorption spectroscopy (TDS) and secondary ion mass spectroscopy (SIMS), as well as Raman, photoluminescence (PL) and Fourier transform infrared (FTIR) spectroscopies. Results indicate that the hydrogen that compensates the acceptor states created by indium, thus preventing p-type conductivity, mostly sit in defect sites that are more stable than those of the hydrogen that was introduced through the humid annealing process. The more stable defect sites are thought to be substitutional sites, while the less stable defects are thought to be interstitial sites.

Introduction:

The native n-type conductivity of SnO_2 is often explained by assuming that oxygen vacancies act as shallow donors, but recent density functional theory calculations claim that oxygen vacancies are too deep to act as shallow donors and instead point to hydrogen as acting as “hidden” shallow donors in SnO_2 [1]. These calculations also indicate that indium and gallium could create shallow acceptor states in SnO_2 that would cause p-type conductivity [1]. However, p-type tin dioxide has never been obtained experimentally. DFT claims this is because the acceptor states created by gallium and indium are compensated by hydrogen [1].

The technique of using isotopic tracers allows characterization based on the mass difference between isotopes. Ideally, a

common isotope is exchanged for a less common isotope — ^2H for ^1H in this case. The ^2H is introduced to the system via $^2\text{H}_2\text{O}$. This $^2\text{H}_2\text{O}$ then becomes $^2\text{H}^1\text{HO}$ through an exchange process that allows ^1H to be replaced by ^2H . The ^1H that was previously in the lattice is then carried off by $^2\text{H}^1\text{HO}$, while the ^2H diffuses further into the lattice.

Experimental Procedure:

Pure and In-doped SnO_2 bulk ceramics were used in this study. Before beginning the humid annealing process, they were polished and sintered to smooth the surface and repair mechanical damage. To introduce ^2H into the SnO_2 lattice as an isotopic tracer, samples were annealed in humid O_2 gas enriched with $^2\text{H}_2\text{O}$ for one hour at 200°C, 300°C or 400°C. The $^2\text{H}_2\text{O}$ contained 98 atomic% ^2H and had a dew point of 60°C, resulting in an absolute humidity concentration of about 19.6 volume%.

Samples were characterized before and after annealing, mainly using methods that took advantage of the difference in mass between ^1H and ^2H . These methods include TDS, in which the samples are heated from room temperature to 1000°C to create a desorption profile for reactivity analysis; and SIMS, in which the material surface is sputtered to create a composition depth profile for diffusivity analysis. Other characterization techniques used include PL, Raman and FTIR spectroscopies.

Results and Conclusions:

TDS was used to analyze defect stability because it gives information about how much energy is needed to desorb a certain species. Thus, the higher the desorption temperature, the greater the stability of the species. This can be translated to the stability of a species in a particular defect when the species are isotopes, so the main difference between the two is their

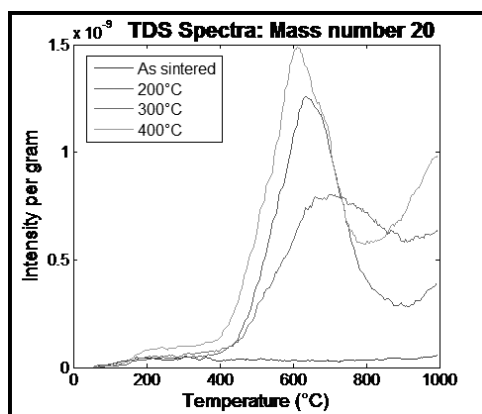


Figure 1: TDS spectra of In-doped SnO_2 for mass number 20, which corresponds to $^2\text{H}_2\text{O}$.

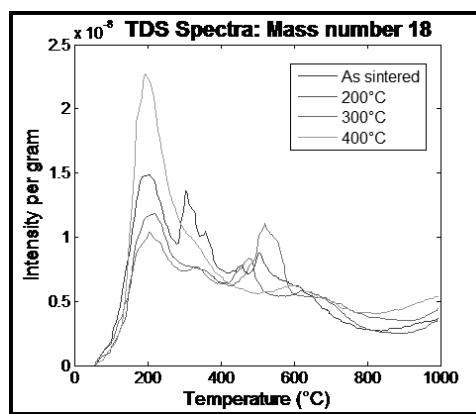


Figure 2: TDS spectra of In-doped SnO_2 for mass number 18, which corresponds to $^1\text{H}_2\text{O}$.

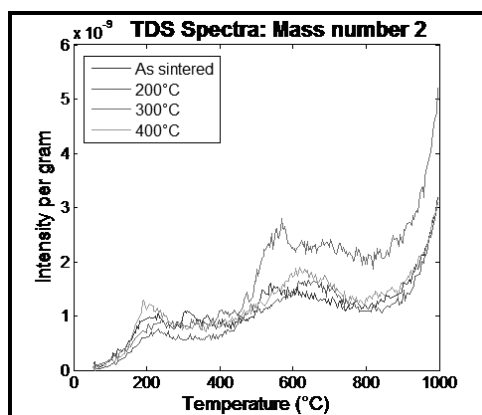


Figure 3: TDS spectra of In-doped SnO_2 for mass number 2, which corresponds to $^1\text{H}_2$.

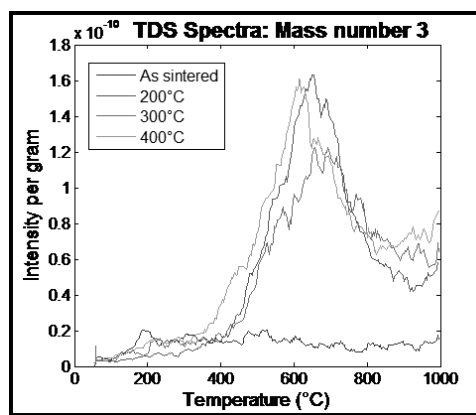


Figure 4: TDS spectra of In-doped SnO_2 for mass number 3, which corresponds to $^1\text{H}^1\text{H}$.

surroundings. Peaks at 610-690°C and around 1000°C were deemed to be the most important for understanding hydrogen behavior. In the ranges of interest, mass number 2 corresponds to $^1\text{H}_2$, mass number 3 to $^1\text{H}_2\text{H}$, mass number 18 to $^1\text{H}_2\text{O}$, and mass number 20 to $^2\text{H}_2\text{O}$.

For mass number 20 (Figure 1), there was a strong peak at 610-690°C for the annealed samples, but no peak for the sample that had not been annealed, as expected. However, there was no peak in that same range for mass number 18 (Figure 2), which indicates that hydrogen was likely being added to SnO_2 lattice instead of being exchanged. This was supported with SIMS data that showed the concentration of ^2H in the In-doped ceramics was approximately an order of magnitude higher than that of the pure ceramics.

For mass number 2 (Figure 3), the dominant hydrogen peak was around 1000°C, while the dominant hydrogen peak for mass number 3 (Figure 4) was at 610-690°C for the annealed samples. This indicates that the ^1H that was initially in the In-doped ceramics and compensated the acceptor states created by In mostly sat in stable defect sites. The ^2H that was added to the

material sat in less stable defect sites. These sites are believed to be substitution and interstitial sites, respectively, because of their relative stabilities.

Acknowledgments:

I would like to thank all of the people and organizations that made my summer research possible: Professor Naoki Ohashi and Dr. Ken Watanabe for guiding me and my work; Dr. Minako Hashiguchi, Dr. Noriko Saito and Dr. Takeo Ohsawa for their help; the National Institute for Materials Science for hosting me; and the National Nanotechnology Infrastructure Network International Research Experience for Undergraduates (NNIN iREU) Program and National Science Foundation for providing funding.

References:

- [1] Singh, A., et al.; "Sources of Electrical Conductivity in SnO_2 "; Physical Review Letters, 101.5, 055502 (2008).

Solid-State NMR of $(\text{CdSe})_{13}(\text{Propylamine})_{13}$

Michael E.H. West

Chemical Engineering and Physics, University of Arkansas

NNIN REU Site: Nano Research Facility, Washington University in St. Louis, St. Louis, MO

NNIN REU Principal Investigator: Dr. Sophia Hayes, Department of Chemistry, Washington University in St. Louis

NNIN REU Mentor: Dr. Zayd Ma, Department of Chemistry, Washington University in St. Louis

Contact: mew016@email.uark.edu, hayes@wustl.edu, zaydma@wuchem.wustl.edu

Abstract and Introduction:

Cadmium selenide (CdSe) nanoparticles exhibit unique electrical properties due to quantum confinement of electrons, showing potential for wide-ranging nanomaterial applications [1]. A constituent of these nanoparticles are so-called “magic number clusters” of CdSe, which are stable molecular units that can be synthesized with high purity. It is not known what makes these specifically numbered clusters stable and what the actual structure is. Samples of $(\text{CdSe})_{13}(n\text{-propylamine})_{13}$, one of these magic number clusters capped with *n*-propylamine ligands, were synthesized in near-purity and in quantities suitable for NMR spectroscopy by the Buhro lab at Washington University [2]. All NMR studies were performed in Sophia Hayes’s lab.

Experimental Background:

For this project we focused on the NMR active nuclei ^{113}Cd . ^{113}Cd is a very difficult nucleus to find and acquire signal due to a relatively slow precession frequency (9.4 MHz/Tesla), low isotopic abundance (12.26%), a very large chemical shift range (> 3000 ppm), and exceptionally long longitudinal relaxation times (T_1 values over three hours are not uncommon). The other NMR active nuclei in the cluster are ^{111}Cd and ^{77}Se , which are both less sensitive than ^{113}Cd . On average, only one of each NMR active nuclei will be in the nanocluster, which leaves 23 atoms with spin zero. The absence of spin-zero nuclei has the effect of nullifying any strong dipolar interaction within the cluster and lengthening the relaxation time. Further elongating the relaxation time is the lack of a repeating crystal structure with strong phonon modes to mediate spin flips. The lack of repeating crystal orientation is due to each cluster being encapsulated in propylamine ligands. Even with these experimental realities, we were able to acquire high quality ^{113}Cd NMR data on the $(\text{CdSe})_{13}(n\text{-propylamine})_{13}$ nanoclusters.

Experimental Procedure:

All solid-state NMR experiments were performed at room temperature on a 7T (300 MHz) superconducting magnet using a 4 mm MAS Chemagnetics probe tuned to 65.45 and 294.97 MHz for ^{113}Cd and ^1H , respectively. A 4 mm zirconium rotor, Tecmag Apollo spectrometer, and 1 kW amplifiers on ^1H and ^{113}Cd channels were used universally.

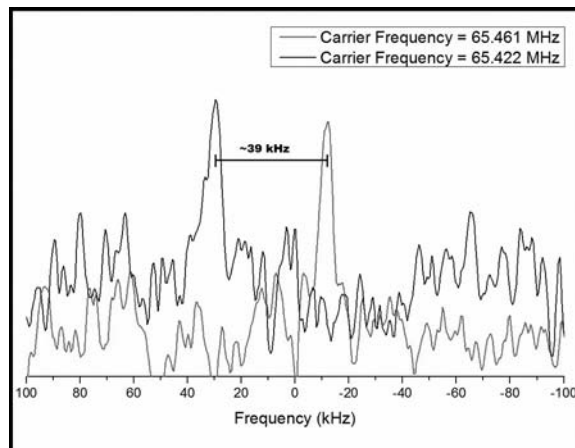


Figure 1: ^{113}Cd DEFT NMR of $(\text{CdSe})_{13}(\text{propylamine})_{13}$ at differing carrier frequencies.

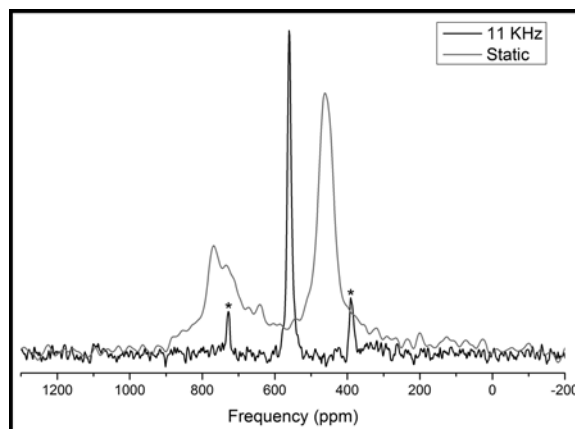


Figure 2: Static CP and 11 kHz CPMAS ^{113}Cd NMR of $(\text{CdSe})_{13}(\text{propylamine})_{13}$.

Three types of NMR pulse sequences were used to excite and observe the ^{113}Cd spins: “90-acquire,” “Driven Equilibrium Fourier Transform” (DEFT), and “Cross-Polarization Magic Angle Spinning” (CPMAS).

The 90-acquire pulse sequences were used to acquire reference spectra and to optimize equipment. DEFT is a pulse sequence that can reduce the effects of long T_1 relaxation times by realigning nuclear spins back along the main magnetic field after observing the NMR signal. CPMAS is a technique developed by a researcher from Washington University [3] that cross-polarizes the ^{113}Cd with the ^1H , which allows the use of the ^1H relaxation time (typically much faster than ^{113}Cd) and results in a large signal enhancement of the ^{113}Cd . “Magic angle spinning” refers to rapid rotation (> 10 kHz) of the sample about 54.7° relative to the applied magnetic field.

Previous work would indicate that (CdSe) would have a chemical shift that is roughly similar to previous CdSe NMR spectroscopy, such as in the case with Berrettini et al. [1] working with 2 nm CdSe nanoparticles and having a chemical shift of roughly 600 ppm referenced to 0.5M $\text{Cd}(\text{NO}_3)_2$ solution, so initial signal hunting focused largely on the region from 300-800 ppm from our reference, 0.1M $\text{Cd}(\text{ClO}_4)_2$.

After pulse optimization and all reference spectra acquisition, our efforts were focused on finding direct ^{113}Cd signal using DEFT. Figure 1 shows results from two DEFT experiments with different excitation frequencies which proved the validity of the signal at 458 ppm. This result ensured we had found the ^{113}Cd signal and told us the frequency range to focus our CPMAS experiments.

Results and Discussion:

DEFT experiments proved to be too long to acquire acceptable signal to noise and we turned to CPMAS. Our goal was to use the ^1H magnetization on the propylamine ligands to polarize the ^{113}Cd and then observe the ^{113}Cd signal. This worked exceptionally well and the results of this experiment are shown in Figure 2.

As ^{113}Cd is a spin $\frac{1}{2}$ nuclei, each unique chemical site should result in only one peak. The CPMAS results while spinning indeed indicate only a single site. It is known that different parts of a powder pattern line CP differently depending on their orientation with respect to the applied magnetic field [4] and this is why the static CPMAS result has two peaks. Longer contact times result in the expected static lineshape of an axially symmetric site.

If the $(\text{CdSe})_{13}$ cluster has a central Cd, we would expect it to have a different chemical shift than the outer cadmiums. However, the ability for magnetization to transfer from a ^1H to a central Cd would be severely hampered by distance from surface protons to the center, and spin diffusion through the virtually spin-free nanocluster results in a very weak CPMAS signal. Thus, our conclusion at this juncture in the research is we have, for the first time, successfully observed at least one unique cadmium site and further work, such as ^{77}Se NMR, needs to be done to complete the NMR study of this material.

Acknowledgements:

I would like to thank the NNIN REU Program and the NSF for supporting this project. Thank you to Nathan Reed and Dee Stewart for locally coordinating the program. Thank you to the Buhro and Hayes lab, specifically Dr. Sophia Hayes, Dr. Zayd Ma, Yuanyuan Wang, Katie Wentz, and Andrew Surface for their direct contributions.

References:

- [1] Berrettini, Mia G., et al.; J. Am. Chem. Soc., 126, 7063-7070 (2004).
- [2] Wang, Yuanyuan, et al.; Inorganic Chemistry 52, 2933-2938 (2013).
- [3] Schaefer, J., and Stejskal, E.O.; J.Am.Chem.Soc., 98, 1031-1032 (1976).
- [4] Pines, A., M. G. Gibby, and J. S. Waugh. The Journal of Chemical Physics 59.2: 582 (1973).

Synthesis of Metal Supported Catalysts for the Hydrogenolysis of Lignin

Jeanne Xu
Chemistry, Wellesley College

NNIN REU Site: Nano Research Facility, Washington University in St. Louis, St. Louis, MO

NNIN REU Principal Investigator: Dr. Marcus Foston, Energy, Environmental, and Chemical Engr., Washington University in St. Louis

NNIN REU Mentor: Yu Gao, Department of Energy, Environmental, and Chemical Engineering, Washington University in St. Louis

Contact: jxu3@wellesley.edu, mfoston@seas.wustl.edu, gaoyu@wustl.edu

Abstract:

Transition-metal (nickel, cobalt, copper, and iron) containing metal-oxide material (silica, alumina, and titania) were screened in an effort to develop heterogeneous catalysts for the hydrogenolysis of lignin that selectively cleave aryl ether linkages. Different combinations of active transition-metal precursors with metal-oxide supports were synthesized by sol-gel processes, and the synthetic conditions for silica-, alumina-, and titania-supported catalysts were optimized. To minimize contamination and avoid oxidation, multiple washes with deionized water followed by sonication, centrifugation, Soxhlet extraction, and calcination under flowing inert nitrogen (N) atmosphere were investigated and an optimal protocol determined. Future characterization studies and investigations on catalytic activity and selectivity for aryl ether hydrogenolysis will determine the optimal transition-metal and metal-oxide support combination for selective hydrogenolysis of lignin.

Introduction:

Plant biomass, a renewable resource rich in carbon and chemical potential energy, is a promising feedstock to displace non-renewable petroleum [1]. In particular, lignin, one of the three main components of the plant cell wall, is an under-utilized feedstock that is currently considered as waste [1].

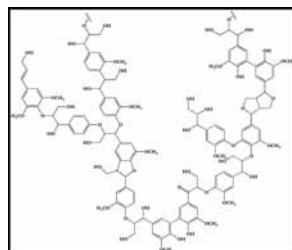


Figure 1: Representation of the molecular structure of lignin.

The highly heterogeneous structure of lignin (Figure 1) makes it difficult to deconstruct and therefore utilize; however, its rich aromatic composition is an ideal precursor for a variety of fuels and value-added reactive intermediates [1]. While many thermochemical processes can exploit lignin's potential, large energy inputs and harsh reaction conditions are required, often leading to a wide distribution of products [1].

Our research goal focused on synthesizing transition-metal containing metal-oxide catalysts that will be utilized in the production of a narrow distribution of phenolic-like products from lignin with minimal energy and material inputs. Sol-gel processes were employed due to better control on catalyst

structure and chemical properties, higher thermal stability, and its low-cost [2].

Experimental Procedure:

All catalysts were prepared by co-precipitation methods adapted from literature and had a transition-metal to metal-oxide ratio of 0.6 [2]. Active component metal precursor solutions included: either 30 mL of a 0.86 M transition-metal ($\text{Ni}(\text{NO}_3)_2 \cdot 6\text{H}_2\text{O}$, $\text{Co}(\text{NO}_3)_2 \cdot 6\text{H}_2\text{O}$, $\text{FeCl}_2 \cdot 4\text{H}_2\text{O}$) or 53 mL of a 0.49 M $\text{Cu}(\text{NO}_3)_2 \cdot 3\text{H}_2\text{O}$ solution in 100% ethanol. Mesoporous variants were synthesized to control porosity using various surfactants. In each case, mesoporous variants were generated by adding hexadecyltrimethylammonium bromide (CTAB) prior to the addition of metal-oxide precursor. Figure 2 illustrates the chemistry that occurred in the synthesis of the catalysts. Figure 3 outlines the synthesis of the catalysts.

Silica-Supported Catalyst. An initial solution of tetraethyl orthosilicate and ethanol was added to 1.5 mL of 0.3 M hydrochloric acid (HCl). The solution was stirred at 50°C for 90 minutes. At 25°C, the appropriate active component metal precursor solution was added to the reaction mixture. A firm gel formed upon the slow addition of 35 mL 30% aqueous ammonium hydroxide in 65 mL ethanol.

Alumina-Supported Catalyst. A solution of 10.0 g hexylene glycol in the appropriate active component metal precursor solution was stirred at 95°C for 30 minutes. Aluminum isopropoxide (8.6 g) was then introduced to the solution and stirred at 120°C for four hours. At 95°C, a saturated solution of sodium hydroxide in ethanol (~0.5 mL) was added every 30 minutes for a span of 90 minutes. At 25°C, the pH of the solution was adjusted to 9.0 with sodium hydroxide.

Titania-Supported Catalyst: A solution containing 12.2 g titanium isopropoxide, 22 mL ethanol, and the appropriate active component metal precursor solution was mixed under inert (argon) atmosphere. A second solution consisting of 3 mL of 1.8 M nitric acid in 3 mL 100% ethanol was slowly added to the first solution, resulting in the formation of a firm gel.

For all catalysts, the gelled suspension solution was stirred at 25°C for 30 min, sonicated for 1 h, and aged at 25°C for 85 h.

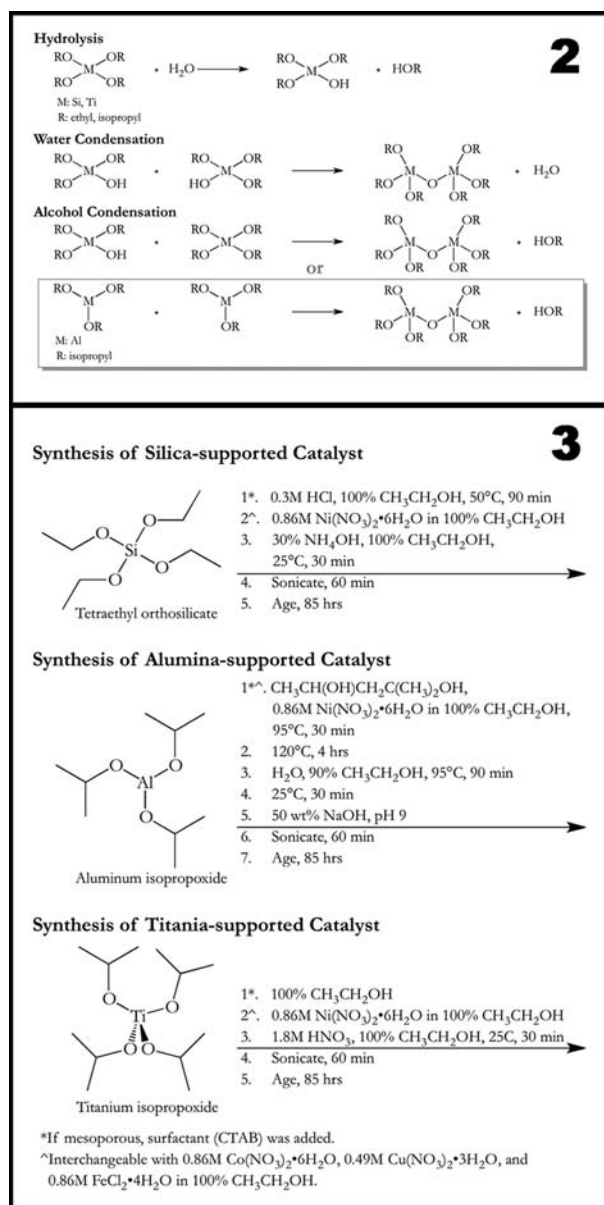


Figure 2, top: Three primary reactions in silica, titania, and alumina gel formation.

Figure 3, bottom: Adapted synthesis protocol for metal supported catalysts.

Purification of Catalysts. Catalysts were washed with deionized water, collected by centrifugation, and underwent Soxhlet extraction with deionized water overnight and then with ethanol overnight or 48 hours for mesoporous variants. Catalysts were dried overnight at 105°C under vacuum and calcinated under flowing inert N atmosphere at 550°C for 5 h.

Conclusions and Future Work:

Metal supported catalysts were successfully synthesized after modifications to the synthesis and purification protocols. Sol-gel condensation reactions in alumina-supported catalysts were optimized at 25°C at a pH of 9.0. To prevent premature

gelling and the formation of heterogeneous products, titania-supported catalysts required lower reaction concentrations. Furthermore, the incorporation of the transition-metals in the titania-supported catalysts appeared to be low due to their appearance. Ultimately, future work with titania will use an alternative procedure.

To minimize contamination by unincorporated metal precursors, multiple washes with deionized water followed by sonication, centrifugation, and Soxhlet extraction were determined to be optimal. In addition, calcination can cause significant oxidation and charring, and therefore must be performed under flowing inert nitrogen atmosphere rather than in air.

Future work includes characterizing the chemical and physical properties of the catalysts by several methods (Table 1). To determine the effect catalyst structure has on the activity and selectivity for arylether hydrogenolysis, catalysts will be screened against model compounds and lignin. Various preparation methods will be explored to investigate the effect preparation method has on catalyst structure. Ultimately, the goal is to determine the optimal transition-metal and metal-oxide support combination for aryl ether hydrogenolysis.

Acknowledgments:

My sincerest gratitude to Dr. Marcus Foston, Yu Gao, and Jake Meyer for their guidance and support. I would also like to thank Dee Stewart and Nathan Reed from the NRF, the NNIN REU Program, and the NSF. My grateful thanks are extended to Mindy Prado, Siqin He, Michelle Liberton, and Dr. Wei-ning Wang.

References:

- [1] Pandey, M. P., et al.; Chem Eng Technol, 34(1), 29-41 (2011).
- [2] Goncalves, G., et al.; Journal of Non-Crystalline Solids, 352(32), 3697-3704 (2006).

Method or Instrument	Purpose
Brunauer-Emmett-Teller (BET) method	Specific surface area
Barrett-Joyner-Halenda (BJH) method	Pore diameter
Fourier transform infrared spectroscopy (FTIR)	Carbon contamination
Inductively coupled plasma mass spectrometry (ICP-MS)	Metal composition
Hammett acidity function	Acidity of catalyst
Esterification	Acidity of catalyst
Transmission electron microscopy (TEM)	Particle size and shape

Table 1: Characterization methods for determining the chemical and physical properties of the catalysts.

Fabrication of Smart Gels with Tunable Stiffness

Carolyn Zhang

Biochemistry and Cell Biology, University of California San Diego

NNIN REU Site: Center for Nanoscale Systems, Harvard University, Cambridge, MA

NNIN REU Principal Investigator: Professor David A. Weitz, Harvard School of Engineering and Applied Sciences, Harvard University

NNIN REU Mentors: Dr. Adrian Pegoraro, Tom Kodger, and Ming Guo, Harvard School of Engr. and Applied Sciences, Harvard University

Contact: cmzhang@ucsd.edu, weitz@seas.harvard.edu, apegoraro@seas.harvard.edu, tkodger@fas.harvard.edu, mingguo@fas.harvard.edu

Abstract:

The differentiation of stem cells was influenced by many factors, one of which was the stiffness of the cellular microenvironment: soft substrates led to neuronal cells, intermediate stiffness substrates led to myogenic cells, and very rigid scaffolds lead to osteogenic cells [1]. To further understand the kinetics of stem cell differentiation, we designed degradable polyacrylamide hydrogels, which allowed us to change substrate stiffness during differentiation, and observe the effect of this change on the lineage specification of stem cells. With this purpose in mind, 8 wt% polyacrylamide gels composed of permanent *N,N'*-methylenebisacrylamide (BIS) and degradable *N,N'*-bis-(acryloyl)cystamine (BAC) cross-linkers were constructed. The shear modulus of these gels can be changed from ~ 10 kPa to ~ 400 Pa. Under normal conditions, these gels would lead to osteogenic and neuronal differentiation, respectively. This hydrogel was found to be degraded in a time span that maintained continuous cell proliferation with the biocompatible chemical tris(2-carboxyethyl)phosphine hydrochloride (TCEP) in Dulbecco's modified eagle's medium (DMEM). Since stem cells are known to commit to their final cell type within a week, using these gels will allow us to test whether the time point at which the scaffold is degraded affects the final lineage specification of the cells.

Experimental Procedure:

For our experiments, we made polyacrylamide gels and varied the amount of degradable and permanent crosslinkers. We used an 8 wt% polyacrylamide, 0.46 wt% BAC, 0.03 wt% Bis solution; this ratio was chosen to mimic a stiff, Bis only, gel (8 wt% acrylamide, 0.3 wt% Bis) predegradation and a soft gel (8 wt% acrylamide, 0.03 wt% Bis) after being degraded. By laying a 12 mm diameter coverslip on the solution and polymerizing the gel at 65°C, we fabricated degradable gels that were about 100 μm thick. The gels were then treated with a Sulfo-SANPAH solution followed by a 0.1 mg/ml collagen solution. The addition of collagen to the surface allowed the cells to adhere to the gel.

For initial tests of the degradable gels, HF fibroblasts of the BJ line are cultured on the gels and after about five hours, imaged as the gels degraded in a 10 mM TCEP (pH 7) solution over a period of ten hours. The Young's modulus of the degradable gel was measured on a Squisher device, or modified atomic force microscope (AFM), while the shear modulus was measured on a rheometer.

Results and Conclusions:

We tested several compounds to degrade the gel for both biocompatibility and effective degradation. We defined a compound as being biocompatible if cells continued to proliferate after exposure. To measure degradation, we simply allowed the gel to swell and degrade, and measured the time it took to complete the process. A 10 mM TCEP at a pH of 7 that was diluted in DMEM was determined to be the reducing agent that was biocompatible and able to degrade the gel on a desirable timescale.

Tested Chemicals for Degradation	Biocompatible:	
	Degrades gel	in media in DMEM
Dithiothreitol = DTT	✓	✗
Glutathione = GSH	✗	✓
GSH in HEPES buffer	✗	✗
L-Cystine	✗	✗
Hydrazine	✓	✗
L-Ascorbic acid (Vitamin C)	✓	✗
2-Phospho-L-ascorbic acid	✗	✗
Bisulfite	✗	✗
Tris(2-carboxyethyl) phosphine hydrochloride =	✓	✗
TCEP (ph 7)		✓
Tris(2-carboxyethyl) phosphine hydrochloride =	✓	✗
TCEP (ph 3)		✗

Figure 1: The chemicals that were tested to degrade the hydrogels composed of 8% polyacrylamide, 0.46% BAC, 0.03% Bis solution.

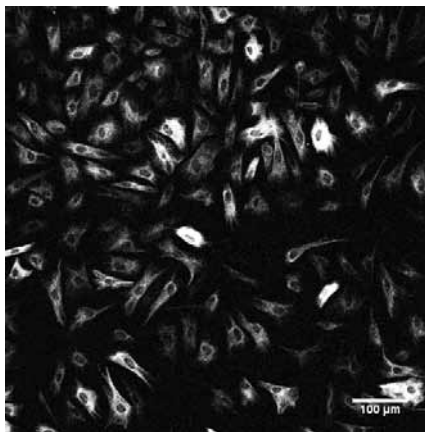


Figure 2: Fibroblasts cultured on the degradable gel before the degradation process.

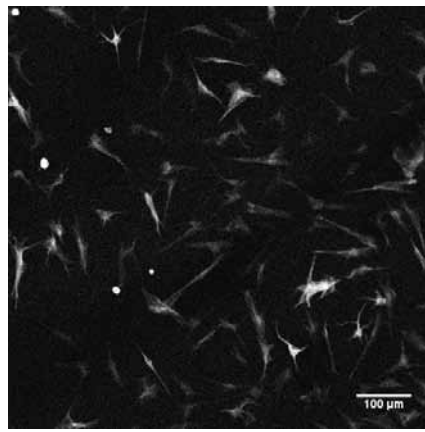


Figure 3: Fibroblasts after a 12 hour 10 mM TCEP treatment to degrade the gel.

Using a rheometer, we measured the change in the gel stiffness during polymerization as the temperature increased to 65°C. Our degradable gels had a shear modulus of the same order as a 0.3% Bis gel (stiff gel) and a degraded gel was estimated to have a shear modulus similar to a 0.03% Bis gel (soft gel) and should favor osteogenic and neurogenic differentiation, respectively.

To confirm these measurements, we used a “Squisher” device. By compressing an indenter into the gel by a known distance, we were able to measure the Young’s modulus of the gel and determined that 100 mM and 10 mM TCEP conditions had the same degradation rate during a 12.5 hour degradation process. The kinetics of the degradation process for the degradable gel between 100 mM and 10 mM TCEP remained the same despite changes in the pH of the TCEP conditions.

To measure the effect of degradation on cells, we observed the effect of an ~ten-fold decrease in the stiffness of our degradable gel on fibroblasts and found that the cell area decreased after the gel is degraded. A morphology change between cells that were cultured on our degradable gel before the degradation process and those cultured on our gels after the degradation process was also noted. Those cultured on the initially stiff gels were spread out and after the TCEP treatment; they remained spread out, while cells cultured on pre-degraded, soft gels had a rounder morphology.

In conclusion, 8% polyacrylamide 0.46% BAC 0.03% Bis gels can be made to have a ten-fold decrease in shear modulus after degradation. A 10 mM TCEP in DMEM was determined to be

a biocompatible reducing agent that is able to degrade the gels on a desired timescale. Preliminary results showed that TCEP was biocompatible with and didn’t interfere with the differentiation of stem cells, however, further experiments are required to indicate statistical significance.

Future Work:

With applications in tissue engineering, future works for this project include culturing Mesenchymal stem cells on degradable gels to study the differentiation on different stiffness scaffolds as well as finding a biocompatible chemical that reversibly degrades the gels.

Acknowledgements:

I would like to thank my mentors Dr. Adrian Pagararo, Tom Kodger, Ming Guo, my principal investigator Professor David A. Weitz, and my site coordinator Dr. Katherine Hollar for their assistance. I would also like to thank the National Science Foundation and the National Nanotechnology Infrastructure Network Research Experience for Undergraduates Program for providing funding for my research.

References:

- [1] Discher, D.E., Janmey, P., and Wang, Y.L. Tissue cells feel and respond to the stiffness of their substrate. *Science*. 310(5751):1139-43;2005.

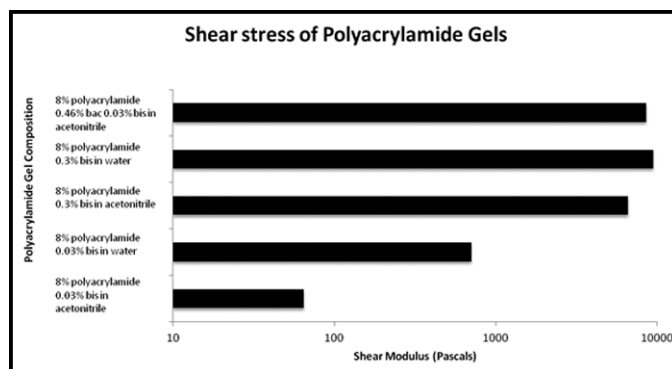


Figure 4: Comparison of the shear modulus of polyacrylamide gels of different cross-linker compositions with the degradable gel being the 8% polyacrylamide 0.46% BAC 0.03% Bis gel.